N° d'ordre 51-2015 Année 2015

THESE DE L'UNIVERSITE DE LYON

Délivrée par

L'UNIVERSITE CLAUDE BERNARD LYON 1

ECOLE DOCTORALE DE PHYSIQUE ET D'ASTROPHYSIQUE

DIPLOME DE DOCTORAT
Spécialité: PHYSIQUE

Soutenue publiquement le 28 avril 2015
par

JI Ming Chao

TITRE:

Molecular Relaxation Dynamics Of Anthracene Cations Studied In An Electrostatic Storage Ring

Directeur de thèse:
Prof. Li CHEN et Dr. Serge MARTIN

JURY: M. Jean-Yves CHESNEL rapporteur
M. Philippe RONCIN rapporteur
M. Christian BORDAS
M. Jean-Philippe CHAMPEAUX
Mme. Li CHEN
M. Serge MARTIN

UNIVERSITE CLAUDE BERNARD - LYON 1

Président de l'Université	**M. François-Noël GILLY**
Vice-président du Conseil d'Administration	M. le Professeur Hamda BEN HADID
Vice-président du Conseil des Etudes et de la Vie Universitaire	M. le Professeur Philippe LALLE
Vice-président du Conseil Scientifique	M. le Professeur Germain GILLET
Directeur Général des Services	M. Alain HELLEU

COMPOSANTES SANTE

Faculté de Médecine Lyon Est – Claude Bernard	Directeur : M. le Professeur J. ETIENNE
Faculté de Médecine et de Maïeutique Lyon Sud – Charles Mérieux	Directeur : Mme la Professeure C. BURILLON
Faculté d'Odontologie	Directeur : M. le Professeur D. BOURGEOIS
Institut des Sciences Pharmaceutiques et Biologiques	Directeur : Mme la Professeure C. VINCIGUERRA
Institut des Sciences et Techniques de la Réadaptation	Directeur : M. le Professeur Y. MATILLON
Département de formation et Centre de Recherche en Biologie Humaine	Directeur : M. le Professeur P. FARGE

COMPOSANTES ET DEPARTEMENTS DE SCIENCES ET TECHNOLOGIE

Faculté des Sciences et Technologies	Directeur : M. le Professeur F. DE MARCHI
Département Biologie	Directeur : M. le Professeur F. FLEURY
Département Chimie Biochimie	Directeur : Mme le Professeur H. PARROT
Département GEP	Directeur : M. N. SIAUVE
Département Informatique	Directeur : M. le Professeur S. AKKOUCHE
Département Mathématiques	Directeur : M. le Professeur A. GOLDMAN
Département Mécanique	Directeur : M. le Professeur H. BEN HADID
Département Physique	Directeur : Mme S. FLECK
Département Sciences de la Terre	Directeur : Mme la Professeure I. DANIEL
UFR Sciences et Techniques des Activités Physiques et Sportives	Directeur : M. C. COLLIGNON
Observatoire des Sciences de l'Univers de Lyon	Directeur : M. B. GUIDERDONI
Polytech Lyon	Directeur : M. P. FOURNIER
Ecole Supérieure de Chimie Physique Electronique	Directeur : M. G. PIGNAULT
Institut Universitaire de Technologie de Lyon 1	Directeur : M. C. VITON
Institut Universitaire de Formation des Maîtres	Directeur : M. A. MOUGNIOTTE
Institut de Science Financière et d'Assurances	Administrateur provisoire : M. N. LEBOISNE

Acknowledgements

This thesis has been accomplished in Ions Multichargé group, Institut Lumière Matière (ILM), Université Claude Bernard Lyon 1 (UCBL), France from September 2011 to April 2015.

First, I tender my deepest thanks to my dedicated supervisors, Prof. Li CHEN and Dr. Serge Martin, for giving me the opportunity to work on this new and challenging project, for your guidance and encouragement throughout my thesis work, for the discussions and corrections of my manuscript, and for your care of my living in Lyon as well.

I'd like to thank Dr. Jérôme BERNARD and Dr. Richard BREDY, for the inspiring discussions with you, also for your advice and help during my thesis work. I thank Miss Céline ORTEGA for the pleasure time spent together in the laboratory and during the conferences. I'd like to watch your basketball match again! I also thank Mr. Guillaume MONTAGNE, Mr. Alain BOURGEY and other technical staff for your support in the experiments. I sincerely thank Mrs. Aurélie BORDAS, Mr. Claude LESAGE and all the administration staff of ILM and UCBL.

I express my gratitude to our collaborators and visitors, Dr. Bruno CONCINA and Prof. Abdul Rahman ALLOUCHE in ILM; Prof. Amine CASSIMI from CIMAP, Caen; Dr. Dongbin QIAN and Dr. Bin LI from IMP, Lanzhou; Prof. Christine JOBLIN from IRAP, Toulouse; Dr. Géraldine FERAUD; Prof. Hajime TANUMA and Miss Naoko KONO from TMU, Tokyo; thank you all for the rewarding discussions.

To my friends, Hui (LI), Xueshi, Hui (REN), Qianli, Xiaochun, Mengqing, and other friends whose names are not listed here, thank you all for your company and help during my stay in Lyon.

I gratefully acknowledge Prof. Ximeng CHEN, Dr. Jianxiong SHAO, Dr. Lin CHEN, Dr. Chunlin ZHOU and Dr. Xueyang LV, for your advice and help for

applying the scholarship from China Scholarship Council (CSC). I also express my acknowledgement to CSC for funding this thesis.

I owe a great thanks to my wife Min and my family. Thank you so much for your understanding and all your support for my study abroad. Despite the time and distance, you are always in my heart.

Résumé

Les molécules hydrocarbures aromatiques polycycliques (HAP) sont à l'heure actuelle considérées comme probablement responsables des bandes d'émission infrarouge non identifiées du milieu interstellaire (MIS). La dynamique de refroidissement des molécules HAP est essentielle pour estimer leur photo-stabilité, leur durée de vie et les distributions de taille dans le MIS. Au cours des dernières années, les expériences s'appuyant sur le stockage électrostatique d'ions moléculaires ou d'agrégats sont devenus des outils puissants pour étudier leur refroidissement dans une large gamme de temps allant de la microseconde à quelques secondes. En général, l'étude des courbes de déclin associées aux processus de dissociation dans le cas des cations ou bien de détachement d'électrons dans le cas des anions fournit des informations sur l'évolution de l'énergie interne des ions stockés.

Dans ce travail de thèse, le refroidissement de cations d'anthracène a été étudié dans un anneau de stockage électrostatique compact, le Mini-Ring, jusqu'à 8 ms. Les courbes de déclin spontané provenant de la dissociation par émission de fragment C_2H_2 ou H neutres montrent trois régions distinctives. Ces trois régions indiquent différents régimes de refroidissement en fonction du temps de stockage, la dissociation domine pour les temps inférieurs à 1 ms, l'effet de l'émission radiative entre alors en compétition avec la dissociation puis domine au-delà de 3 ms.

Au cours du cycle de stockage, des impulsions laser sont envoyées pour ré-exciter des ions moléculaires après un temps de stockage bien contrôlé. Les courbes de déclin induit par laser suivent approximativement une loi de puissance en $t^{-\alpha}$. La diminution du coefficient α avec le temps de stockage indique un décalage vers les basses énergies de la distribution d'énergie interne (DEI) des ions stockés. En utilisant une modélisation simple de la dépendance de la DEI en fonction de α, son extrémité à haute énergie ainsi que son taux de variation $\Delta E/\Delta t$ ont été déduits à plusieurs différents temps de stockage à l'aide d'un modèle statistique. Deux séries de mesures de α ont été obtenues en modifiant l'énergie des photons de $h\nu_1$ à $h\nu_2$. L'intervalle de temps nécessaire pour que la DEI se décale d'une énergie correspondant à $h(\nu_2 - \nu_1)$ a été déterminé expérimentalement en fonction du temps de stockage, permettant ainsi de mesurer directement le taux de variation de la DEI $\Delta E/\Delta t$ sans utiliser de modèle théorique.

Pour obtenir une évolution plus précise de l'évolution de la DEI en fonction du temps de stockage, un modèle statistique (RRKM ou loi d'Arrhenius) a été utilisé pour calculer les taux de dissociation en fonction de l'énergie interne. La DEI a été simulée par une fonction multi-paramétrée et des ajustements ont été réalisés pour minimiser l'écart entre les courbes de déclin mesurées et calculées aux différents temps de stockage. Par cette méthode, des taux de déclins de population variant de 25 à 450 s^{-1} ont été mesurés pour des énergies internes de 6 à 7,4 eV. Après correction des effets dus à l'émission infrarouge provenant de transitions entre niveaux vibrationnels, le décalage d'énergie attribué au processus de fluorescence due à des transitions provenant d'états électroniques excités thermiquement s'élève en moyenne à environ 100 eV/s. Dans la gamme d'énergie étudiée, la fluorescence via des transitions électroniques est le processus dominant dans le refroidissement radiatif.

Mots clés: HAP, anthracène, dissociation, refroidissement radiatif, distribution d'énergie interne, Poincaré fluorescence, transition électronique.

Abstract

The polycyclic aromatic hydrocarbon (PAH) molecules have been considered as possible carrier of the unidentified infrared emission bands from the interstellar medium (ISM) for about thirty years. The cooling dynamics of the PAH molecules which is essential to estimate their photostability and therefore their lifetime and size distributions in the ISM, has attracted numerous theoretical and experimental studies. In recent years, electrostatic storage devices (ESD) became powerful tool to investigate the cooling regime of molecules and clusters in a large time range from microseconds to seconds. Generally speaking, the decay of the emitted neutral yields due to dissociation of molecular cations or electron detachment of anions in such experiments carries information on the internal energy of the stored molecular ions.

In this thesis work, the cooling regimes of anthracene cations are studied by following the time evolution of the internal energy distribution (IED) of the stored anthracene cations. A spontaneous neutral yield curve obtained from the stored molecular ions as a function of the storage time shows three distinguishable regions. The three regions indicate different cooling regimes at corresponding storage time range, i.e., the dissociation mechanism of the molecule dominates at storage time $t < 1$ ms, quenching of the dissociation by radiative cooling processes occurs during $1 < t < 3$ ms and radiative cooling governs at $t > 3$ ms.

During the storage cycle, laser pulses are sent to irradiate the stored molecular ions at well-controlled storage time. The laser induced neutral yield curves are fitted with a $t^{-\alpha}$ law, and the decrease of factor α with the storage time indicates the shift of the IED of the stored ions to lower energies. Combining with a simple modeling of the α-IED dependence, the high energy edge of IED and the shift rate $\Delta E/\Delta t$ of IED as well, are estimated at various storage times. By changing the photon energy ($h\nu_1$ to $h\nu_2$) of laser pulses to irradiate the stored ions, two series of α are obtained. The time interval Δt necessary for the IED of the stored ions to undergo a shift ΔE that matches the energy difference of $h(\nu_2 - \nu_1)$ are determined as a function of the storage time, thus the shift rate $\Delta E/\Delta t$ of the IED is estimated without involving any IED simulations.

By fitting the laser induced neutral yield curves with theoretical ones calculated from the modeled dissociation rates and assumed multi-parameter function to estimate

the IED, the IED of the stored ions is drawn up. The average energy shift rate of IED from 3 to 7 ms is estimated to be about 100 eV s^{-1}. The population decay of IED due to radiative emission is measured to be 25 to 450 s^{-1} as a function of internal energy from 6 to 7.4 eV. After the correction of the population decay due to infrared emission via vibrational transitions, the fluorescence emission rate due to electronic transition from thermally excited state is obtained to be 20 to 400 s^{-1} from 6 to 7.4 eV. The measured fluorescence emission rate is an evidence of the predicted Poincaré fluorescence. In the studied internal energy range, the fluorescence emission process via electronic transition is the dominant mechanism of radiative cooling.

Key words: PAH, ESD, anthracene, radiative cooling, quenching, internal energy distribution, energy shift rate, Poincaré fluorescence

Contents

Outline

In this thesis work, a newly built electrostatic storage ring, the Mini-Ring, is presented in detail, and the cooling dynamics of anthracene cation is studied in Mini-Ring. This thesis consists of five chapters organized as described below:

Chapter 1 gives a brief review of the PAH hypothesis, the electrostatic storage devices (ESDs), and the earlier studies carried out on the ESDs as well.

Chapter 2 introduces the previous studies on the cooling dynamics of PAH molecules and the photon absorption characteristics of our studying candidate, the anthracene cation. In addition, several calculations are performed to help to understand the ESD experiments.

Chapter 3 presents the experimental setup. This chapter is developed along three lines: detailed description of the experimental setup including data acquisition and pulsed laser equipment, simulations of ion trajectories in Mini-Ring by SIMION software, and optimization of storage using visualized ion beam trajectory and detector imaging.

Chapter 4 starts with the description of the experimental methods and parameters. Subsequently, the experiments performed on anthracene cation are explained, the time scales in Mini-Ring experiments as well as the sensitive energy window are also discussed. More specifically, an experiment performed on a long storage time range is thoroughly analyzed and the fast radiative cooling mechanism is experimentally observed on the PAH molecules.

Chapter 5 shortly summarizes this thesis and gives perspectives.

Chapter 1 Introduction

Since the polycyclic aromatic hydrocarbon (PAH) molecules were proposed as possible carriers of the characteristic infrared (IR) emission bands observed from the interstellar medium (ISM), various studies on the PAH molecules have been performed during the past three decades aiming to figure out their origin, evolution and role in the universe [1]. In the first section of this chapter, the proposal of PAH molecules as possible carriers of the observed characteristic emission bands, and the studies on the PAH molecules will be briefly introduced.

In the second section, the electrostatic storage devices (ESDs) and the studies carried out on will be introduced. In recent years, the experiments performed on compact ESDs have demonstrated their great potential in many fields of physics like atomic and molecular physics, mass spectrometry, biophysics, etc [2]. Taking the advantage of such new storage devices, the study on the relaxation dynamics of the PAH molecules will be considered, which is the aim of the present work.

1.1 UIR Bands and PAH Molecules

The story started in the early 1970s when several unidentified infrared (UIR) bands were firstly discovered in the ISM. From then on, people started to search the species responsible for these UIR bands, after about one decade, the members of the PAH family were proposed as possible carriers.

1.1.1 UIR Bands in the ISM

The IR emission features around 10 μm were first discovered on the observations of NGC 7207 and BD +30°3639 in the ISM by Gillett et al [3]. Afterward, it was noticed that the 11.3 μm band was always combined together with a set of emission

bands at 3.3, 6.2, 7.7 and 8.6 μm, as presented in Figure 1.1 [4]. These emission features were found to be a common characteristic of many objects in the ISM. Although several proposals of the possible carriers were given [4], the identification of the carrier remained mysterious for almost a decade, and these emission bands were collectively called UIR bands.

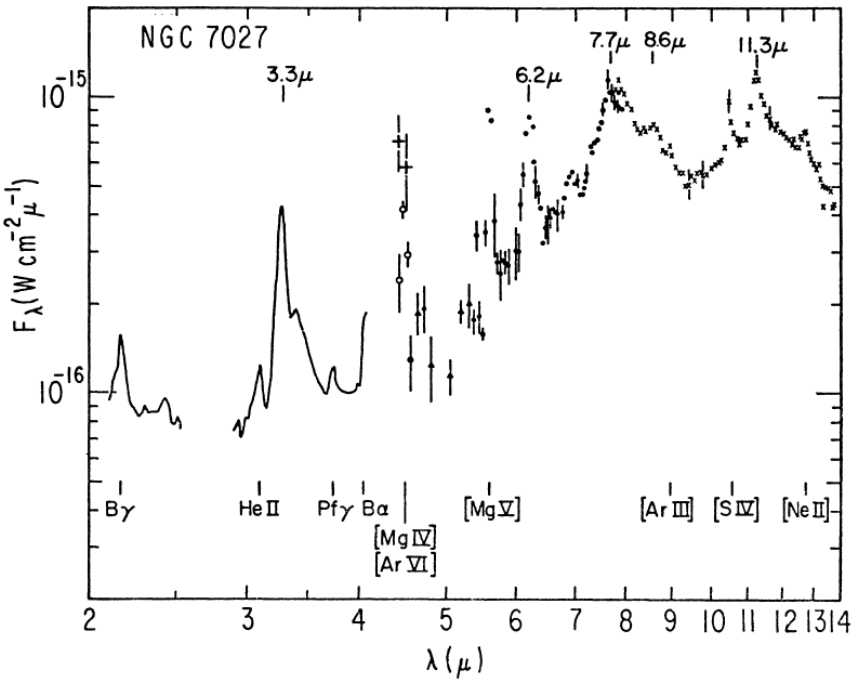

Figure 1.1 First overview IR emission spectrum of NGC 7027 from 2 to 13 μm. From Ref. [4].

In 1981, Duley and Williams realized that the emission features of the UIR bands were quite characteristic for aromatic molecules, so they proposed the hydrogenated carbon grains as the carriers of UIR bands [5]. By calculating the emission of coronene molecule heated to 600 K, Léger and Puget found that the emission spectrum of coronene ($C_{24}H_{12}$) fitted well with the UIR bands, then the PAH molecules appeared in sight as possible carriers [6]. Independently, Allamandola et al calculated the IR emission intensities of chrysene ($C_{18}H_{12}$) and attributed the UIR bands to partially hydrogenated, positively charged PAHs [7]. This proposal of PAH molecules as carriers of the UIR bands in ISM was then developed to the PAH hypothesis [1]. This hypothesis suggests that a substantial fraction (10% – 20%) of carbon in the universe is in form of PAH molecules, which exist ubiquitously in the ISM.

1.1.2 **Studies on PAH molecules**

PAH molecules are hydrocarbon molecules composed of multiple aromatic rings in honeycomb structure with peripheral H atoms. Figure 1.2 presents several members of this large molecule family. Since being proposed as possible carriers of the UIR bands, the PAH molecules have attracted numerous experimental and theoretical studies. These studies were mainly carried out on their IR spectra as well as their physical and chemical properties in the ISM environment [1].

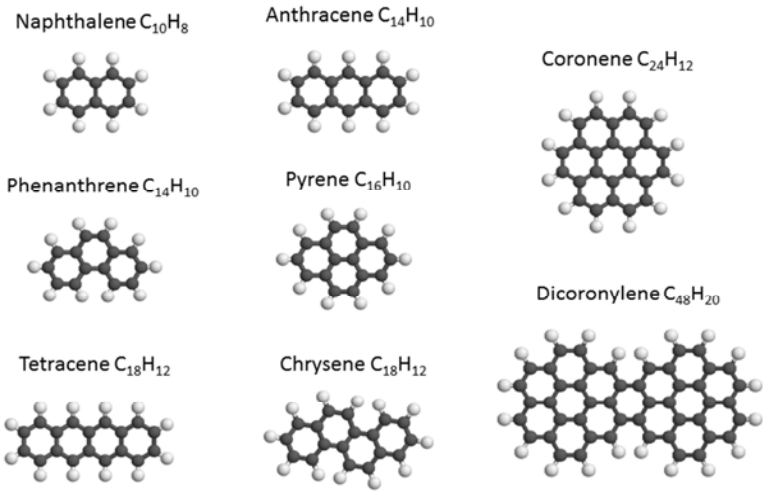

Figure 1.2 Several PAH molecules.

Since 1990s, numerous studies have been performed on the IR spectra of different PAH molecules like naphthalene [8], anthracene [9], pyrene [10], coronene [11], etc. These IR spectra obtained with matrix isolation spectroscopy (MIS), infrared multiple-photon dissociation of trapped ions (MPD), dissociation spectroscopy of ionic PAH van der Waals clusters (VDW), and infrared emission (IRE) have been compared and discussed by Oomens et al [12]. Using combined laboratory spectra of neutral and cationic PAH molecules, Allamandola et al have modeled the IR emission bands associated with different interstellar objects. Their models may indicate the structures, stabilities, abundances and ionization balance of the PAH molecules in the ISM [13].

The physical and chemical properties of PAH molecules in the ISM environment have also been widely studied [14] [15]. The PAH molecules in the ISM can be neutral or ionized depending on the physical conditions as well as the properties of the PAH molecules. In 1996, Salama et al have studied the charge distribution and spectroscopic properties of the interstellar PAH molecules, and evaluated the contributions from PAH molecules with different size and charge states [16]. By calculating the internal energies of PAH molecules at which the dissociation rates reach 10^2 and 10^4 s^{-1}, Jochims et al suggested that PAH molecules with a small

number of carbon atoms (< 30 ~ 40) would prefer dissociation rather than IR emission, while for those with a large number of carbon atoms (> 30 ~ 40), the principal relaxation channel would be IR emission [17]. The lifetimes of the PAH molecules, were also calculated at various distances from the sun, for instance the lifetime of anthracene was calculated to be about 30 s at a distance 1 AU (average distance between the earth and the sun, 1 AU ≈ 1.5×10^8 km) from the sun [18]. Beside these studies which related directly to the PAH hypothesis, several other studies indicated that the PAH molecules may play an important role in other aspects. For instance, the PAH molecules were suggested to be the precursors of biogenic molecules which hold the key to the origin of life [19] and the traces of star formation [1].

These studies accomplished during the past three decades have strongly extended our understanding on the PAH molecules. Nevertheless, the lack of detailed knowledge of their physical properties restricts our awareness of the PAH molecules and the UIR bands; no even one single molecule has been identified in the ISM up to now. Further studies like the cooling dynamics of the PAH molecules are still essential to estimate their size distribution and therefore to understand their roles in the universe. Considering their heavy mass (typically around hundreds) and their slow cooling processes (cooling time up to seconds), the storage techniques are needed to study these PAH molecules.

1.2 Electrostatic Storage Devices

The storage rings and ion traps built with only electrostatic electrodes were developed in the laboratories in the late 1990s. The electrostatic storage rings (ESR) and electrostatic ion beam traps (EIBTs), are collectively called electrostatic storage devices (ESDs). Due to their compact designs and relatively small sizes, the ESDs have shown their great advantages and potential in many fields of physics. In this section, a brief review of the ESDs and the physics studied on them will be presented. In the first subsection, a short history of the ESDs together with the structures of EIBTs and ESRs will be introduced; the physics studied on the ESDs in different fields will be summarized in the second subsection.

1.2.1 ESRs and EIBTs

Although the history of the ESDs is less than twenty years, the technique of trapping ions can be traced back to the invention of the Paul and Penning Trap in the 1950s. Using electric and magnetic multiple fields to confine the charged particles in three dimensions, the ion traps are built to store ions for long enough time and for well

localized position in space as well. Since 1970s, a new type of storage device, the heavy-ion storage rings (CERN, GSI, etc.) were developed using mainly magnetic bending and focusing elements for high energy particle physics. In general, the trapping/storing of ions in traps or rings brings several advantages in experiments, for instance the better energy measurement precision with longer observation time (according to Heisenberg uncertainty principle, $\Delta E \Delta t \geq \hbar/2$), the long lifetime measurements of metastable states, well controlled perturbation, and recycling of ions [2].

In contrast to the magnetic field which bends the ion trajectory depending on the ion momentum and therefore on the square root of its mass, the electric field deflects the passing through ion depending on its kinetic energy only. For identical kinetic energy, the deflection of ions is independent of mass. Therefore, in principle, there is no mass limitation to the stored ions in the ESDs; this is the main advantage of such devices. Additional advantages are the low construction and operation costs, easier tuning and operation, etc. Considering these advantages, ELISA, the first ESR for heavy ions was built at Aarhus University, Denmark in 1996 [20]. Thereafter, numerous ESRs with very different structures have been constructed in several laboratories, for instance the "tabletop" Mini-Ring in our group [21] and the double rings DESIREE at Stockholm University, Sweden [22].

The development of small EIBTs went almost in parallel with that of ESRs. The basic concept of EIBTs is inspired by the storage of a photon beam between two mirrors where certain condition for stability is fulfilled. This condition for symmetric mirror is given as following [23] [24],

$$0 \leq \left(1 - \frac{L}{2f}\right)^2 \leq 1$$

Equation 1-1

where f stands for the focal distance of the mirror and L for the distance between the two mirrors. This equation is equivalent to

$$L/4 \leq f < \infty$$

Equation 1-2

The analogous design of symmetric mirrors is also used for ion storage. As long as the geometry and focal length of the electrostatic mirrors fulfill the above condition, a stable storage of an ion beam between the two electrostatic mirrors is expected. The EIBTs were firstly developed simultaneously and separately at both Weizmann Institute of Science [23] and Berkeley [25]. Subsequently, several laboratories have

developed their own EIBTs based on the design developed at the Weizmann Institute of Science, for instance the one at Queen's University, Belfast [26] and the one as part of the CSR project in Heidelberg, Germany [27]. Another interesting EIBT geometry is the ConeTrap developed at Stockholm University, which consists of only three electrodes [28].

In the following, choosing one or two examples from the ESRs and EIBTs, the structures and characteristics of the two types of ESDs will be discussed, respectively. Beside these examples, the other ESRs and EIBTs will also be briefly introduced.

1.2.1.1 **Electrostatic Storage Rings**

Up to now, there are more than ten ESRs in operation or under construction in the world. In this paragraph, choosing ELISA which is the first ESR and the most representative one as example, the design and characteristics of the ESRs will be discussed.

Figure 1.3 presents the layout of ELISA; it has a racetrack shape with a circumference of 6.28 m. The initial optics of ELISA was defined by two spherical 160° deflectors (SDEH), four 10° horizontal deflectors (DEH) and four pairs of quadrupoles (QEV, QEH). Four additional vertical ± 1° deflectors (DEV) are arranged to allow fine vertical correction of the ions' orbits [20]. Later on, the two spherical deflectors were replaced by two 160° cylindrical deflectors to avoid the sharp focusing points in the center of the spherical deflectors since the sharp focusing effect strongly reduced the ion beam lifetime.

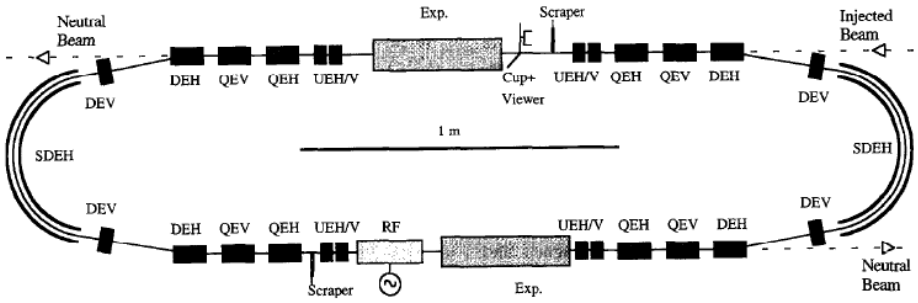

Figure 1.3 Layout of ELISA [20]. SDEH designates the spherical 160° horizontal deflectors, DEH and DEV the horizontal and vertical electrostatic deflectors, QEH and QEV the horizontally and vertically focusing electrostatic quadrupoles, UEH and UEV the horizontal and vertical pick-up electrodes, RF the drift-tube radio frequency system.

Different ion sources can be mounted on a high voltage (maximum 25 kV) platform to prepare the ion beam for ELISA. For instance sputter ion source, hollow-

cathode glow discharge source, Nielsen-type source, and electrospray ionization source have been used to prepare various ion species for ELISA [2]. The ions are injected into the ring as ion bunches of μs duration through one of the straight sections when the voltages on the first DEH are off; after injection the voltages on the first DEH are turned on by fast switches, the ion bunch then can circulate inside the ring. The pressure inside the ring can reach 10^{-11} mbar, which gives a lifetime of typically 10 to 1000 s. The neutrals emitted from the ring are collected at the end of one straight section, while laser pulses are sent to merge the stored ion bunch in the center of the other straight section.

The second ESR, ESRing, came into operation at KEK-High Energy Accelerator Research Organization in Japan in 2000 [29]. Apart from its unique merging electron target, the ESRing essentially shares the same design as ELISA [30]. The TMU E-ring constructed at Tokyo Metropolitan University in 2004 also shares similar design as ELISA, but the improved liquid nitrogen cooling system can lower down the temperature of inner region down to below -50 °C. It is also noteworthy that four sets of beam position monitors (BPM) have been installed on the straight sections to monitor and tune ions' trajectories [31] [32].

The DESIREE consisting of two ESRs which share one merging section, came into operation at Stockholm University, Sweden in 2011 [22]. The two rings running at cryogenic temperature 13 K are dedicated to store positive and negative ions simultaneously and respectively. The physics at low ion-ion collision energies will be studied in the merging section.

The SAPHIRA, as part of ASTRID2 synchrotron radiation facility in Aarhus, has been set up and commissioned. It has a simple square geometry (1×1 m) and is dedicated to the laser induced processes in atomic and molecular ions [33]. Recently, a cryogenic ring named as RICE [34] in AMO Physics Laboratory, RIKEN, Japan came into operation, and ELASR [35] which also follows the design of ELISA have been constructed in Riyadh, Saudi Arabia.

There are still several ESRs under construction, for instance, the Frankfurt low energy storage ring (FLSR) [36], the cryogenic storage ring (CSR) in Heidelberg [37], and the μE-ring at Tokyo Metropolitan University [38].

These ESRs, designed with circumferences from meters to tens of meters (CSR, 35 m), are used to store ions with kinetic energy from several keV to tens of keV. Due to their compact designs and relative small sizes, the control of temperature becomes realizable, for instance the RICE ring can be cooled down to 4 K. Lowering the temperature has several advantages, for instance improving the vacuum and reducing the black-body radiation.

1.2.1.2 **Electrostatic Ion Beam Traps**

The EIBTs, compared to the ESRs, are designed with even smaller sizes and more compact structures. In this paragraph, the EIBT at Weizmann Institute (referred as Zajfman trap hereafter) and the ConeTrap at Stockholm University, Sweden, are chosen as examples to discuss the designs and characteristics of EIBTs.

Figure 1.4 presents the schematic view of the Zajfman trap at Weizmann Institute [23]. This ion trap consists of two electrostatic mirrors and a field free region between them. Each mirror is made of five electrodes with voltages V_s divided linearly from E5 to E1. The grounded electrode A1 at the end of each mirror is employed to reduce the electric field out of the trap. To inject ions, the left mirror is grounded to let the ion bunch pass through; once the ion bunch is located inside the trap, the voltages on the left mirror are switched on by a fast switch, the ions are then stored between the two mirrors. In order to focus the stored ions, two additional electrodes Z1 (voltages V_z) and Z2 (grounded) together with electrode E5 act as an asymmetric Einzel lens. Thus, the Zajfman trap is actually characterized by only two voltages, Vs and Vz.

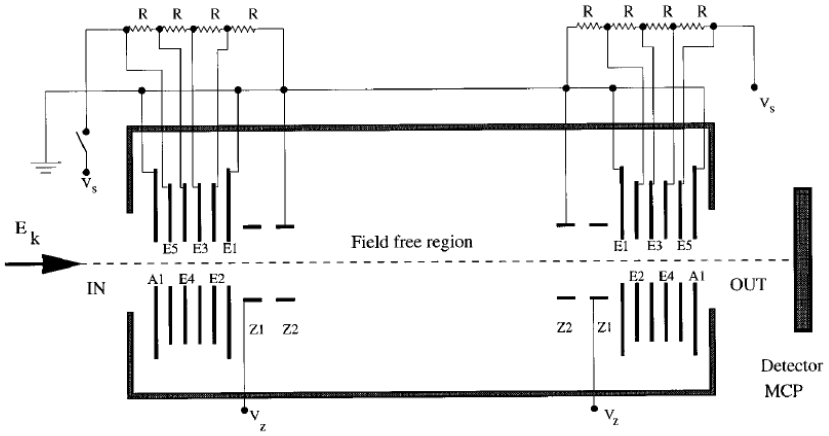

Figure 1.4 Layout of the Zajfman trap. Electrodes E5-E1 work as electrostatic mirror; E5, Z1 and Z2 form an asymmetric Einzel lens [23].

The ions travel in the field free region in straight lines with their initial kinetic energies, and the length of this region can be modified as needed. To monitor the stored ion bunch, a pick-up ring electrode arranged in the field free region can measure the image charges when the ions pass through [39]. The interactions of the stored ions with photons, electrons or ions are usually performed in the field free region. For instance an electron target can be installed in the field free region to study the collision with stored ions [40], detectors can also be arranged along the field free region to collect the charged particles or electrons resulting from collisions [41]. To collect

neutral particles, the detector is usually placed at the end of the trap, as shown in the figure.

Comparing to Zajfman trap, the ConeTrap consisting of only three electrodes has even simpler design, as shown in Figure 1.5 [28] [42]. Two cone shaped electrodes are installed facing each other with a cylindrical electrode between them. Due to this special design, the electric fields inside the two cone electrodes can not only reflect but also focus the stored ions. With proper choices of the dimensions and the applied voltages on the three electrodes, stable storage conditions can be fulfilled. The injection of ions is similar to that of Zajfman trap by grounding the left mirror to inject and switching on the voltage after injection. Due to the miniature design, the detector is also placed at the end of the ConeTrap. In Lyon, in order to study the delayed fragmentation of recoil ion after collision, an ion trap with similar design as ConeTrap was installed into the time-of-flight tube to store the C_{60} molecular ions [43] [44].

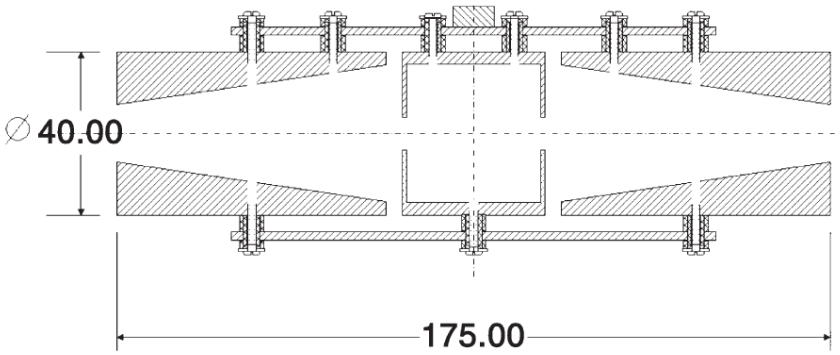

Figure 1.5 The geometry of ConeTrap (dimensions in mm) [28].

The ions are usually injected into the EIBTs by unit of ion bunch with a given width. The stability and ion loss of the ion bunch in Zajfman trap have been both experimentally and numerically investigated by Pedersen et al [39]. The properties of ion bunch like bunch expansion, particle loss, bunch decay and radio-frequency bunching have also been studied in the cryogenic trap for fast ion beams (CTF) under an extremely high vacuum (10^{-14} mbar) [45].

Due to the use of electric field to reflect the stored ions, these EIBTs are usually limited to a few keV. However, due to the miniature structures, the revolution period of stored ions is typically around several microseconds.

The experience that we have learned from other ESDs greatly helped us to build our Mini-Ring, for instance we have learned from ELISA to avoid sharp focusing point, and to achieve simple design of electrostatic mirror from ConeTrap. The Mini-Ring originated from ConeTrap has run as an ESR in our laboratory since 2008. Its circumference of ion trajectory is 0.73 m, it is the first real “tabletop” ring and the

smallest ESR in the world. This thesis work is performed on Mini-Ring, the detailed description of the ring will be presented later in chapter 3.

Generally speaking, the ESRs and EIBTs are designed with small sizes but high storage ability especially for clusters and bio-molecules. The ESDs usually operate at several keV to tens of keV under low pressure from 10^{-9} to 10^{-14} mbar. The ESDs can be cooled down to cryogenic temperature, even to a few K. These features bring many advantages to the experiments performed on ESDs, and therefore the ESDs show great potential in many fields.

1.2.2 **Physics on the ESDs**

The physics studied on the ESDs concerns many fields. In this subsection, the following aspects are briefly summarized: lifetime measurement, absorption profile measurement, study of cooling dynamics, collision with electrons, and mass spectrometry. In the past two decades, numerous works have been performed on the ESDs and yielded an impressive list of achievements. Hereby, choosing one or two experiments in each aspect, the physics that have been studied on the ESDs will be succinctly introduced.

1.2.2.1 **Lifetime Measurement**

Before the appearance of ESDs, physical processes of relatively long lifetimes were studied on magnetic heavy-ion storage rings. Due to the use of magnetic fields to bend and focus the stored ions, the closely spaced fine-structure components of ions may be mixed by the magnetic fields. This brings complexity to the interpretation of the experimental data [46]. Using the ESDs instead of magnetic storage ring to store the ions, this kind of difficulty can be avoided.

Taking the lifetime measurements of metastable He^- [48] and Be^- [49] as examples, the species were stored in ELISA and Zajfman trap, respectively, and the neutrals were recorded by MCP detectors as a function of the storage time (Figure 1.6). By fitting the collected neutral yields with an exponential decay law, the lifetimes of stored species were obtained. As shown in the figure, the lifetimes of He^- were estimated to be 10.9 ± 0.1 μs for angular momenta $J = 1/2, 3/2$ and 306.1 ± 2.0 μs for $J = 5/2$ by Pedersen et al, while the lifetime of Be^- is obtained as 42.07 ± 0.12 μs by Knoll et al.

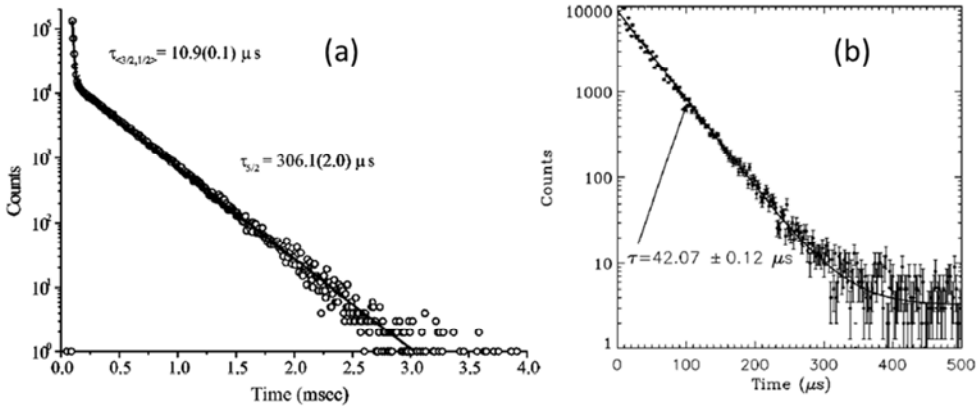

Figure 1.6 Collected neutral yields as a function of the storage time. (a) Neutral He measured in ELISA [47]. (b) Neutral Be measured in Zajfman trap [48].

It is noteworthy that the lifetime measurement of He^- was also carried out by Reinhed et al in the ConeTrap under different temperatures 10, 50 and 296 K [49]. The measured lifetime of $1s2s2p\,^4P^0_{5/2}$ level of He^- was compared with the value obtained from other experiments and theory. It was found that the lifetime decreases strongly with the increasing temperature above 100 K. The observed temperature dependence was attributed to the photodetachment due to blackbody radiation.

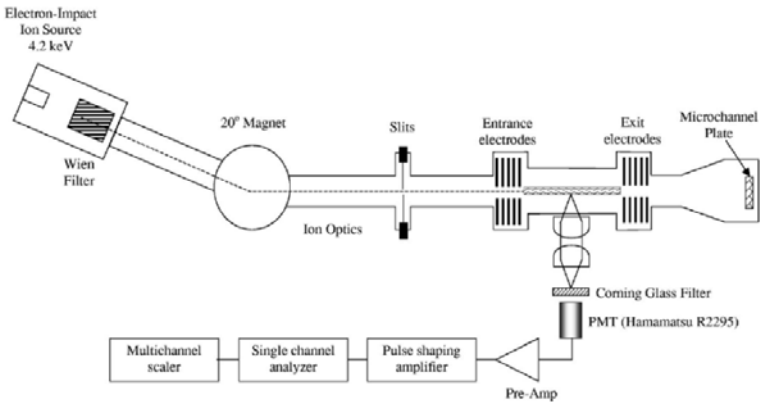

Figure 1.7 Schematic view of the Zajfman trap with photon counting system [50].

To measure the radiative lifetime of a metastable state, like $^1S_0$ state of Xe^{2+} [50], a photomultiplier was installed in the field free region of Zajfman trap to collect the emitted photons, as shown in Figure 1.7. The collected photon yields were plotted as a function of storage time (Figure 1.8). After correction of the beam lifetime, a value of 4.46 ± 0.08 ms was obtained for the $^1S_0$ state of Xe^{2+}.

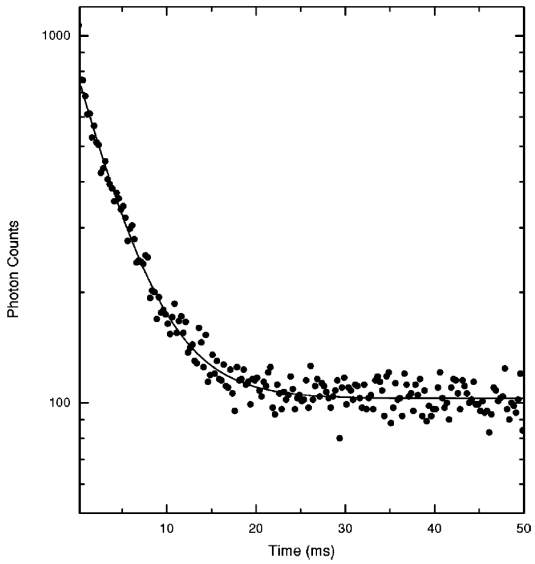

Figure 1.8 Photon yield decay curve of ${}^1S_0$ state of Xe^{2+}. From Ref. [50].

Besides the experiments discussed above, various lifetime measurements have also been performed on other species, like molecular ions H_2CC^- [52], SF_6^- [53], and cluster ions [53]. Taking the advantages of the small dimensions as well as the ease of controlling temperature of the ESDs, these measurements simplified the experimental process and improved the measurement precision as compared to the previous studies.

1.2.2.2 **Absorption Profile**

The absorption profile is one of the important characteristics of molecules, especially for the photoactive proteins. The absorption profiles of gas-phase molecular ions can be measured from the laser induced neutral fragments. The chromophore of green (red) fluorescent protein (GFP, or RFP) were produced in an electrospray ion source and stored in ELISA, then the laser induced neutral fragments were monitored as a function of the photon wavelength [55] [56]. The measurement of photon absorption cross-section at a specific wavelength was obtained from

$$\sigma \propto \frac{N_{neutrals}}{N_{ions}} \frac{1}{E\lambda}$$

Equation 1-3

where σ is the cross-section for photon absorption, $N_{neutrals}$ the number of laser induced neutrals, N_{ions} the number of ions in the stored ion bunch, E the pulse energy of laser, and λ the photon wavelength. By studying both the cation and anion of chromophore of GFP, their absorption profiles in vacuum were compared with that

obtained in other media, protein and solution [54], as shown in Figure 1.9. It was shown that the location of the absorption band of anionic GFP chromophore is ascribed almost purely to the intrinsic chemical properties of the chromophore. Similar works on other GFP and RFP chromophores are also performed in ELISA and discussed in different papers [57] [58] [59].

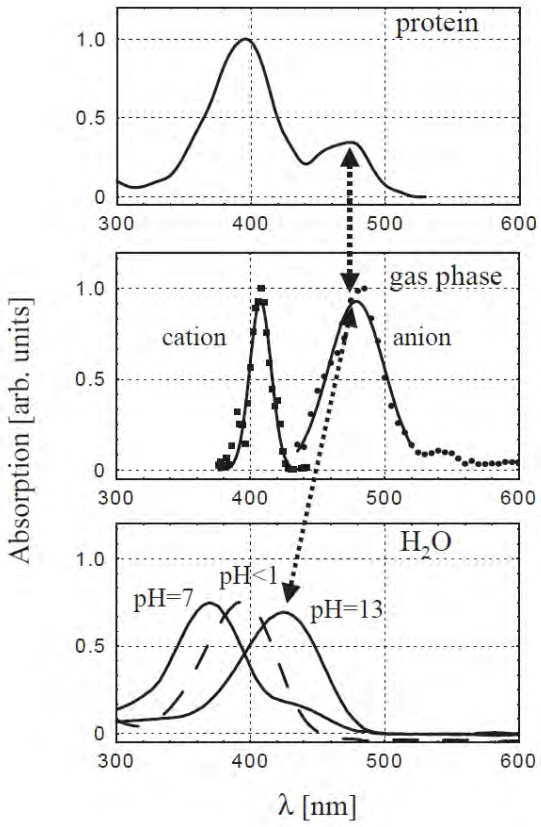

Figure 1.9 Photon absorption spectra. Top: the wild-type Aequorea victoria GFP; middle: the chromophore of GFP in vacuum condition; bottom: the chromophore of GFP in aqueous solutions of different pH values. From Ref. [54].

1.2.2.3 **Cooling Dynamics**

The neutrals emitted from the ESDs due to laser induced dissociation from cations (or electron detachment from anions) are the easiest detectable signals. By studying the neutral yields emitted from the stored Ag_5^-, Al_7^- clusters and $C_{36\sim94}^-$ molecular ions in ELISA, Hansen et al have first shown that, for cluster or molecular ions with broad internal energy distribution, the neutral yields resulting from statistical decay process tend to a t^{-1} distribution [60].

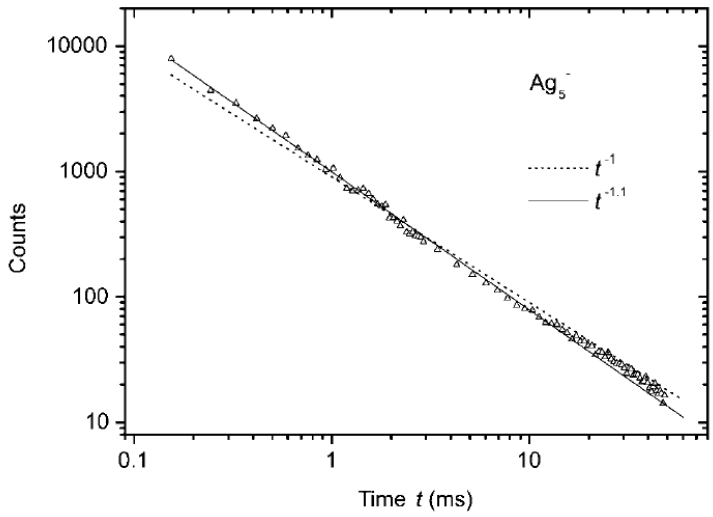

Figure 1.10 Neutral yields due to electron detachment of stored Ag_5^- clusters in ELISA. The decay is close to a t^{-1} distribution but is fitted better with a power -1.1. From Ref. [60].

In order to understand the t^{-1} behavior of the neutral yields and the cooling dynamics of the molecular ions, various experiments on different molecules have been carried out. The photo-destruction experiments on Adenosine 5′-Monophosphate (AMP) nucleotide ions showed that the AMP anions fragment in a statistical process while the cations don't [61]. Using theoretical models to reproduce the neutral yields resulting from laser induced electron detachment from molecular anions, detailed information about the electron detachment process was obtained [62] [63]. In the experiments performed with protonated amino acids up to storage time 100 ms, Andersen et al noticed that the dissociation of metastable molecules follows approximately the t^{-1} law until a time τ after which the neutral yields drop and deviate from the t^{-1} law, as shown in Figure 1.11 [64]. This fast reduction of neutral yields after time τ was attributed to the quenching of dissociation by radiative cooling.

The radiative cooling process, as a nondissociative process, has been studied indirectly for many different molecular and cluster ions, for instance fullerene anions C_N^- with N value from 36 to 94 [65] [66] [67], aluminum cluster anions [68] [69], carbon cluster anions [70] [71] [72] and PAH molecules like naphthalene cations [73], anthracene cations [74]. In these works, statistical models have been applied to reproduce the collected neutral yields and/or to draw the conclusions. Some physical pictures could thus be obtained, like the absolute cooling rate, the radiative cooling rate [67], and the internal energy distribution [70].

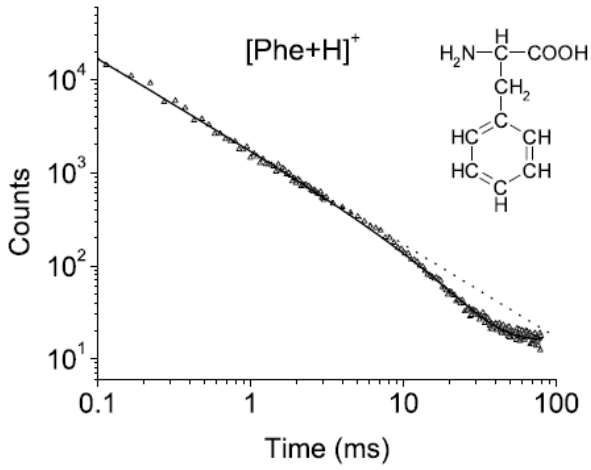

Figure 1.11 Neutral yields of protonated phenylalanine in 100 ms. The structure illustrates the neutral phenylalanine [64].

1.2.2.4 **Collision with Electron**

To study the collisions between electrons and cluster or molecular ions, electron targets with different structures have been installed on several ESDs. For instance in the Zajfman trap at Weizmann Institute, an electron target was installed in the field free region, as shown in Figure 1.12 [75]. This target consisted of only electrostatic elements; the interaction region was rectangular, about 7.5 by 50 mm. The electron beam energy E_e was variable from 5 to 30 eV, with typical current of 42 μA at 20 eV and an energy spread of 0.1 eV.

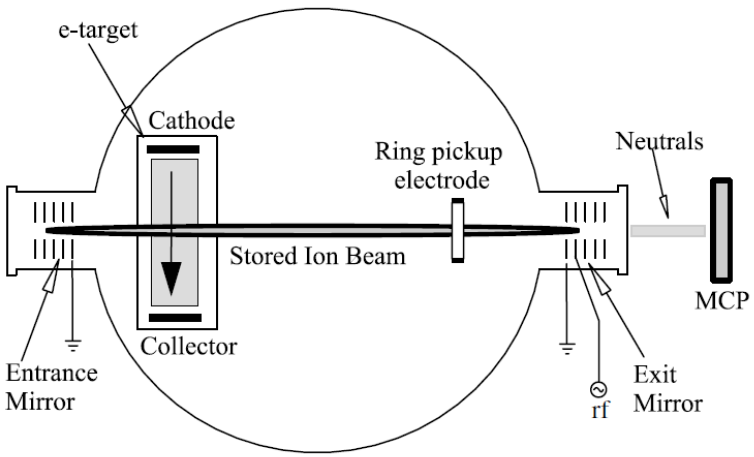

Figure 1.12 Schematic view of the Zajfman trap with an electron target [75].

The electron-impact detachment cross-section was measured for carbon and aluminum cluster anions as a function of the number n of atoms in the clusters (Figure 1.13) [75]. The electron detachment cross-section of carbon clusters shows obvious odd-even oscillations, which is reasonably opposite to the electron binding energy. However, the experimental cross-sections for carbon clusters were found to increase with n, while the theoretical expectation was a global decrease, leading to the increase of the ratio between experimental and theoretical values (Figure 1.13 (c)). In contrast to carbon clusters, the results for aluminum clusters were in good agreement with theoretical predictions, the cross-section decreased for higher electron binding energies, as a function of the number of atoms. The different behaviors of the measured cross-sections between carbon and aluminum clusters suggested that the polarizability should be considered in the theoretical work.

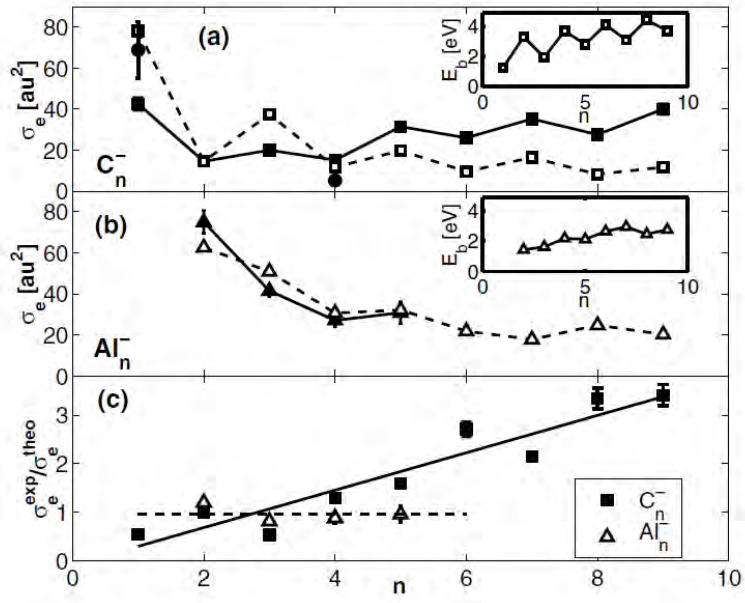

Figure 1.13 Measured electron-impact detachment cross-section σ_e at electron energy 20 eV as a function of the number of atoms n for (a) C_n^- (solid squares) and (b) Al_n^- (solid triangles). The calculated values are plotted as open squares and triangles, respectively. Inserts: electron binding energy for (a) carbon and (b) aluminum clusters as a function of n. (c) Ratio between the experimental and theoretical cross-sections for C_n^- (squares) and Al_n^- (open triangles) at electron energy 20 eV as a function of n. From Ref. [75].

In KEK ESRing, an electron beam target immersed in a uniform solenoid field of 30 G was installed in one of the straight sections [76]. The electron energy is variable from 1 to 100 eV, and the interaction length with stored ions is about 20 cm. The neutral emission in collisions of electrons with peptide cations consisting of 7 to 10 amino acids was measured by Tanabe et al as a function of electron energy from about 1 to 30 eV [77]. A resonance structure was observed at about 6.5 eV (Figure 1.14), and

this structure was ascribed to a resonant electron capture process. It was also observed that the emission rate decreases with a decrease in the number of amino-acid residues, suggesting that only a few bonds in the peptide cations play an important role in the reaction.

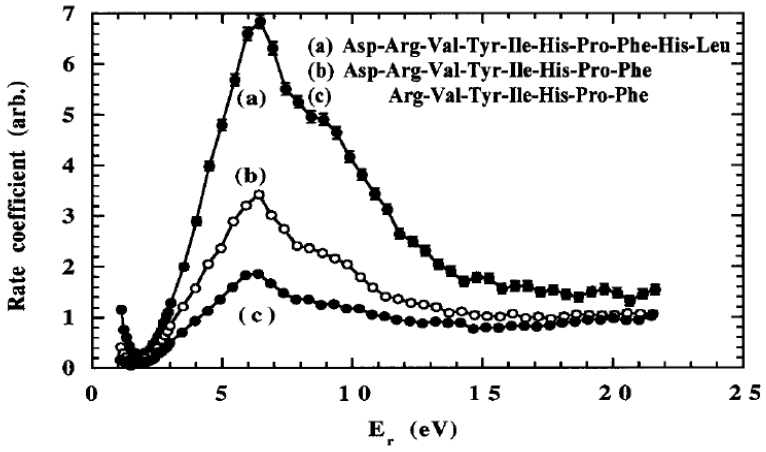

Figure 1.14 Neutral emission rate as a function of electron energy for peptide cations. From Ref. [77].

The electron-anion collisions have been extensively studied in ELISA where an electron beam trap, called ETRAP was installed into one of the straight sections. The thresholds for the formation of neutrals as a function of electron energy have been measured for $Pt(CN)_4^{2-}$ and $Pt(CN)_6^{2-}$ in ELISA, the high electron energy (around 17 eV) indicates the high energetic stability of these multi-charged anions [78]. The cross-section for neutral formation starting from NO_2^-, $NO_2^- \cdot (H_2O)$ and $NO_2^- \cdot (H_2O)_2$ has also been measured in ELISA [79]. These electron-ion collision works performed in ELISA and KEK ESRing had also been reviewed by Tanabe in 2007 [80].

1.2.2.5 **Mass Spectrometry**

As it is well-known, ion bunch stored in an EIBT oscillates between the two electrostatic mirrors, while the ions are almost stopped at their turning points inside the mirrors. Thus, strong effect due to Coulomb interactions among the ions is expected. While studying the motion of ion bunch in Zajfman trap, Pedersen et al have observed two different behaviors of ion bunches: under certain storage conditions, the stored ion bunch can achieve self-bunching mode which maintains a constant width of the ion bunch, or enhanced diffusion leading to fast debunching (Figure 1.15) [81] [82] [83].

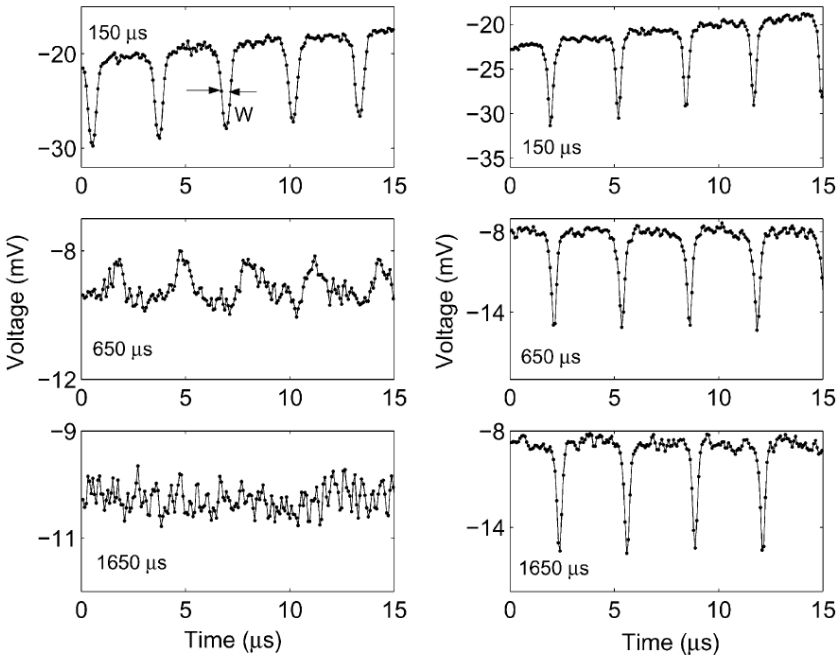

Figure 1.15 Signal observed with the pickup electrode for an initially short bunch of Ar^+ at 4.2 keV for three different time windows of 15 μs after injection. The three left panels are in the debunching mode, while the three right panels are in the self-bunching mode. The initial value of the time window is written in each plot [83].

The interesting self-bunching behavior, also called negative mass instability, has been studied in many experimental and theoretical works [82] [84] [85]. Considering that the revolution frequency of ions in the trap is proportional to the root of ions' charge over mass ratio $\sqrt{q/m}$ and the shape of the bunch is independent of time, a measurement of the oscillation frequency directly yields a mass spectrum of the stored ions [84]. Figure 1.16 presents the frequency spectrum of two isotopes of xenon, $^{131}Xe^+$ and $^{132}Xe^+$, the mass resolution is obtained to be ~ 7×10^{-6}. In principle, the mass resolution of ion trap is proportional to the measuring time, so that even higher resolution is achievable. However, the lifetime of stored ion bunch limits the measuring time. For species with very high and close mass, peak coalescence may take place, leading to a single bunch under the self-bunching mode [84]. As a spectrometer, the resolving power of the ion traps has been discussed and compared with other high resolution mass spectrometers by Zajfman et al [83].

A similar ion trap used as a multi-reflection time-of-flight mass separator (MR-ToF-MS) for the isotope separator ISOLDE/CERN has also been tested by Wolf et al [86] [87]. Figure 1.17 shows a time of flight spectrum of N_2^+ and CO^+ (mass 28.0056 and 27.9944 u, respectively). Mass resolving power as a function of time of

flight is also plotted in the figure, showing that a resolving power up to 80 000 has been achieved.

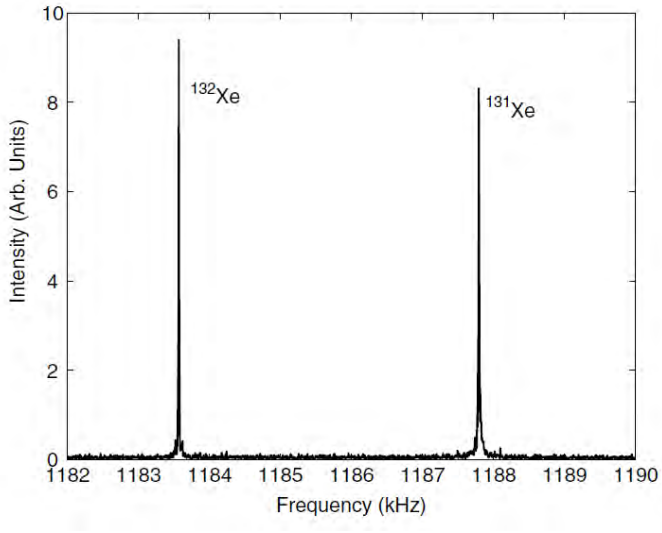

Figure 1.16 Frequency spectrum obtained by fast Fourier transform of the pickup signal when an ion bunch comprising two isotopes of singly charged xenon ions. Only the seventh harmonics are shown. Figure from Ref. [84].

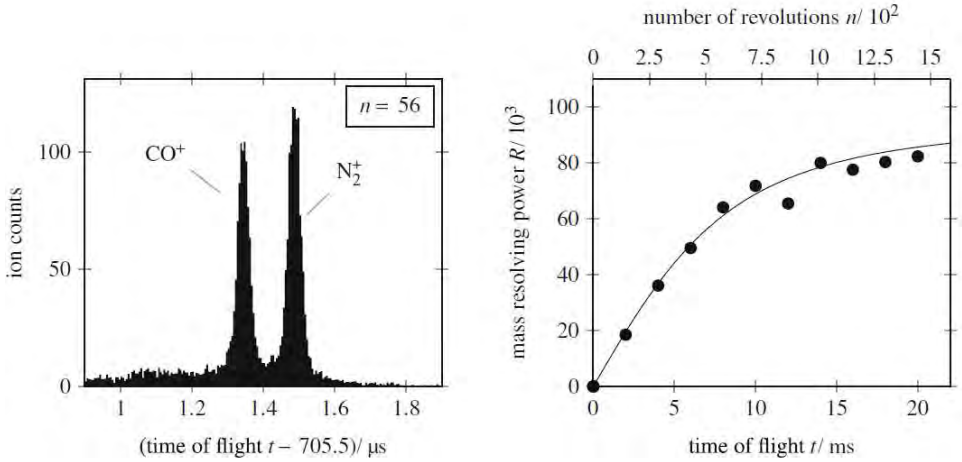

Figure 1.17 Left: ion signal as a function of time of flight demonstrating the mass separation of CO^+ and N_2^+. Right: experimental mass resolving power as a function of time of flight (N_2^+, 2.2 keV) [86].

In the above two subsections, the structures and characteristics of the ESDs, as well as the previous studies carried out on the ESDs have been briefly reviewed. Benefiting from the outstanding features of the ESDs, including short ion revolution

period, long storage lifetime, no mass limitation, self-bunching behavior and so on, these ESDs have demonstrated their great potential in many fields.

Conclusion

The aim of the present work is to study the cooling dynamics of the PAH molecular ions. Choosing anthracene cation from the PAH family as a candidate, we aim to study its cooling regimes over different time ranges. Then a storage device having a short ion revolution period, a long storage lifetime and the ability to store heavy ions is an ideal tool for this study. The Mini-Ring was constructed for this purpose; owing to its small size, the revolution period of 12 keV anthracene cation is only 6.5 μs in Mini-Ring. Therefore, the study of anthracene cation in Mini-Ring can be performed from the very first microseconds up to the second range.

The energy relaxation processes of anthracene cation, including the well-known dissociation and infrared emission processes have been widely studied [88]. Beside these two processes, a fast radiative cooling mechanism has been predicted for the PAH molecules in the ISM environment by Léger et al [89], but no evidence has ever been found yet. In this work, we focus on the radiative cooling processes of anthracene cation, and strive for the experimental evidence of this predicted cooling mechanism.

Chapter 2 Theories and Calculations

The absorption of UV photons is the dominant way of gaining energy for the PAH molecules in the ISM. After the absorption of an UV photon by a molecule, energy redistribution and energy conversion may take place at different time scales. The excess energy can then be dissipated by dissociation, fluorescence emission and/or infrared (IR) emission. These processes will be described in the first section of this chapter. To study the radiative cooling process of the stored molecules, the photodissociation can be employed as a probe to monitor the evolution of the internal energy distribution (IED). In the second section, the Franck-Condon principle, and the photo-absorption spectrum of anthracene cation will be introduced. In the third section, based on the characteristics of the ESD experiments, several calculations will be performed to help us to understand such experiments.

2.1 Energy Relaxation Channels

The interactions of the intermediate size (20 – 50 atoms) PAH molecules and their environment in the ISM have already been extensively studied. Under highly isolated conditions, their absorption of UV photon, cooling by IR emission and collision with ambient gas in a reflection nebula were estimated in the approximate range, $\tau_{UV} \approx 3\times10^4$ s, $\tau_{IR} \approx 3$ s, $\tau_{collision} \approx 5\times10^5$ s, respectively [14] [89] [90]. In this section, the possible processes following the absorption of an UV photon will be discussed. In the first subsection, the energy conversion processes between electronic excitation and vibrational excitation as well as the energy decay processes after absorbing UV photon will be introduced. Following the energy conversion process, the absorbed energy is distributed over vibrational modes, followed by dissociation of small fragments and/or emission of IR photons. These two processes, dissociation and IR emission, will be discussed in the second and third subsections, respectively. The Poincaré fluorescence

predicted by Léger et al in 1988 was considered as a fast cooling process as compared to IR emission. This mechanism will be introduced in more details in the fourth subsection.

2.1.1 **Energy Conversion and Cooling Processes**

The energy transition processes of molecule after the absorption of an UV photon have already been widely studied. Based on the step ladder model describing the electronic and vibrational states of the molecular system [91], the energy transition processes are summarized in Léger's work [89], as shown in Figure 2.1. The electronic states are considered as doublets for simplicity and denoted by D. The electronic levels with higher multiplicity are considered as playing a minor role in PAH cations [92] and will not be discussed here.

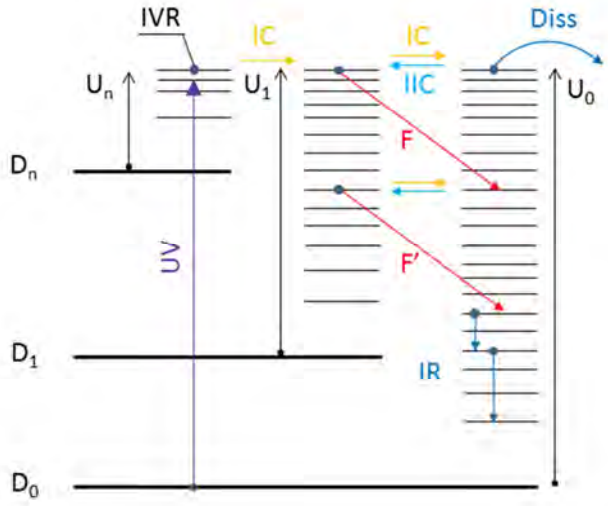

Figure 2.1 Energy level scheme of a large molecular ion with both electronic and vibrational contributions [89]. D denotes doublet; U, vibrational energy level; UV, UV photon absorption; IVR, internal vibrational redistribution; IC, internal conversion; IIC, inverse internal conversion; Diss, dissociation; F and F', fluorescence emission; IR, infrared emission.

For the PAH molecules, after the photon absorption corresponding to the transition from the ground state (D_0, U_0) to an electronic excited state (D_n, U_n), the absorbed energy is distributed on electronic state D_n followed by a rapid internal vibrational redistribution (IVR, 10^{-12} ~ 10^{-10} s) to occupy vibrational states U_n [93]. Then the internal conversion (IC) to vibrational levels of lower electronic states may take place following (D_n, U_n) → (D_{n-1}, U_{n-1}) → (D_{n-2}, U_{n-2}) until the molecule arrives at the ground electronic state (D_0, U_0) with high vibrational energy. Several direct measurements of the IC process have been performed [94] [95], giving a typical time from 10^{-12} s to 10^{-8} s. Beside the fast IC process, the electronic transition with visible

or near infrared photon emission may occur (arrow F in the figure). This process may also bring the molecule back to its ground electronic state (D_0, U_0) but with lower vibrational energy, however the transition rate of this process is usually much lower than that of the IC process.

Once the molecular ion arrives at (D_0, U_0) with high vibrational energy, two relaxation processes may occur. The molecular ion may break and emit fragments like hydrogen atom or small hydrocarbon molecule, this process is called delayed dissociation. The molecular ion may also undergo infrared (IR) emission and emit IR photons. Beside the above two relaxation processes, it is also possible for the molecular ion to transfer backward to (D_1, U_1) by the inverse internal conversion (IIC) process.

For molecules in highly excited states, the probability of presence in one of the degenerate state is proportional to the density of state function $\rho(U)$ which gives the number of accessible levels per unit of energy [96]. The time that a molecular ion spends in a given state (D_0, U_0) or (D_1, U_1) is proportional to $\rho(U)$ [89],

$$\frac{t_1}{t_0} = \frac{\rho(U_1)}{\rho(U_0)}$$

Equation 2-1

If the molecular vibrational modes are known, the density of states $\rho(U)$ can be calculated using analytic approximation, for instance the semi-empirical formula given by Whitten and Rabinovitch in 1960s [97],

$$\rho(U) = \frac{(U + aE_z)^{s-1}}{(s-1)!\prod_i h\nu_i}$$

Equation 2-2

where s is the number of vibrational models, E_z the zero point energy, and $h\nu_i$ are the energies of vibrational modes. The empirical correction factor a ($0 < a < 1$) depends on the ratio U/E_z according to an empirical law in Ref. [97]. In 2008, K. Hansen has improved the calculation of density of states with a saddle point inversion of the canonical partition function [98]. In his work, the density of states $\rho(U)$ is expressed as a function of the microcanonical temperature.

With the calculated densities of states $\rho(U_1)$ and $\rho(U_0)$, the ratio $\rho(U_1)/\rho(U_0)$ is found depending on the size and internal energy of the molecular ion. In the work of Léger et al [89], the ratio $\rho(U_1)/\rho(U_0)$ for a molecule with 18 atoms is found varying

from 10^{-12} to 10^{-5} in the energy range 2 to 10 eV; while for a molecule with 36 atoms this ratio varies from about 10^{-20} to 10^{-7} in the same energy range. These small but not infinity small ratio indicates that the molecular ion system can transfer forward and backward between the two states (D_1, U_1) and (D_0, U_0) by IC and IIC, respectively. For the highly isolated molecular ions like those in the ISM or in the laboratory ultra-high vacuum condition, the IIC process has important consequences on the fluorescence emission. Due to the rare interaction of the molecular ion and its surroundings, the molecular ion system may follow the pathway IIC → fluorescence (F) → IIC → fluorescence (F') and so on, as shown in Figure 2.1. The effective fluorescence emission rate can be expressed as [89],

$$k_{eff} = k_F \frac{\rho(U_1)}{\rho(U_0)}$$

Equation 2-3

where k_{eff} stands for the effective fluorescence emission rate and k_F for the emission rate from D_1 to D_0. This fluorescence emission process is called "Poincaré fluorescence" or "recurrent fluorescence". A remarkable feature of Poincaré fluorescence is that the quantum yield can be larger than 1. That is to say, several photons can be emitted during the cascade after the absorption of one UV photon if the photon energy is large enough.

In this subsection, the possible processes of a PAH molecular ion after UV photon absorption have been briefly introduced. The detailed description and calculation of the three energy relaxation channels: dissociation, IR emission and predicted Poincaré fluorescence will be given individually in the following three subsections.

2.1.2 **Dissociation**

2.1.2.1 **Dissociation Mechanisms, Channels and Pathways**

Following the absorption of an UV photon, a molecule may dissociate via one of the three possible dissociation mechanisms [94]: (a) direct dissociation, (b) predissociation, (c) hot-molecule mechanism. As illustrated in Figure 2.2, when a molecule is excited to a repulsive potential, as shown in (a), the direct dissociation process occurs instantaneously in a time range comparable to its vibrational periods. If it happens that the molecule is excited to a non-dissociative state, but this non-dissociative state is coupled to a dissociative one by internal or external perturbations, as shown in (b); the molecule may transfer to the dissociative state (the dashed line in (b)) and then dissociates, this process is called predissociation [99].

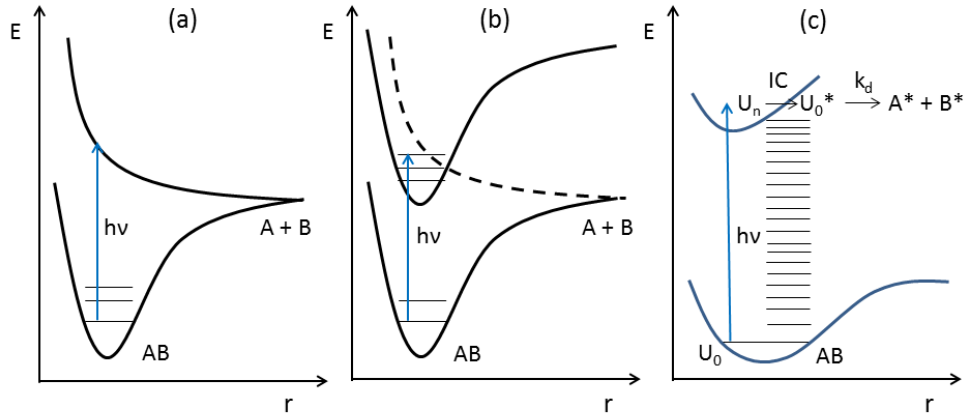

Figure 2.2 Three dissociation mechanisms: (a) direct dissociation, (b) predissociation, (c) hot-molecule mechanism, also called delayed dissociation.

For a PAH molecular ion, as introduced in the last subsection, after UV photon absorption the IVR process and IC process may occur before the dissociation process. As a result, the molecular ion comes back to its electronic ground state with all the absorbed photon energy distributed on its vibrational modes. Then the molecular ion dissociates by the loss of small fragment at a much lower rate compared to that of the other two mechanisms [94], this process is called hot-molecule mechanism or delayed dissociation.

The occurrence of dissociation mechanisms depends on the experimental conditions, the molecular species, the excitation process and excitation energy. For the experiments performed in the ESRs, the observation of the dissociation process typically starts in microsecond time scale, in such time scale, the dissociation process of the PAH molecules is ascribed to the delayed dissociation. Thus, hereafter, the dissociation process we talk about is always referring to the delayed dissociation.

To investigate the dissociation of the PAH molecules, numerous calculations and experiments have been performed. The calculations were dedicated to estimate the dissociation energies, branching ratio among different dissociation channels, and dissociation rate-energy dependence [100] [101] [102]. The experimental techniques like collision induced dissociation (CID) [103], time-resolved photo-ionization mass spectrometry (TPIMS), and mass-analyzed ion kinetic energy spectrometry (MIKES) [104] have been applied to study the dissociation channels and energies. In these experiments, laser pulses or collision with noble gas atoms in CID experiments were employed to excite the PAH molecules in a trap or collision cell, and the charged products were extracted and analyzed by detectors after excitation process. Thus the choices of the irradiation time which determines the deposit energy, and the extraction time may strongly affect the experiments (Fig.7 in Ref. [104]). Recently, a new

method called imaging photoelectron-photonion coincidence spectroscopy (iPEPICO) was developed to study the dissociation process. Using the iPEPICO method, the ejected electrons can be velocity imaged in coincidence with the fragment ion products [105].

The dissociation channels for the PAH molecular ions are known as the loss of hydrogen atom H, molecule H_2 and small hydrocarbon fragments. For instance, the benzene cation undergoes the loss of H, H_2, C_2H_2 and C_3H_3 fragments [106]. Beside the loss of the four fragments above, the naphthalene cation undergoes the additional C_4H_2 loss [107]. For anthracene cation, its dissociation channels are illustrated as following [104],

$$
C_{14}H_{10}^{+} \begin{cases} \rightarrow C_{14}H_9^{+} + H & (1) \\ \quad \hookrightarrow C_{14}H_8^{+} + H & (2) \\ \rightarrow C_{14}H_8^{+} + H_2 & (3) \\ \rightarrow C_{12}H_8^{+} + C_2H_2 & (4) \\ \quad \hookrightarrow C_{12}H_7^{+} + H & (5) \\ \rightarrow C_{11}H_7^{+} + C_3H_3 & (6) \\ \rightarrow C_{10}H_8^{+} + C_4H_2 & (7) \end{cases}
$$

Among all the dissociation channels, the major reactions are the loss of H atom (reaction 1, 2) and C_2H_2 (reaction 4). It is noteworthy that, the daughter cation $C_{14}H_8^{+}$ is mainly produced by sequential loss of H atom from $C_{14}H_9^{+}$ in the microsecond time range (reaction 2), while the loss of H_2 from anthracene cation is a minor process (reaction 3); the formation of $C_{12}H_7^{+}$ is mainly resulting from the H atom loss from $C_{12}H_8^{+}$ (reaction 5) while the contribution of C_2H_2 loss from $C_{12}H_9^{+}$ is less important [104] [105].

According to the structure of anthracene molecule (Figure 2.3), the loss of H atom may result from three possible positions, noted as 1, 2 and 9 in the figure. The critical energy to emit one H atom depends on the corresponding C-H bonds energies, it is found that the average C-H bond energy of different C-H bonds in anthracene cation is slightly lower than the value for position 9 [100] [104]. The dissociation energy for the loss of H of anthracene cation is obtained from the fitting of iPEPICO experiment to be 4.28 eV by West et al [105].

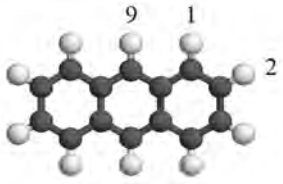

Figure 2.3 Anthracene molecule.

Comparing to the dissociation of H atom, the dissociation of C_2H_2 fragment is more complex, and the isomerization process competes with dissociation. From the energetics point of view, three different C_2H_2 loss pathways have been calculated with density functional theory, the relative energies of the anthracene cation isomers, the three products following different C_2H_2 loss pathways, as well as the associated barriers of the isomerization have been obtained [103], as illustrated in Figure 2.4. Among the three pathways, the shift of one hydrogen atom within the rings plays an important role in breaking the C-C bonds. Although the acenaphthylene (5 in the figure) is the lowest energy structure, the experiments and calculations performed by West et al suggest that the loss of C_2H_2 is from an outer ring of anthracene molecule and the dissociation energy is about 4.2 eV [105].

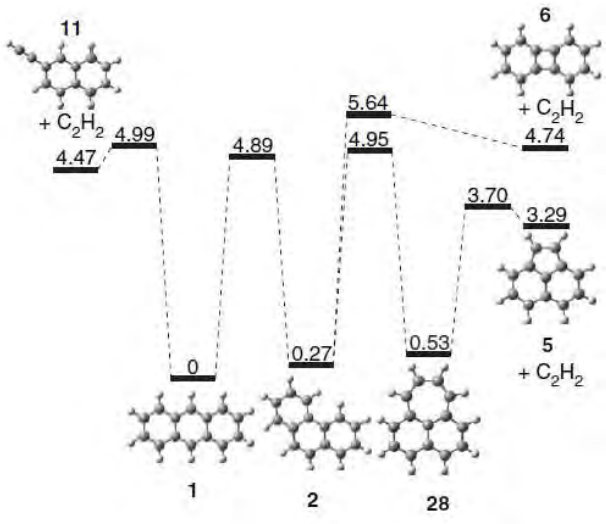

Figure 2.4 Relative energies of the products following the loss of C_2H_2 of anthracene cation and the associated barriers for isomerization, figure from Ref. [103].

2.1.2.2 **Dissociation Rate**

The statistical information of an isolated molecule system is contained in the density of states function $\rho(E)$. The microcanonical temperature T of the system is given by

$$\frac{1}{k_B T} = \frac{\partial}{\partial E} \ln \rho(E)$$

Equation 2-4

where k_B is the Boltzmann constant. For a statistical dissociation process with dissociation energy E_d, the dissociation rate can be expressed as the product of a factor υ by the ratio of the level densities of daughter and parent molecules [96] [108],

$$k(E) = \upsilon \frac{\rho(E - E_d)}{\rho(E)}$$

Equation 2-5

Following the Taylor's theorem, this formula can be written as

$$k(E) \approx \upsilon \frac{1}{\rho(E)} \left[\rho(E) - \frac{d\rho(E^*)}{dE} E_d \right]$$

where E^* stands for an energy value, $E - E_d < E^* < E$, allowing for the estimation of difference between $\rho(E - E_d)$ and $\rho(E)$ in a linear way. As a good approximation, the intermediate value $E - \frac{1}{2} E_d$ is assigned to E^*. Thus we have

$$k(E) \approx \upsilon \left[1 - \frac{d \ln \rho(E - \frac{1}{2} E_d)}{dE} E_d \right]$$

Following the Equation 2-4, the emission temperature T_e corresponding to energy E^* can be defined as

$$\frac{1}{k_B T_e} = \frac{d}{dE} \ln \rho(E - \frac{1}{2} E_d)$$

The dissociation rate then can be expressed as a function of the emission temperature T_e,

$$\begin{aligned} k(T_e) &\approx \upsilon (1 - \frac{E_d}{k_B T_e}) \\ &\approx \upsilon \exp(-\frac{E_d}{k_B T_e}) \end{aligned}$$

Equation 2-6

leading to the famous Arrhenius formula under the approximation $E_d << k_B T_e$. The relation between the emission temperatures T_e and the temperature of the parent molecule T can be obtained by expanding $\frac{1}{k_B T_e}(E - \frac{1}{2}E_d)$ around $\frac{1}{k_B T}(E)$ in a Taylor series, we have

$$\frac{1}{k_B T_e} = \frac{1}{k_B T(E - \frac{1}{2}E_d)}$$
$$\approx \frac{1}{k_B T} + \frac{d}{dT}(\frac{1}{k_B T}) \times (-\frac{1}{2}E_d)$$

Combining with the definition of the heat capacity, $C = \frac{dE}{dT}$, the above equation becomes

$$\frac{1}{k_B T_e} = \frac{1}{k_B T} + \frac{1}{k_B C T^2}\frac{E_d}{2}$$

Then the relation between the emission temperature T_e and parent system temperature T is obtained as,

$$T_e(E) = T(E) - \frac{E_d}{2C}$$

Equation 2-7

The temperature-energy dependence $T(E)$ can be obtained using Equation 2-4, or following the calculation in an earlier work of Cook et al [109]. The heat capacity C of PAH molecules had been calculated by Léger et al, and the ratio $C/C_{\max}$ showed identical curve among different PAH molecules [110]. To fit the capacity data from Léger et al as well as that from NIST [111], a simple numerical curve appears with pretty good accuracy,

$$C = C_{\max}(1 - e^{-\beta T + \theta})$$

Equation 2-8

where $C_{\max} = (3N - 6)k_B$ and N stands for the total number of atoms in the molecule, β = 0.00186 K^{-1} and θ = 0.1327 are the fitting parameters. Alternatively, as in the work of Postma et al, the emission temperature T_e can also be estimated by an approximate equation [112].

For anthracene cation, the two dissociation energies for the loss of H and C_2H_2 have already been discussed in paragraph 2.1.2.1 as 4.28 and 4.2 eV, respectively. The heat capacities for various temperatures can be directly obtained from NIST. If the factor υ is known, then dissociation rate can be calculated as a function of energy E.

In a recent work of West et al [105], the dissociation rate of anthracene cation as a function of energy was calculated using a formula similar to the Arrhenius one,

$$k(E) = \frac{\sigma N^*(E - E_d)}{h\rho(E)}$$

Equation 2-9

where σ stands for the dissociation degeneracy, h is Planck's constant. $N^*(E - E_d)$ is the number of states at energy $(E - E_d)$ which can be counted directly. The calculated dissociation rates for the two channels, the loss of C_2H_2 and H, are plotted in Figure 2.5 [113]. The dissociation rates obtained by West et al will be used in the following work.

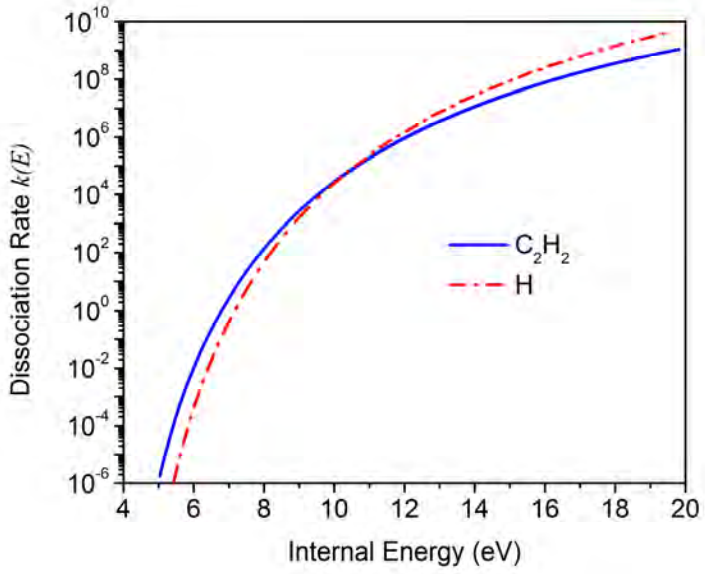

Figure 2.5 Dissociation rate $k(E)$ of anthracene cation as a function of internal energy, dash-dot line, H atom loss; continuous line, C_2H_2 loss [113].

As noticed in the figure, the dissociation rates of both channels increase strongly with internal energy, and cross each other at about 10.5 eV with a rate ~10^5 s^{-1}. By fitting their dissociation rate curves, the pre-exponential factor υ in Equation 2-6 is found about 10^{16} s^{-1}.

In this subsection, the dissociation process of anthracene cation has been discussed in detail. The anthracene cation follows the delayed dissociation mechanism with two major dissociation channels, the loss of H and C_2H_2. Different pathways of the two dissociation channels have been discussed; the dissociation rates as a function of internal energy were recalled.

2.1.3 **Infrared Emission**

Generally speaking, the infrared emission occurs in the ground electronic state (D_0, U_0) with total internal energy E distributed statistically over the whole $3N$-6 vibrational modes, N stands for the number of atoms in the molecule. The infrared emission process of the PAH molecules with internal energy E can be described using a statistical model. Following the work of Boissel et al [88], the IR emission is treated in the harmonic approximation, and the IR emission rate from a specific oscillator i via the transition between two vibrational states ($\upsilon \rightarrow \upsilon$ - 1) is given by $k_{i,\upsilon}$,

$$k_{i,\upsilon} = \upsilon \cdot A_i \frac{\rho^*(U - \upsilon h\nu_i)}{\rho(U)}$$

Equation 2-10

where A_i is the Einstein coefficient of spontaneous emission on the vibrational states υ: 1 → 0 transition, and ρ^* the density of state of the molecule system without the i oscillator. Due to the large number of vibrational modes, the average energy distributed to each mode is low, thus the IR emission from second and higher vibrational states is rare, leading to $\upsilon \approx 1$.

Considering one particular molecule, the emission of an IR photon at mode i leads to an energy decrease through a discrete step of $h\nu_i$. For anthracene, the most intense vibrational frequencies are listed in Table 1, the transition energy is typically about 0.2 eV [88]. However, due to the statistic nature of the energy distribution among a large number of oscillators, it is not possible to determine or predict the exact mode of emission, as a consequence the energy of emission, at a given instant. For an ensemble of molecular ions with internal energy E, an average energy shift rate due to IR emission is therefore defined by summing over the whole set of IR transitions [88],

$$\left[\frac{dE}{dt}\right]_{IR} = \sum_i \sum_\upsilon k_{i,\upsilon} h\nu_i$$

Equation 2-11

Table 1 Harmonic vibrational transitions and Einstein coefficients of anthracene cation [88] [114].

Frequency (cm^{-1})	Energy (eV)	Einstein coefficient (s^{-1})	Attribution
1540	0.1909	2.2	R(CC)
1457	0.1807	2.4	R(CC)
1414	0.1753	48.7	R(CC)
1341	0.1663	41.1	$^{-}$(CC)
1291	0.1601	2.7	$^{-}$(CC)
1188	0.1473	31.6	$^{-}$(CC)
1034	0.1282	4.9	R(CC)
912	0.1131	2.8	^{2}(CH)
748	0.0927	6.9	^{2}(CH)

This energy shift rate corresponds to the ratio of total emission power due to IR transition to the number of molecules in the ion ensemble. Furthermore, due to the large number of oscillators and the statistic nature of the IR emissions, the transition energy and emission rate are not known precisely. Under this model, for internal energy E much higher than the IR emission energy quanta, $E >> h\nu_i$, the internal energy of each molecule follows approximately a smooth variation curve. Therefore, an IR cooling rate η_{IR} can be defined as [88],

$$\eta_{IR} = \frac{1}{E}\left[\frac{dE}{dt}\right]_{IR}$$

Equation 2-12

The calculation performed by Boissel et al shows that the IR cooling rate η_{IR} is almost energy independent, about 2 s^{-1} in a large energy range from 2 to 10 eV, as plotted in Figure 2.6.

2.1.4 **Fluorescence Emission**

For anthracene molecule, the usual fluorescence emission via electronic transition is often considered as a minor process comparing to the IC process. However, for the hot molecules at ground electronic state with high enough internal energy, a small

fraction of population may be produced at electronic excited states via IIC process. Although this population is very small comparing to total molecule population, the Einstein coefficient for spontaneous electronic transition from such electronic excited states could be several orders of magnitude larger than that of the IR emission. Thus, a fast radiative cooling mechanism named as Poincaré fluorescence was proposed by Léger et al in 1980s [89].

Considering a molecular ion with internal energy E at its ground electronic state, the internal energy E is distributed among all the vibrational modes, leading to a density of states $\rho(E)$. The molecular ion could also occupy one of the degenerated vibronic states with electronic excitation energy E_n at the excited state D_n, n = 1, 2, 3... The remaining energy for being distributed to vibrational modes is then reduced to $E - E_n$ and the density of states $\rho(E - E_n)$ is decreased dramatically comparing to $\rho(E)$ of the ground electronic state. Especially when the energy of electronic excited states E_n is high, $\rho(E - E_n)$ could be by several orders of magnitude smaller than $\rho(E)$ [90]. Therefore, the probability of presence of the molecular ion in highly excited electronic states is usually considered negligible.

However, molecular ions with an electron being raised to an excited state D_n, may undergo a fast fluorescence emission with transition energy close to E_n with an Einstein coefficient A_{elec} typically in the order of 10^6 ~ 10^7 s^{-1}. The fluorescence emission rate defined as the product of A_{elec} by the probability of presence in the D_n state may be no longer negligible. Although the number of electronic excited states D_n that could be involved in this process is large, due to the rapid decrease of the density of states with increasing energy E_n at state D_n, the fluorescence emissions from higher electronic states (n > 2) can be neglected. In the work of Boissel et al [88], only the transitions from D_2 were considered since the transitions from D_1 to D_0 are forbidden. Between D_2 and D_0, several vibronic transitions can be involved, as shown in Table 2, the data obtained from absorption spectroscopy were recalled here [114]. For instance, the first available transition $E_{elec,1} = E_2 = 1.71\,\text{eV}$ corresponds to the pure electronic transition from D_0 to D_2, while the second transition $E_{elec,2} = 1.88\,\text{eV}$ at slightly higher energy corresponds to a transition involving the excitation of a vibrational mode by $\Delta\upsilon = 1$. In the work of Boissel et al, the transition wavelengths obtained in the absorption experiments were directly used in the calculations of emission. The fluorescence emission rate $k_{elec,j}$ for each transition was defined as the product of $A_{elec,j}$ by the probability of presence of molecular ion in the corresponding vibronic states for which the available vibrational energy is $E - E_{elec,j}$,

$$k_{elec,j} \approx A_{elec,j} \frac{\rho(E - E_{elec,j})}{\rho(E)}$$

Equation 2-13

Table 2 Vibronic transitions, oscillator strengths and Einstein coefficients of anthracene cation [88] [114]. The transitions are noted as j = 1, 2, 3...for simplicity.

Symmetry	j	Average Wavelength (nm)	Oscillator Strength	A_{elec} (s^{-1})
^2A_u (D_2)	1	724	0.055	7.0×10^6
	2	660	0.021	3.2×10^6
	3	610	0.009	1.6×10^6
	4	540	0.009	2.1×10^6
$^2B_{1u}$ (D_4)	5	432	0.026	9.3×10^6
$^2B_{1u}$ (D_5)	6	350	0.052	28×10^6
	7	336	0.048	28×10^6
^2A_u (D_6)	8	315	0.187	125×10^6

Due to the fast decrease of $\rho(E - E_{elec,j})$ with increasing $E_{elec,j}$, the fluorescence emission rate for $j \geq 3$ are much smaller than for j = 1 and 2. In fact, the $k_{elec,j}$ from transitions with $j \geq 3$ in Table 2 are less than 1% of $k_{elec,1}$. Thus only the first two transitions (j = 1, 2) from D_2 were included in their calculations.

In contrast to IR emission, due to the large photon energy released by each electronic transition, the fluorescence emission should not be described as a continuous energy decrease. However, based on a large molecular ion ensemble at the same initial energy, a mean fluorescence cooling rate can still be defined as following [88],

$$\eta_{elec} = \frac{1}{E}\left\lfloor \frac{dE}{dt} \right\rfloor_{elec} = \frac{1}{E}\sum_j k_{elec,j} E_{elec,j}$$

Equation 2-14

The calculated fluorescence cooling rate together with the IR emission rate are presented in Figure 2.6. As noticed, in the low energy range E < 5 eV, the cooling is dominated by IR emission; while above 5 eV, the fluorescence emission becomes the dominant cooling process.

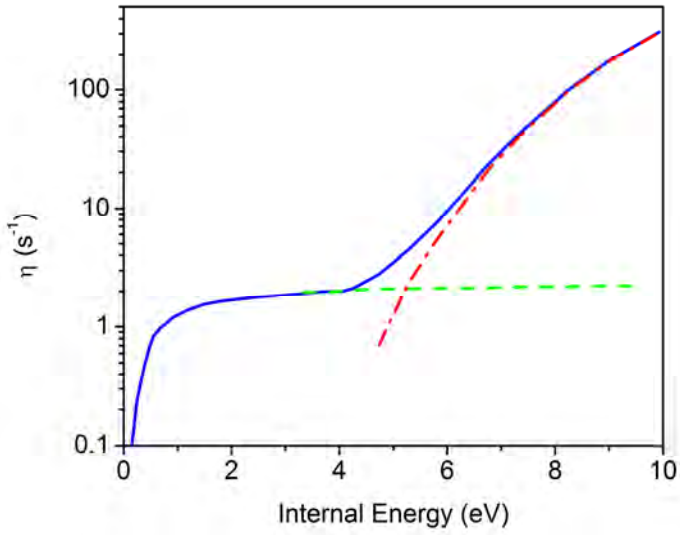

Figure 2.6 Radiative cooling rates of isolated anthracene cation as a function of internal energy. Green dash line: IR cooling; red dash-dot line: fluorescence cooling rate; solid line: total cooling rate including both of IR and fluorescence emission [88].

In this section, three energy relaxation channels including delayed dissociation, fluorescence emission and IR emission of the isolated PAH cation after absorbing an UV photon have been discussed. The dissociation mechanisms, channels and pathways as well as the dissociation rate versus internal energy have been discussed. The mechanisms of the radiative cooling processes, the fluorescence emission and IR emission have also been explained. More particularly, following the work of Boissel et al, the mean cooling rates of fluorescence emission and IR emission have been compared.

2.2 Photon Absorption of Anthracene Cation

To study the radiative cooling of molecular ions, the direct way would be to count the emitted visible or infrared photons. However, the fluorescence emission and IR emission occur with typical times around tens of milliseconds and seconds, respectively, ion storage techniques are needed in such a long time scale. In addition, the direct measurement of the emitted photon, suffering from the poor signal counts comparing to background, and/or from the low collection efficiency, is difficult to perform.

On the other hand, the easy detection of keV neutral particles from ESRs due to the delayed dissociation process makes it possible to study the radiative cooling of the molecular ions by monitoring the neutral yields and estimating its internal energy distribution (IED). In general, laser pulses, electrons and ions can be employed to excite the stored molecular ions to probe its IED as a function of time. Considering the ease of use and precise energy deposit, the laser pulse is chosen to excite the PAH cation. Therefore, in this section the photon absorption of anthracene cation will be discussed.

2.2.1 **Franck-Condon Principle**

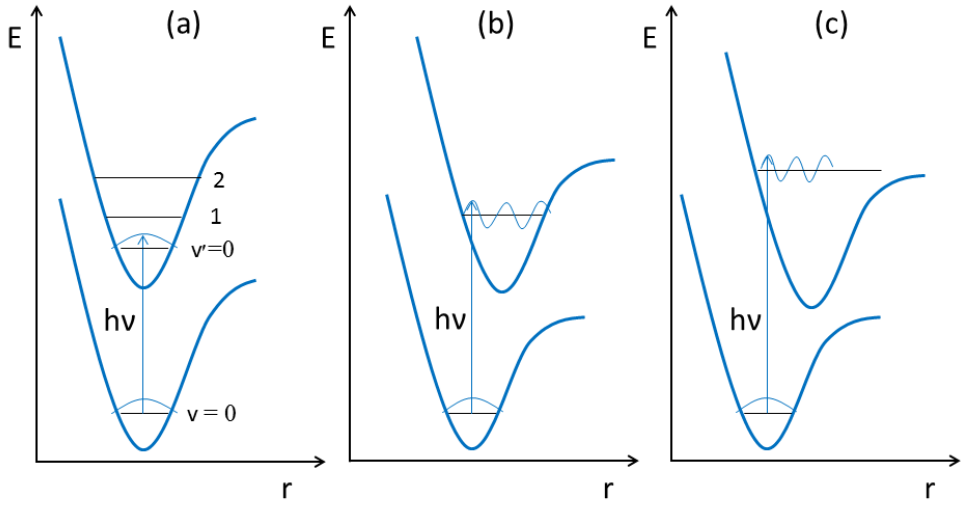

Figure 2.7 Three different potential curves of diatomic molecules.

The absorption of a photon by a molecule (or molecular ion) follows the well-known Franck-Condon principle. The principle, combined Franck's main idea and Condon's development is expressed as following: the electron jump in a molecule takes place so rapidly in comparison to the vibrational motion that immediately afterwards the nuclei still have very nearly the same relative position and velocity as before the jump [115]. Taking the diatomic molecules as example, three typical cases of the potential curves of molecules with upper and lower electronic states are illustrated in Figure 2.7 to show the application of the Franck-Condon principle [115].

In Figure 2.7 (a) the minima of the potential curves of two electronic states locate nearly one above the other, showing that the internuclear distance hardly changes between the two electronic states. In absorption, the molecule is initially populated at the lowest vibrational state $v = 0$, the transition to the lowest vibrational state ($v' = 0$) of the upper potential curve fulfils the requirement of the Franck-Condon principle.

The transition to a higher state (ν′ = 1, 2, 3...) occurs only when, the position or velocity or both, of the atoms in the molecule take appreciable changes at the moment of the electron jump. For the vibrational state ν′ = 1, the necessary change of position or velocity is comparatively small, so the transition 1 - 0 can appear but with lower probability than the 0 - 0 transition. With increase vibrational state (ν′ = 2, 3...), the necessary change of position or velocity increases, leading to the decrease of transition probability. The distribution of the transition probability is illustrated in Figure 2.8 (a).

In Figure 2.7 (b), the minimum of the upper potential curve locates at a greater *r* value than that of the lower one. Therefore, the most probable transition is no longer the transition 0 – 0 but the one vertically upwards ν′ - 0 since no position or velocity change is needed for this transition. For the transition to the neighborhood states ν′ +1 and ν′ -1 at the upper potential curve, the transition probability will reduce because of necessary small change of position or velocity. Then the transition probability is distributed as that in Figure 2.8 (b).

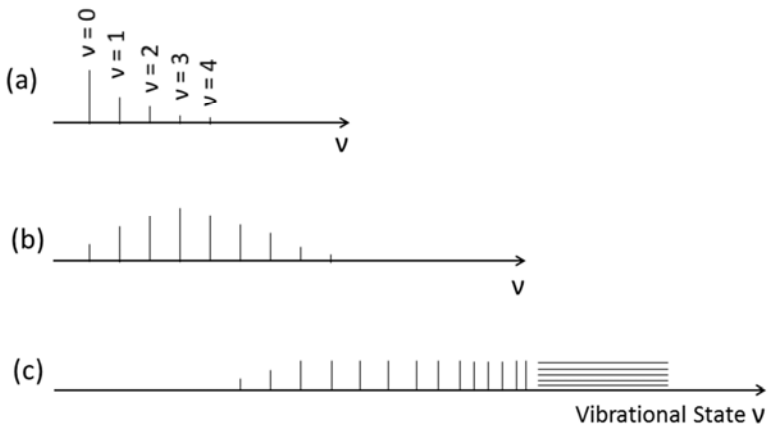

Figure 2.8 Three typical cases of the distributions of the absorption probability.

In Figure 2.7 (c) the minimum of the upper potential curve locates at a greater internuclear distance. The transition which strictly fulfills the Franck-Condon principle leads to an energy level above the dissociation energy (the limit of the asymptotic curve), the atoms will fly apart after the electron jump. Above the dissociation energy, the transition shows continuous behavior. The transition to neighborhood lower vibrational state is also possible. The distribution of transition probability is illustrated in Figure 2.8 (c). If we compare the cases (b) and (c) we may notice that, the transition probability to high vibrational states varies slower with ν, which is due to the increase of density of states with ν.

In summary, according to the Franck-Condon principle, the most probable transition from ν is always corresponding to the lowest potential curve vertically upward in the potential curve schematic.

2.2.2 **Franck-Condon Profile of Anthracene Molecule**

The Franck-Condon principle is explained above for the diatomic molecules. For anthracene cation with twenty-four atoms, the potential as a function of the internuclear distances should be a multi-dimension surface which is not easy to draw. However, the Franck-Condon profile of anthracene for certain electronic transition can still be experimentally measured or calculated by theoretical models. Figure 2.9 presents the Franck-Condon profiles of the $^1A_g \rightarrow {}^1B_{2u}$ (S_0 - S_1) transition of anthracene molecule calculated at 500 K, 300 K, 100 K and 0 K, respectively [116]. The experimental absorption spectrum of the $S_0 - S_1$ transition of anthracene molecule obtained by Ferguson et al [117] at around 400 K is rescaled and plotted in (b) to compare with the calculated one.

As noticed, at low temperature (d) 0 K, the Franck-Condon profile presents several sharp absorption peaks corresponding to the transitions to different vibrational states which fit well the Franck-Condon principle. Among these absorption peaks, there are several absorption valleys. When the temperature increases, the absorption valleys start to be covered by the neighboring absorption peaks, and the absorption profile tends to a smooth curve, for instance at (a) 500 K the absorption profile can be considered approximately as one broad peak with FWHM of about 0.5 eV. According to the Boltzmann distribution, when the temperature increases, the number of oscillators being excited increases at S_0. This brings more possible transition channels in the absorption process. As a result, the absorption peaks are expanded in width when the temperature increases, leading to the smooth absorption profile at high temperature. In addition, the initially excited oscillators of S_0 at high temperature also lead to the small expansion of the absorption profile at $\tilde{\nu} - \tilde{\nu}_0 < 0$ side.

The Franck-Condon profile shows the wavenumber selectivity around certain electronic transition of a molecule. If the given wavenumber is inside the absorption profile, the absorption is relatively easier to occur; otherwise, the absorption might be rare. Due to the fact that the absorption profile tends to a smooth curve with increasing temperature, we can deduce that the absolute value of the absorption cross-section at a given wavenumber varies slower and slower with increasing temperature. Note that, the temperature of a molecule is tightly related to its internal energy. That is to say, the absorption cross-section of a given wavenumber for anthracene molecule tends to be constant when the molecule is relatively hot. Due to the fact that the vibrational structures of anthracene molecule and cation are very close [88], we extend the above analysis from anthracene molecule to cation. In the following, for hot anthracene cations with energy difference of 1 ~2 eV, the absorption cross-section of a given photon is assumed to be constant.

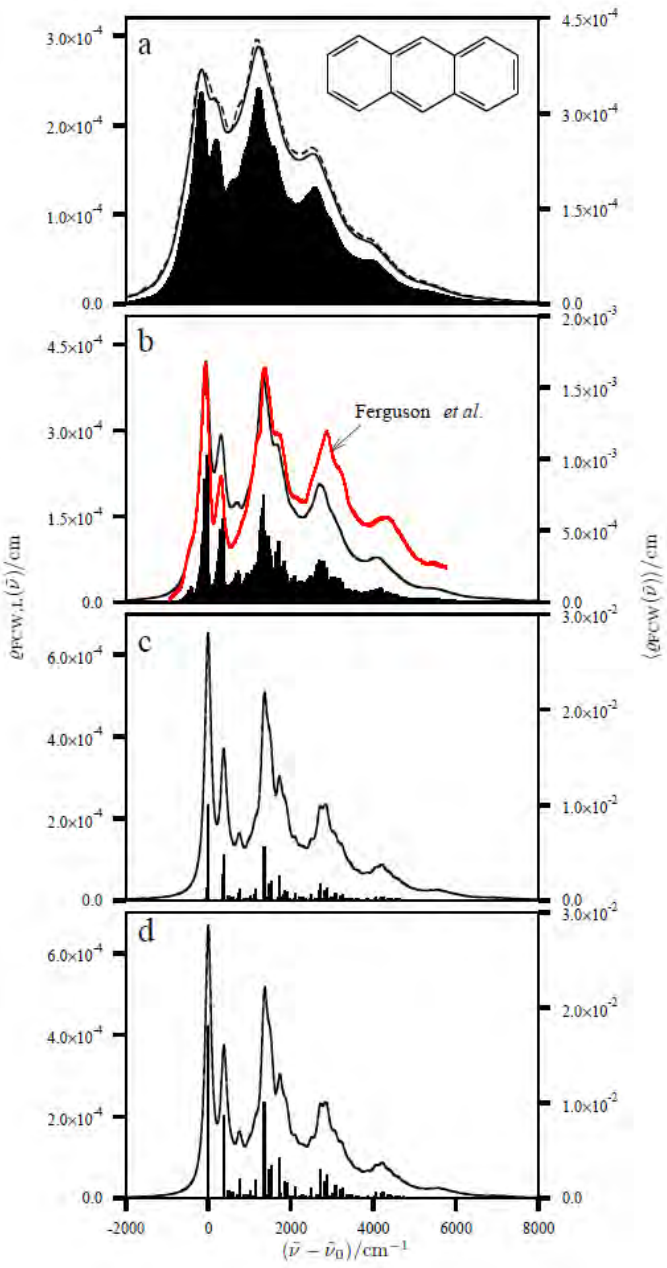

Figure 2.9 Calculated Franck-Condon profiles for the $^1A_g \rightarrow {}^1B_{2u}$ (S_0 - S_1) absorption spectra of anthracene molecule at (a) 500 K, (b) 300 K, (c) 100 K and (d) 0 K. Each line in the stick spectra (right axis) represents the averaged Franck-Condon weighted density of states. The stick representations have additionally been convoluted with Lorentzian line shapes with FWHM of 180 cm^{-1} (solid curve, left axis) and compared with the results obtained from the TCF approach (dashed curve, left axis). Here $\tilde{\nu}_0$ corresponds to the wavenumber of the 0 - 0 transition for the UV absorption band. The experimental UV absorption spectrum of Ferguson et al [117] is additionally compared with the Franck-Condon profile at 300 K in (b). Figure from page 67 of Ref. [116].

2.2.3 **UV Absorption Spectrum of Anthracene Cation**

The photo-absorption spectra of the PAH molecules including their respective anions, cations and dications can be theoretically calculated. Based on the time-dependent density functional theory (TD-DFT), Malloci et al have calculated the photo-absorption cross-section of anthracene cation, as plotted in Figure 2.10 [118] [119]. In their calculated spectrum, an absorption cross-section of about 10^{-18} cm^2 was suggested at around the energy of the second/third harmonic photon. By employing the multilayer multiconfiguration time-dependent Hartree (ML-MCTDH) algorithm, Meng et al have simulated the six lowest-lying electronic states of anthracene cation in full dimensionality [120]. Although the absolute value of the cross-section was not given in their work, the vibronic structures of each electronic state were clearly shown.

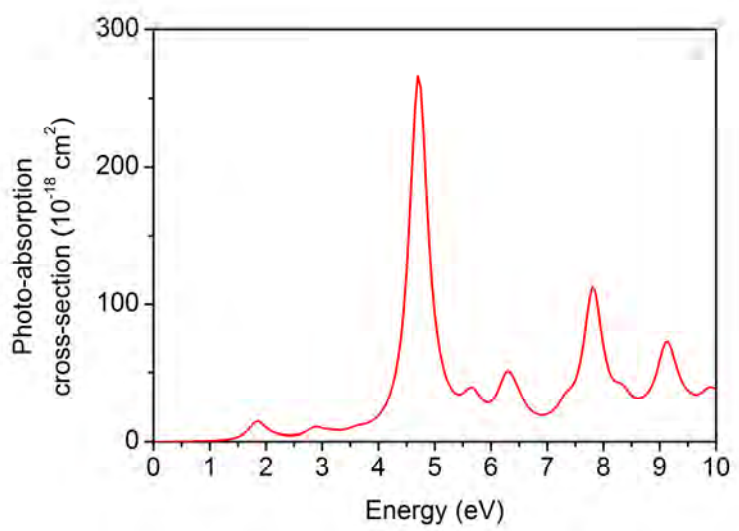

Figure 2.10 Computed photo-absorption cross-section of anthracene cation [118].

The photo-absorption spectra of anthracene cation have also been obtained experimentally by Szczepanski et al in Ar matrices at 12 K [114]. In their experiments, a small amount of CCl_4 was added to the isolator Ar gas with a ratio: Anthracene/CCl_4/Ar = 0.7/1/300. The near-UV absorption spectra of anthracene plus anthracene cation in the Ar matrix before and after 5 min Hg lamp photolysis for 30 min deposition were presented here in Figure 2.11 (A) and (B), respectively, the net UV spectrum of anthracene cations (C) was obtained by subtracting (B) from (A).

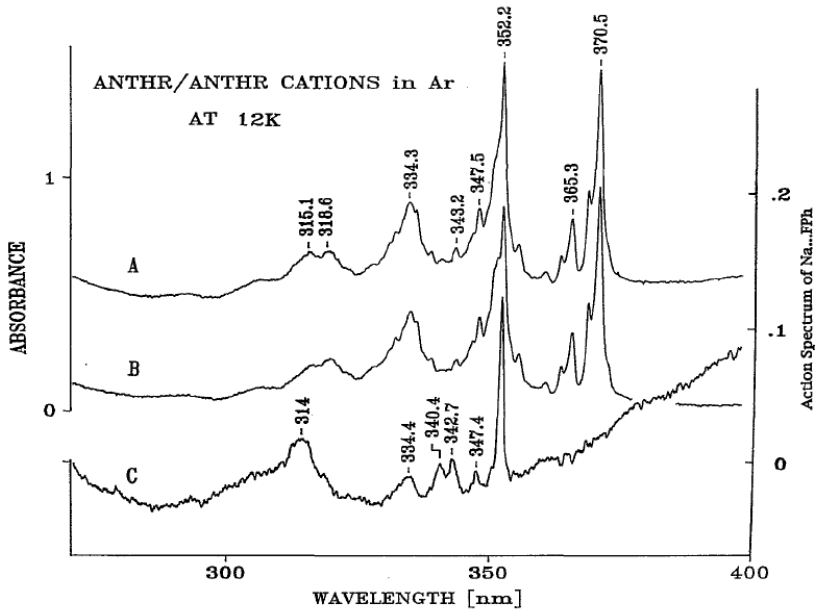

Figure 2.11 UV absorption spectrum of anthracene plus anthracene cation in the Ar matrix (A) before and (B) after 5 min Hg lamp photolysis for 30 min deposition. (C) Net UV absorption spectrum of anthracene cation obtained by subtracting (B) from (A) [114].

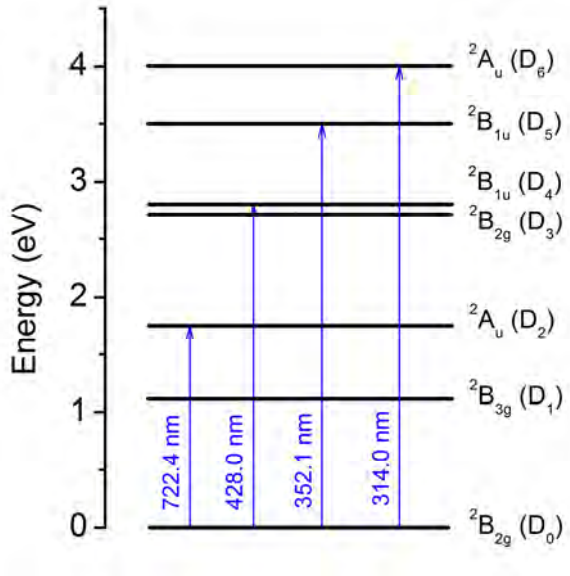

Figure 2.12 Energy diagram of the electronic doublet state system of anthracene cation, the transitions $D_0 \rightarrow D_1$ and $D_0 \rightarrow D_3$ were not shown because of symmetry forbidden [114].

In this UV absorption spectrum, the two absorption peaks at 352.1 and 314.0 nm were assigned to $^2B_{2g}$ (D_0) → $^2B_{1u}$ (D_5) and ^2A_u (D_6) transitions respectively [114]. In addition, the energy diagram of anthracene cation was shown in Figure 2.12, note that the transitions $D_0 \rightarrow D_1$ and $D_0 \rightarrow D_3$ were not shown because of symmetry forbidden.

Considering the relative absorption efficiency, the photon wavelength close to 352.1 nm, for instance the third harmonic photon of a Nd:YAG laser equipment (355 nm, 3.5 eV) is expected to be a good choice to excite the anthracene molecular cation. Although the absorption peak at 12 K is narrow, at much higher temperature, the Franck-Condon profile is expected to be broader as discussed in the last subsection.

In this section, the Franck-Condon principle has been recalled, and the Franck-Condon profile for the $S_0 - S_1$ transition of anthracene molecule has been discussed. As an assumption, for hot anthracene cations with energy difference of 1 ~2 eV, the absorption cross-section of a given photon is considered to be constant. The UV absorption spectra of anthracene cation have been recalled and discussed; the third harmonic photon is expected to be a good choice to excite the anthracene cation.

2.3 Calculations on Anthracene Cation

In the above two sections, the energy relaxation channels of isolated PAH molecular ions have been discussed and the photodissociation process has been chosen as a probe to study the cooling dynamics of anthracene cation. Based on the knowledge of the ESR experiments, several primary calculations on anthracene cation will be performed in this section. The calculations mainly concern the neutral yields $I(t)$, IED $g(E,t)$ (ion population per unit energy at E, at time t) and the time t, as illustrated in Figure 2.13. Considering the revolution period 6.5 μs of anthracene cation (12 keV) in Mini-Ring, the calculation time starts from half of the revolution period, with step of one revolution period 6.5 μs.

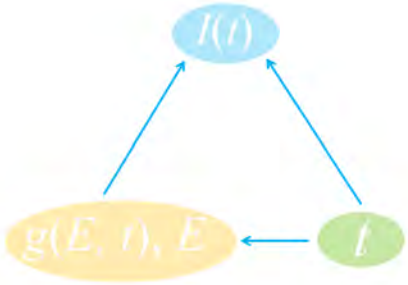

Figure 2.13 Illustration of the relations among the neutral yields, IED (or energy E) and time.

Considering a group of molecular ions with energies between E and $E+\Delta E$, the ion population $N = g(E,t)\Delta E$, then population depletion due to dissociation follows the well-known decay law $\frac{dN}{dt} = -k_{diss}(E)N$, leading to

$$g(E,t) = g_0(E)e^{-k_{diss}(E)t}$$

Equation 2-15

where $g_0(E)$ stands for the initial population per unit energy at E, and $k_{diss}(E)$ for dissociation rate which has already been discussed in paragraph 2.1.2.2. The lifetime of the molecular ion τ due to dissociation is inversely proportional to $k_{diss}(E)$, $\tau(E) = 1/k_{diss}(E)$. As we know, the dissociation rate increases strongly with internal energy, leading to the rapid decrease of lifetime of the molecular ion with internal energy. Taking the dissociation channel of C_2H_2 as an example (same for all the calculations hereafter), the lifetime of anthracene cation is presented in Figure 2.14 as a function of internal energy. For the molecular ions with internal energy 9.5 eV the lifetime τ is about 100 μs, while for molecular ions with internal energy 12 eV, the lifetime τ is only 1 μs.

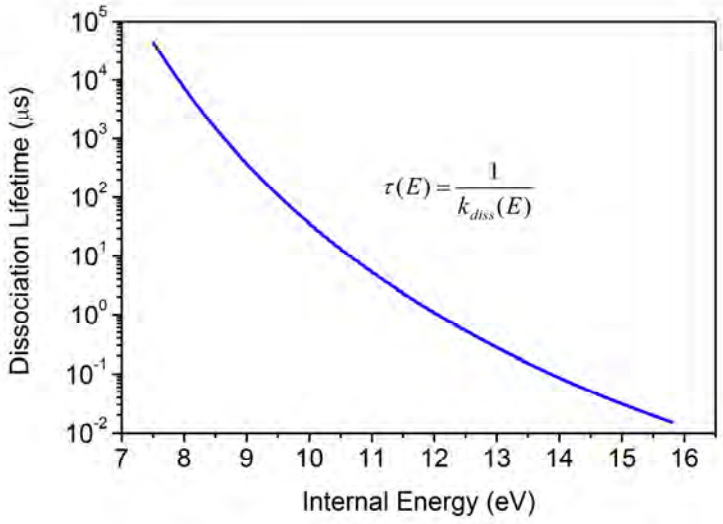

Figure 2.14 Lifetime of molecular cations limited by the dissociation channel of C_2H_2, note the logarithm scale for lifetime.

2.3.1 **High Energy Edge**

Due to the fact that the molecules with higher internal energy are expected to dissociate faster, the IED of a molecule ensemble will be depleted at high energy part

as a function of time, leading the IED as shown in Figure 2.15 with a high energy edge. However, the molecules with very low energy hardly dissociate, it is difficult to know the exact shape of the low energy part of the IED. Here the low energy part of IED was assumed to be flat for simplicity, although a different shape can be expected.

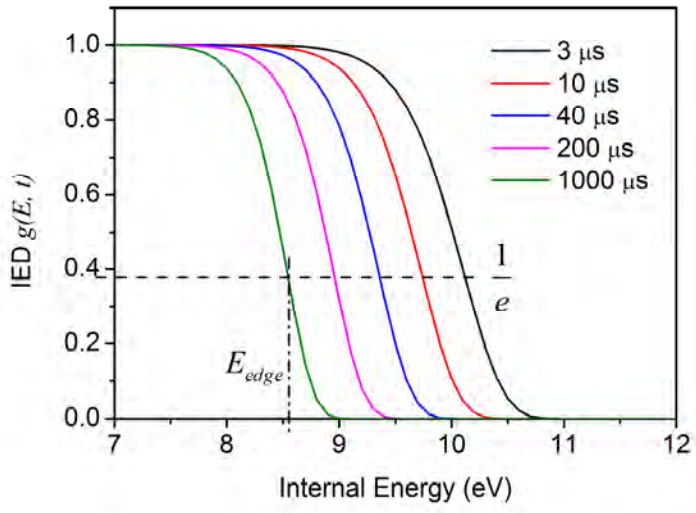

Figure 2.15 The IED at different time, the vertical scale is normalized to 1.

As a first order approximation, the initial energy distribution of the molecular ion ensemble is assumed to be flat, noted as $g_0(E)$. The remaining IED $g(E,t)$ at time t is characterized by the high energy edge E_{edge} which was defined as following,

$$g(E_{edge},t)=\frac{1}{e}g_0(E)$$

Equation 2-16

Comparing with Equation 2-15, we have

$$g(E_{edge},t)=g_0(E)e^{-k(E_{edge})t}=\frac{1}{e}g_0(E)$$

Then we obtain

$$k(E_{edge})=\frac{1}{t}$$

Equation 2-17

Combining with the dissociation rate expressed in Arrhenius form (Equation 2-6, Equation 2-7), together with a linear approximation $T=E/C$, the expression of $E_{edge}(t)$ as a function of time is obtained,

$$E_{edge}(t) = \frac{E_d C}{K_B} \times \frac{1}{\ln(\upsilon t)} + \frac{1}{2} E_d$$

Equation 2-18

As plotted in Figure 2.16, the high energy edge E_{edge} of the IED is about 10.1 eV at 3 μs, giving a rough estimation of the IED at certain time. In addition, E_{edge} decreases with time, indicating the shift of the IED when only dissociation is considered.

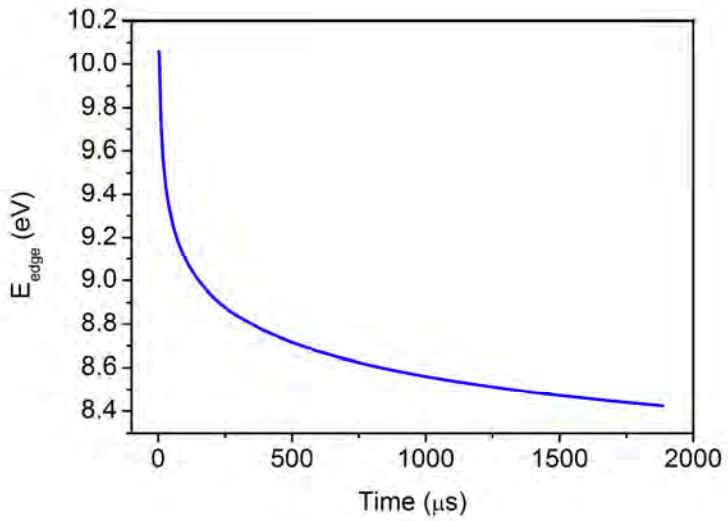

Figure 2.16 High energy edge E_{edge} as a function of time.

2.3.2 Time Dependency of the Neutral Yield

The neutral yields result from the dissociation of the molecular ions. For the molecular ions with energy between E and $E + \Delta E$, their contribution to the neutral yield in a time interval t, $t + \Delta t$ is

$$\Delta i = -N(E,t) = -\frac{d(g(E,t)\Delta E)}{dt}\Delta t$$

Injecting the derivative of Equation 2-15 by time, we have

$$\Delta i = k_{diss} g_0(E) e^{-k_{diss}(E)t} \times \Delta E \Delta t$$

Equation 2-19

Thus the neutrals emitted per unit time by the ion population per unit energy at E can be expressed as,

$$i(E,t) = \frac{\Delta i}{\Delta E \Delta t} = k_{diss}(E) g_0(E) e^{-k_{diss}(E)t}$$

Equation 2-20

From the point of view of whole energy range, the $i(E,t)$ stands for the contribution to the neutral yield from ion population at energy E. The contributions of the molecular ions with different internal energies 8.5, 9.0, 9.5 10.0 and 10.5 eV as a function of time are plotted in Figure 2.17, the sum of their contributions, i.e., the total neutral yield is also plotted in the figure.

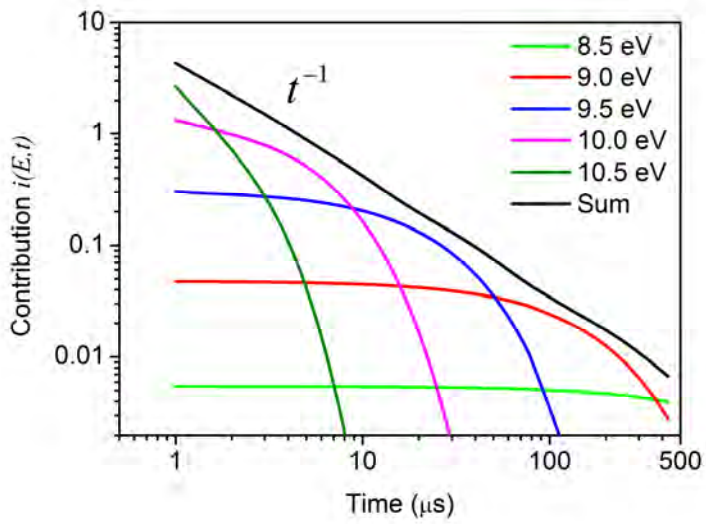

Figure 2.17 Total neutral yields (black line) and the contributions to the neutral yields from molecular ions with internal energies 8.5 (green curve), 9.0 (red curve), 9.5 (blue curve), 10.0 (magenta curve) and 10.5 eV (olive curve) as a function of time, note the log-log scales.

It is noticed that the molecular ions with high internal energy mainly contribute to the total neutral yield at short time while the molecular ions with low internal energy dominate the contribution at long time. In addition, the total neutral yield follows a straight line in the log-log scales, showing a t^{-1} behavior. By summing over the contributions from the whole internal energy range, the total neutral yield $I(t)$ is expressed as,

$$I(t) = \int i(E,t) dE$$

$$I(t) = \int k_{diss}(E) g_0(E) e^{-k_{diss}(E)t} dE$$

Equation 2-21

Following earlier works [60] [64] [67], when the IED of the molecular ion ensemble $g_0(E)$ is broad, the neutral yield $I(t)$ due to thermal dissociation follows the t^{-1} law. The following is one of the demonstrations:

We define a function $f(E) = k_{diss}(E)e^{-k_{diss}(E)t}$, and then the Equation 2-21 can be written as

$$I(t) = \int g_0(E) f(E) dE$$

The maximum value of function $f(E)$ lies on the energy where $k_{diss}(E) = \frac{1}{t}$, as shown in Figure 2.18. According to the Equation 2-17, this maximum value lies actually on the high energy edge E_{edge} of the IED, thus the maximum value $f(E_{edge}) = \frac{1}{t}e^{-1}$.

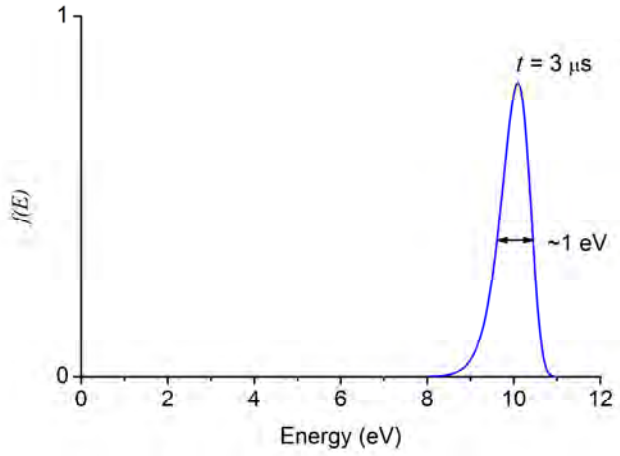

Figure 2.18 Function $f(E) = k_{diss}(E)e^{-k_{diss}(E)t}$ calculated at t = 3 μs.

Since $g_0(E)$ is broad, then the neutral yield $I(t) = \int g_0(E) f(E) dE$ follows the maximum of $f(E)$ at a given time t. In addition, the function $f(E)$ shows a narrow peak located at E_{edge} (Figure 2.18), thus the $I(t)$ can be expressed approximately as a delta function,

$$I(t) \approx \int g_0(E) f(E_{edge}) \delta(E - E_{edge}) dE$$

leading to $I(t) \approx \frac{1}{t} e^{-1} g_0(E_{edge})$. Therefore, the neutral yield $I(t)$ is close to the distribution,

$$I(t) \propto \frac{1}{t}$$

Equation 2-22

2.3.3 **Main Contribution Energy**

In the above subsection, the contributions to the total neutral yield from molecular ions with different internal energies have been calculated as a function of time. Conversely, at a given time *t*, the contributions to the total neutral yield $dI(E)$ can also be calculated as a function of the internal energy of the molecular ions. As plotted in Figure 2.19, the contributions are calculated at several times 3, 10, 16 and 42 μs, the integral of each curve over energy is the total neutral yield $I(t)$ at corresponding time. At *t* = 3 μs, the maximum contribution to $I(t)$ is found at 10.1 eV. On the other hand, from the formula of E_{edge} (Equation 2-18) we obtain that E_{edge} (3 μs) = 10.1 eV. This is a convincing evidence that the maximum contribution to the total neutral yield is provided by the molecular ions with internal energy $E \approx E_{edge}(t)$; the same conclusion can be obtained from the contribution curves at other calculated times.

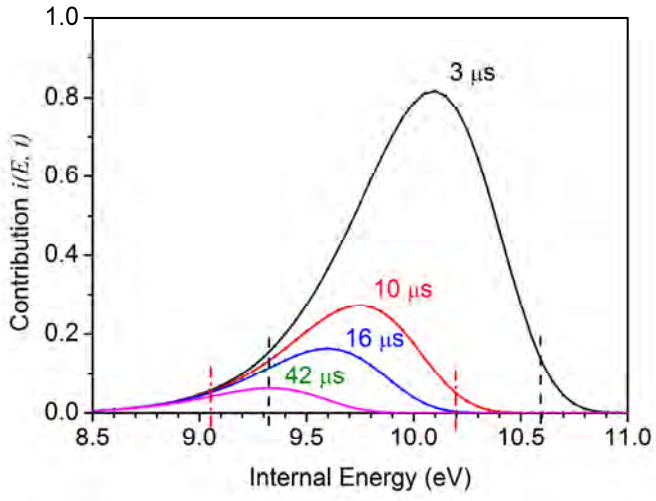

Figure 2.19 Contributions to the neutral yield at given times as a function of the internal energy. The black dash line and red dash-dot line stand for the edges of the main contribution region at 3 and 10 μs, respectively.

On the contribution curve at t = 3 μs in Figure 2.19, if we choose 20% of the maximum contribution $dI(E) = 20\% \times dI(E_{edge})$ as the edge of the main contribution region, we obtain an energy region 9.35 < E < 10.6 eV noted as black dash lines in the figure. Similarly at t = 10 μs, another energy region 9.05 < E < 10.2 eV is obtained (red dash-dot lines). We deduce that there exists a main contribution energy region in width of about 1.2 eV at each calculation time, and this energy region shifts to lower energy as a function of time.

In order to follow the main contribution energy region as a function of time, the energy values at the center of each peak in Figure 2.19 are plotted as a function of time in Figure 2.20. This curve is of importance for understanding the relation between the internal energy and the signal collection time in the ESR experiments. For instance, the center value of the main contribution energy at 20 μs is 9.5 eV, that is to say the collected neutral yield at around 20 μs mainly comes from the molecular ions with internal energy at about 9.5 eV. If the collection of neutral yield starts from 20 μs, then the collected neutral yield is only sensitive to the ion population with internal energy lower than 9.5 eV.

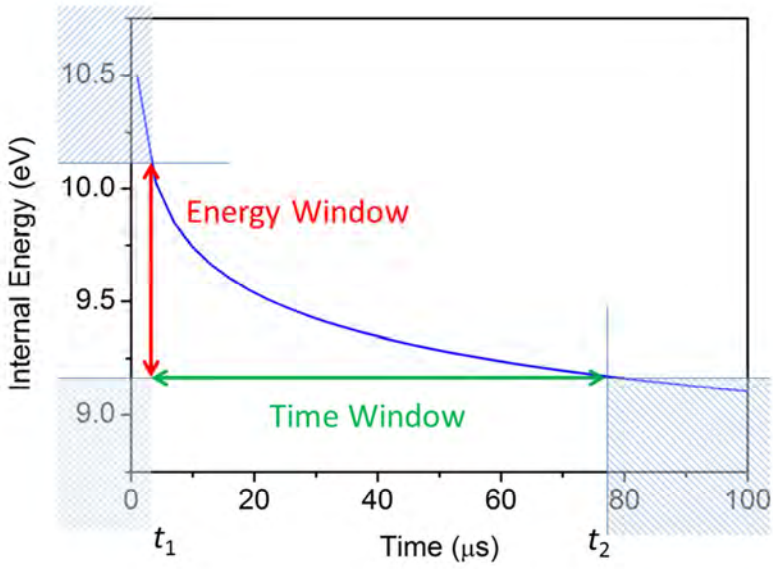

Figure 2.20 Blue curve: center value of the main contribution energy region as a function of time. The green and red arrows denote the time window and corresponding energy window.

The neutral yield collection and data analysis in an ESR experiment are generally performed in a limited time range which is usually called a time window. The short time limit (noted as t_1 in the figure) usually corresponds to the time of flight of the molecular ions from the laser excitation zone to the detection zone which is determined by the kinetic energy of the molecular ions, size of the ESR and the

configuration of laser excitation and neutral collection. The long time limit (noted as t_2) is chosen by selecting the number of neutral yield peaks to analyze. Such time window determines an energy window, and the collected neutral yields in the experiments are mainly contributed by and sensitive to the molecular ions with internal energies inside this energy window, but less sensitive to the molecular ions with lower or higher internal energies. In addition, the main contribution energy decreases slower and slower with increasing time, then the low limit of the energy window is not as sensitive as the high limit to the time. Therefore, the energy window is actually mainly determined by the short time limit t_1 in the experiments.

2.3.4 **Neutral Yields and IED**

As a first order assumption, a rectangular function with only two parameters, E_{edge} and $E_{\min}$ are employed to define the high and low energy edges of the IED. For different IEDs with high energy edge varying from 9.0 to 11.0 eV and low energy edge fixed at 8.0 eV (Figure 2.21 (a)), the calculated neutral yields $I(t)$ are plotted in log-log scales in Figure 2.21 (b). When E_{edge} is larger than 10.1 eV, the neutral yield curve is close to the t^{-1} law as discussed above. In this case the IED is broad enough to be considered as infinitely broad. When E_{edge} is smaller than 10.1 eV, the neutral yield at t = 3 μs deviates from the t^{-1} law, and this deviation increases noticeably when E_{edge} decreases.

In fact, the neutral yield at each time follows this rule: when the high energy edge is higher than a critical value, the neutral yield tends to t^{-1} law; otherwise it deviates from t^{-1} law and the deviation increases when the high energy edge decreases. This phenomenon can be explained qualitatively in the following. Due to the fact that the dissociation rate increases strongly with internal energy (Figure 2.5), molecular ions with higher internal energy dissociate faster, the emitting neutral fragments contribute mainly to the neutral yield $I(t)$ at short time range. Thus, the lack of population at high internal energy leads to the deviation of the calculated neutral yield from t^{-1} law. Since the deviation of the neutral yield from t^{-1} law corresponds to the change of the high energy edge E_{edge} of the IED in short time range, it offers the possibility to study the evolution of the high energy edge E_{edge} by analyzing the deviations of the neutral yield from t^{-1} law at different times.

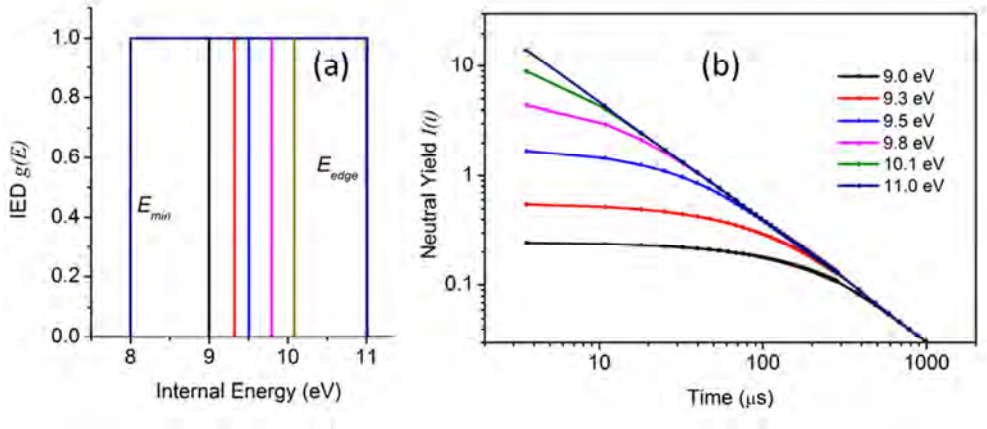

Figure 2.21 (a) IEDs with different high energy edges E_{edge}, (b) Neutral yields $I(t)$ calculated from the IEDs in (a).

Similar calculations are also performed by fixing the high energy edge E_{edge} at 11.0 eV and varying the low energy edge $E_{\min}$, the calculated neutral yields are plotted in Figure 2.22 (b) with their corresponding IEDs in (a). In contrast to the results in Figure 2.21, the neutral yield deviates from t^{-1} law at long time range when the low energy edge $E_{\min}$ is higher than a critical value. This calculation indicates that the deviation of the neutral yield from t^{-1} law at long time range corresponds to the molecular ions with internal energy at around the low energy edge $E_{\min}$. Therefore, by analyzing the deviation of neutral yield at long time range, the low energy edge $E_{\min}$ of the IED may be estimated. However, this is difficult to perform accurately in practice since the neutral yield $I(t)$ decreases fast with time, leading to very low count rate at long time range.

In order to investigate the deviation of the neutral yield from t^{-1} law more precisely, taking the first point of each curve at t = 3 μs in Figure 2.21 (b), the neutral yields $I(E)$ is plotted as a function of the high energy edge E_{edge} (Figure 2.23). It is noticed that the neutral yield $I(E)$ increases fast with the high energy edge E_{edge} in the intermediate energy region between 9.3 and 10.5 eV; while E_{edge} is higher than 10.5 eV or lower than 9.3 eV, the neutral yield $I(E)$ hardly changes. This indicates that there might exists an energy region while E_{edge} is inside this region, the neutral yield $I(E)$ is sensitive to the high energy edge of the IED.

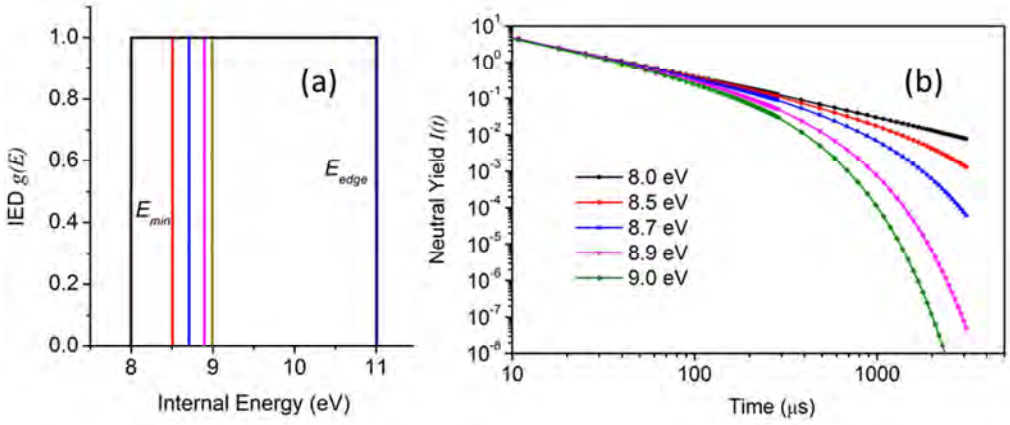

Figure 2.22 (a) IEDs with different low energy edges $E_{\min}$, (b) Neutral yield $I(t)$ calculated as a function of time with the IEDs in (a).

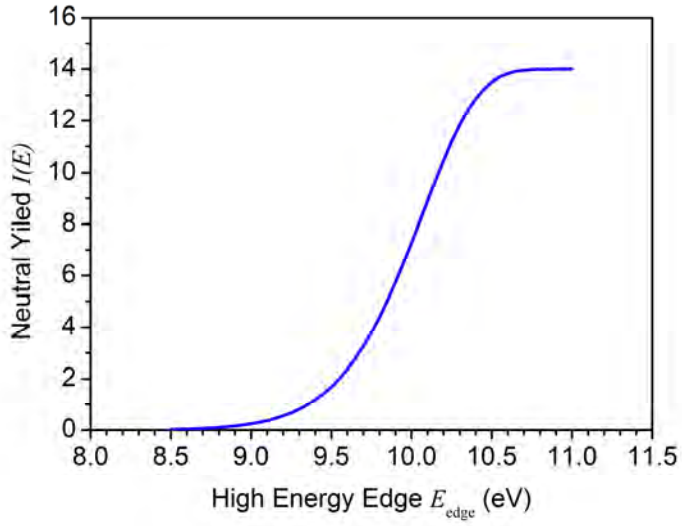

Figure 2.23 Neutral yield $I(E)$ at t = 3 μs as a function of the high energy edge of the IED.

Theoretically, by comparing the experimental neutral yield with the calculated relation between the neutral yield $I(E)$ and the high energy edge E_{edge} (Figure 2.23), one can estimate the IED of the molecular ion ensemble, this leads to a rough determination of the IED.

2.3.5 **Decay Factor α**

The deviation of the neutral yield $I(E)$ from t^{-1} law in Figure 2.21, as discussed above, corresponds to the high energy edge E_{edge} of the IED. In order to describe the

deviation with a phenomenological parameter, a power law function $t^{-\alpha}$ is used to fit the first ten points (from 3 to 62 μs) of the neutral yield curve $I(t)$ in Figure 2.21. The dimensionless factor α is referred hereafter as "the decay factor". Although the $t^{-\alpha}$ law cannot fit precisely the neutral yield curve $I(t)$, the decay factor α is easy to get and still a good indicator for the decay of the neutral yield.

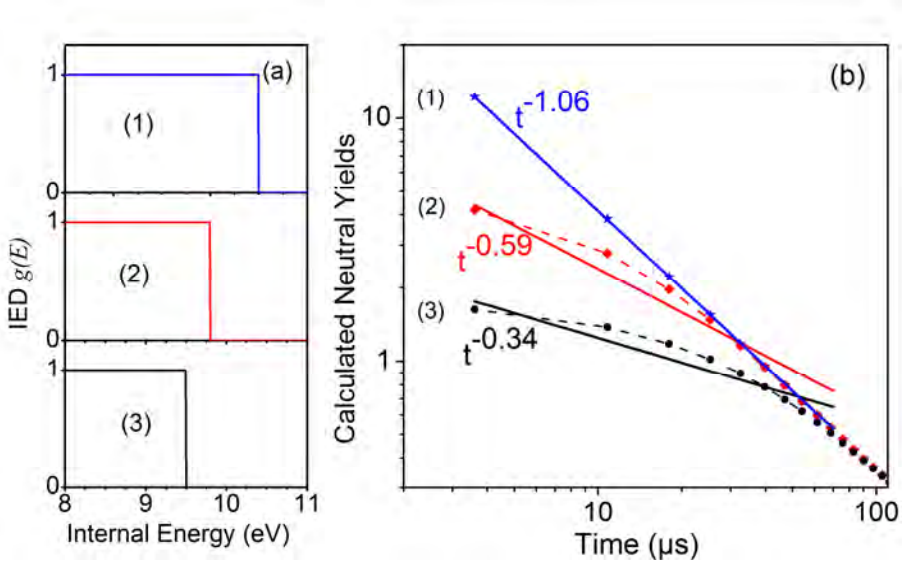

Figure 2.24 (a) Three different IEDs, (1) E_{edge} = 10.5 eV, (2) E_{edge} = 9.8 eV, (3) E_{edge} = 9.5 eV. (b) Symbols: calculated neutral yields from the IEDs of (a), dash lines are to guide the eyes. Straight lines: power law fit $t^{-\alpha}$ for the first ten calculated points, (1) α = 1.06, (2) α = 0.59, (3) α = 0.34.

With the rectangular shaped IED $g(E)$ as assumed above, three different IEDs and the $t^{-\alpha}$ fits of their neutral yields are plotted in Figure 2.24. As mentioned above, when E_{edge} is high enough, the neutral yield $I(t)$ follows the t^{-1} (more exactly $t^{-1.06}$) law; when E_{edge} is lower than 10.1 eV, $I(t)$ deviates from t^{-1} distribution and the deviation is stronger for lower E_{edge} values.

The fitted decay factor α shows sensitive dependency on the high energy edge E_{edge}, it is plotted as a function of E_{edge} from 8.5 eV to 11.0 eV in Figure 2.25. This figure shows three distinct regions similar to Figure 2.23: for E_{edge} > 10.5 eV, the decay factor α is close to 1; for 9.3 < E_{edge} < 10.5 eV, α varies strongly with E_{edge}; for E_{edge} < 9.3 eV, α tends to 0. If the decay factor α in the experiments can be obtained by the same fit, one can determine the E_{edge} of the IED using this relation between α and E_{edge}. However, such a procedure is sensitive only to the intermediate energy

region 9.3 < E_{edge} <10.5 eV where α and E_{edge} presents a nearly linear dependency. It defines in fact an energy window for which the variation of α and E_{edge} is sensitive, this energy window is essentially the same as the energy window we mentioned in subsection 2.3.3. As long as the E_{edge} of the IED is inside this window, any variation of E_{edge} will lead to obvious variation of the decay factor. This energy window is related tightly to the choice of the time range, and extending the time range would increase the width of the energy window at low internal energies.

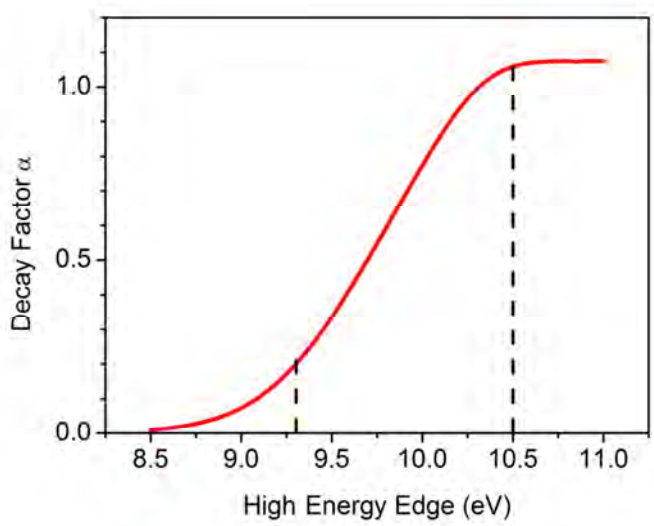

Figure 2.25 Relation between the high energy edge E_{edge} and the decay factor α.

In this section, several calculations on anthracene cation have been performed with several assumptions. The calculations concern the neutral yield, the contribution of neutral yield from molecules with different energies, sensitive energy window as well as the relation between the high energy edge and the decay factor α. Although the exact values given in these calculations rely on the model and the date of anthracene cation, the relations among the neutral yield $I(t)$, the IED (or internal energy) and time can still be discussed qualitatively. These calculations are meaningful and important for not only understanding the ESD experiments but also the design of experiments.

Conclusion

In this chapter, the cooling mechanisms of the studying candidate the anthracene cation in the astrophysical condition, including dissociation, fluorescence emission

and IR emission have been discussed in detail. To study its radiative cooling process and find the experimental evidence of the predicted fast radiative cooling, the photodissociation has been chosen as a probe. The Franck-Condon profile for the photon absorption of anthracene cation has been discussed based on the absorption profile of anthracene molecule. The third harmonic photon (355 nm, 3.5 eV) is considered as a good choice to excite the anthracene cation. Based on the knowledge of the ESD experiments and the data of anthracene, the neutral yield in ESD experiment has been calculated as function of IED and time, respectively. The relations among the neutral yield $I(t)$, IED (or internal energy) and time that we have learned from these calculations are helpful for understanding, as well as the design of the ESD experiments.

Chapter 3 Experimental Setup

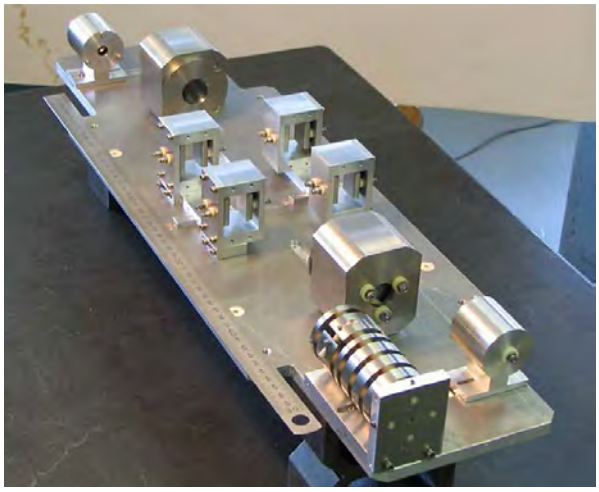

Figure 3.1 First design of Mini-Ring.

To investigate the slow physical processes, for instance the relaxation of PAH molecules, a small electrostatic storage ring was built in Lyon in 2008; due to its small dimensions (Figure 3.1), the ring was named as Mini-Ring [21]. The Mini-Ring was built purposefully with as few electrodes as possible, only ten electrodes plus the ground were used. We have taken the advantage of the ConeTrap; in fact the concept of Mini-Ring's design was based on the ConeTrap. In the Mini-Ring, four pairs of additional parallel-plate deflectors are employed to provide the off-axis (18°) ion injection to the electric field of the conical mirrors, due to the off axis injection, the Mini-Ring contains six straight sections and combines the advantages of both the ESRs and the EIBTs.

In this chapter, a detailed description concerning the construction, simulation and optimization of this new setup will be given individually in three sections. In the first section, the design of each part of the experimental setup, the data acquisition system and the laser equipment will be introduced; in the second section, several simulations concerning the design and storage of Mini-Ring will be performed; in the last section, the optimization process of the ion injection and storage will be introduced, and the storage status of the ion bunch will be discussed.

3.1 Experimental Setup

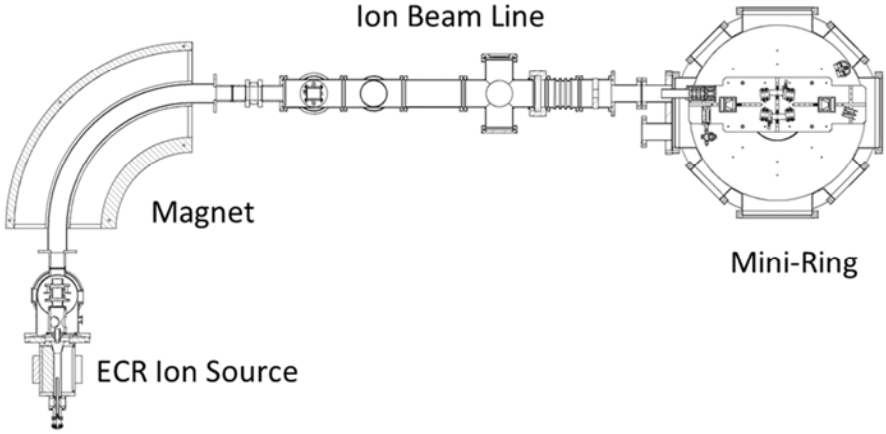

Figure 3.2 Schematic view of the experimental setup.

The schematic of the experimental setup is shown in Figure 3.2, the ions are produced in an electron cyclotron resonance (here after referred as ECR) ion source, selected by the 90° dipole double focusing magnet and bunched in width of typically 1 ~ 2 μs by a pair of vertical parallel-plate deflector called BUNCHER, then the ion bunch is injected and stored in the Mini-Ring. The emitted neutrals due to neutralization and/or unimolecular dissociation of the stored molecular ions are collected on the opposite side of the injection section, and plotted as a function of the storage time after signal processing by the data acquisition system. In order to excite the stored molecular ions and investigate its relaxation process, laser equipment is also employed in our experiments. The whole experimental setup can be roughly considered as five parts: the ion beam preparation, the ion beam line, the Mini-Ring, the data acquisition system, and laser equipment. These five parts will be described individually in the following subsections.

3.1.1 Ion Beam Preparation

3.1.1.1 Ion Source

Depending on the molecular ions one wants to study, there are several kinds of ion sources can be used to provide the molecular ions, like the electrospray ion source [121] [122] [123], Nielsen plasma ion source [124], laser ablation source [125], electron beam ion source [126] [127], Penning ion source [128] [129] and the ECR ion source [130] [131] [132], etc. In this work, a nanogan type ECR ion source from

PANTECHNIK Company was employed to produce the anthracene cations. A brief history and the principle of the ECR ion source are presented hereafter.

The first ECR ion source named MAFIOS was built by R. Geller in Grenoble, France in the middle of the 1960s, then the SUPERMAFIOS and the TRIPLEMAFIOS were established in the same group, the performance concerning the charge sates and intensity of beams has been improved. For this type of ion source, there are several advantages like no electrode corrosion due to arcs, neither cathodes nor anodes in the discharges, etc [130]. Moreover, the ECR ion source benefits from several good properties: stability, easy operation, wide range of species, high ion charge states, high beam current, etc.

The development of the ECR ion source can be roughly divided into three generations according to the resonance frequency. The first generation ECR ion sources operate between 5 and 10 GHz, and the second generation sources operate between 10 and 20 GHz appearing in the late 1980s, which became the most common type of source used for the accelerators, like ECR4 14.5 GHz at GANIL. The third generation ECR ion sources, not like the first and second generations that could be built using conventional room temperature solenoids with permanent magnet sextupoles or with superconducting coils, require fully superconducting magnet structures, like the VENUS ECR ion source which operates at 28 GHz, and the NbTi superconducting wire are used to build the solenoids and sextupoles [133]. The fourth generation, operating with resonance frequency greater than 40 GHz, is under development [134].

The working principle of ECR ion source has been well described in many earlier articles [130] [131] [132]. As illustrated in Figure 3.3, the ECR ion source includes four parts: the plasma tube, the gas feeding system, the microwave system and the minimum-B structure (Figure 10 in Ref. [132]).

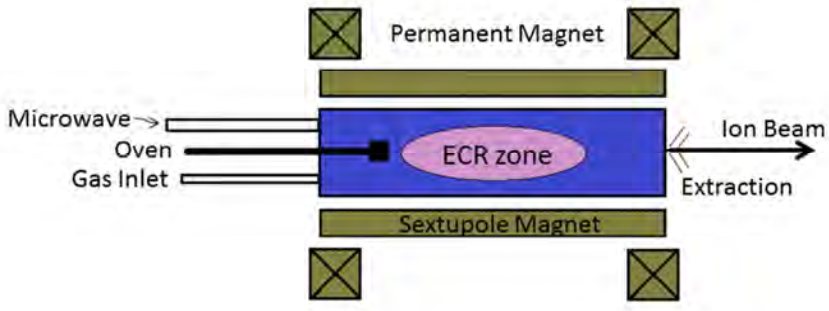

Figure 3.3 Main elements of an ECR ion source.

In general, one set of solenoids are employed to provide an axial mirror field as shown in Figure 3.4 (a) and another set of permanent magnets to produce a radial field

as shown in Figure 3.4 (b) [130]. In the nanogan type ECR ion source, the solenoids are replaced by permanent magnets to reduce the electrical power. The axial and radial magnetic fields together form a minimum-B structure: the magnetic field has a minimum in the middle and from where it increases along all the directions. By this configuration, the electrons are confined due to the magnetic mirror effect; this magnetic field is also called a magnetic bottle. Microwave with a frequency of 10 GHz is sent into the magnetic field at low power (0 ~ 10 W) to accelerate the electrons, thus a closed electron resonance surface can be built at a certain B value. When the electrons move into the magnetic field, they gyrate due to the Lorentz force, and absorb energy from the electromagnetic wave when passing through the resonance surface where the following condition is fulfilled:

$$\omega_{ce} = \frac{eB}{m_e} = \omega_{rf}$$

Equation 3-1

ω_{ce} is the gyration frequency, e the elementary charge, B the magnetic flux density, m_e the mass of electron and ω_{rf} the frequency of the electromagnetic wave.

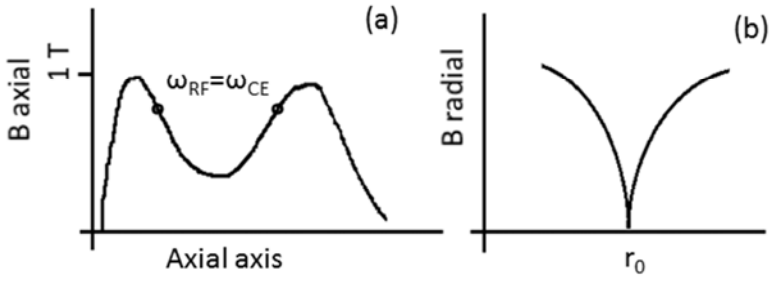

Figure 3.4 Magnetic field of an ECR ion source. (a) axial field; (b) radial field, r_0 stands for the center of the source.

Since the electrons are confined in the magnetic field, they can pass the resonance surface many times and gain kinetic energy to ionize the atoms or molecules to high charge state by successive single ionization, during this process, the electron temperature T_e and the electron density n_e should be as high as possible to increase the collision rate between the electrons and ions.

In the plasma, the ions and electrons are kept in a dynamic equilibrium by ambipolar diffusion that maintains the neutrality. Because of its heavy mass, the ions can neither be confined for long inside the magnetic field nor be accelerated. The average ion confinement time τ_i is linked to the average electron confinement time

τ_e [132]. The beam current of the source is directly related to $n_e\tau_i$, when the electron density and the ion confinement time increase, the beam current increases.

The ECR ion sources are generally known to produce hot plasma to get highly charged ions. However, we operate the nanogan ECR ion source in a special condition with very low power (0 ~ 10 W) to produce much colder plasma in which the anthracene molecules could be singly or doubly ionized without breaking. The anthracene powder we use in this work is from Sigma Aldrich Company with a purity of 99%, the powder is put into the oven on the opposite side of the extraction electrode (Figure 3.3). The heating power of the oven is increased slowly in the experiment until there is enough anthracene vapor in the plasma. The temperature of the oven is estimated to be about 60 °C under which the anthracene molecule will not be broken due to heating.

The ECR ion source can work under continuous or pulsed regime. Since our ion source is connected to a storage ring which does not require continuous ion beam injection, it would be reasonable to let it work at pulsed regime. However, it is not the case in our experiments. Although working at pulsed regime can increase the beam current, it also increases the cost to employ a high-voltage high-current power supply and a fast high-voltage transistor switch to change the extraction voltage (higher than 10 kV) of the source rapidly. On the other hand, it is relatively easy to have enough beam current for the experiments, and the kinetic energy dispersion of the extracted ions is lower if the source works under continuous regime. Thus, the ECR ion source in this work always works under continuous regime.

3.1.1.2 **Mass Spectrum**

In this work, the singly charged anthracene cations are produced in the ECR ion source. To extract the ions, the source itself is placed at a positive high voltage, while the extraction electrode and the downstream beam line components are placed at ground.

After being extracted at 12 kV from the source, all the ions are delivered into the mass selection magnet (radius R = 50 cm) through an Einzel lens. Two parallel-connected high-current power supplies (52 V, 60 A) from DELTA ELEKTRONIKA Company are employed to provide current for the magnet. The current of the two power supplies is controlled by a LabVIEW program via a data acquisition PCI card (NI 6221) with a fairly small step 0.5 mA, so that those species with close mass like anthracene$^+$ and (anthracene-H)$^+$ can be well separated. This LabVIEW program and the PCI card (NI 6221) are also used to record the beam current on the beam line and inside the ring chamber. Thus a mass spectrum can be obtained by recording the ion

beam current on a Faraday cup while scanning the current of the power supplies of the magnet.

Figure 3.5 shows a typical mass spectrum of anthracene cation and its fragments, the Ar gas is injected into the source as support gas to start the plasma. This mass spectrum is very similar to that obtained by other mass spectrometry techniques. The two series of fragments in the spectrum which are plotted as insert figures, show that the main dissociation channels of anthracene cation are the loss of H and C_2H_2. Note that, on the right side of the main peak Ant^+, the small peak corresponding to mass 179 is also anthracene cation but with isotope ^{13}C instead of ^{12}C in the anthracene molecular ions.

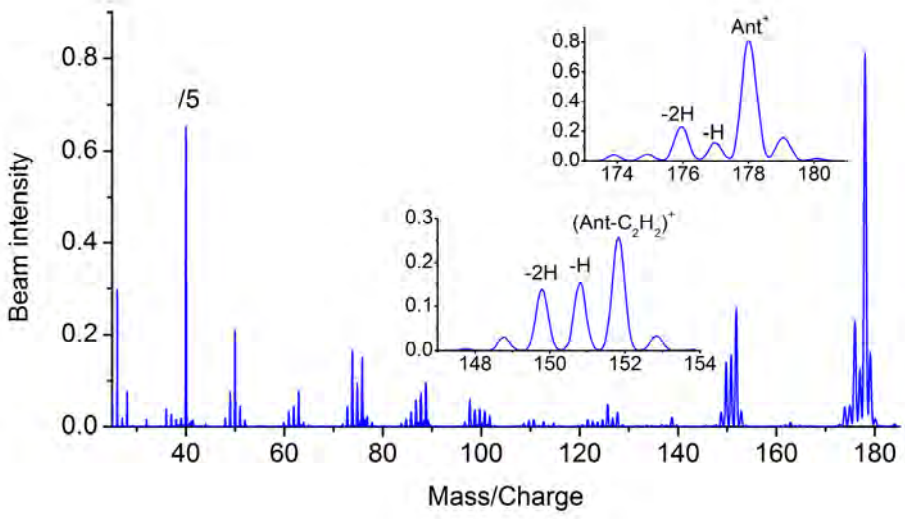

Figure 3.5 Mass spectrum of anthracene cation (noted as Ant^+ in the figure) and its fragments produced in the ECR ion source, the beam intensity of Ar^+ was divided by a factor of 5.

To produce anthracene cation, the ion source may work under different source conditions, i.e., different gas pressures and/or different microwave powers. As shown in Figure 3.6, the pressure in the source is maintained at 3×10^{-7} mbar while the microwave powers are 2 and 0.91 W for the two mass spectra (a) and (b), respectively. In order to compare the relative beam intensity, the intensities of the main product anthracene cation in (a) and (b) are normalized to 1. As noticed, when the microwave power is reduced from 2.0 to 0.91 W, the intensity of $(anthracene\text{-}2H)^+$ peak is strongly reduced, indicating that with different source conditions, the anthracene cations produced in the source may have different internal energy distributions.

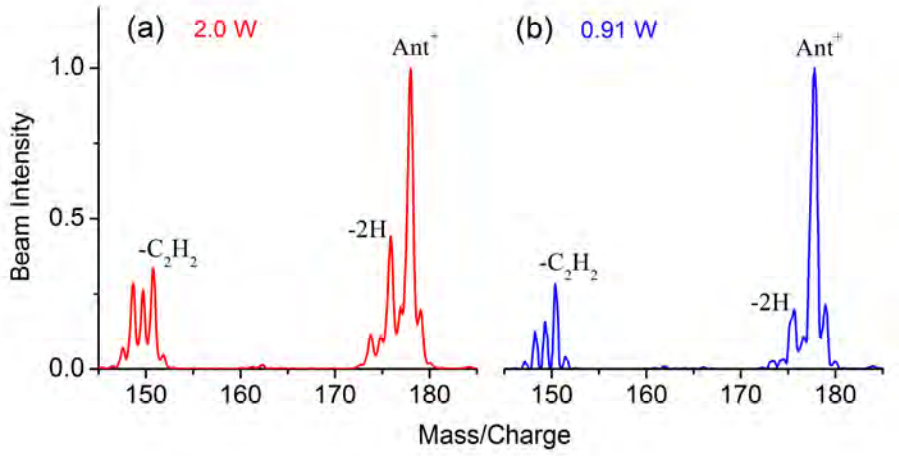

Figure 3.6 Mass spectra of anthracene cation under different microwave powers, the intensities of the main product anthracene cation are normalized to 1.

During the experiments, we prefer to optimize the source condition to maximize the beam intensity of anthracene cation comparing to its fragments. Thus we would like to have the plasma in the source as cold as possible, and the microwave power is always set close to the critical value below which the plasma may stop. To avoid collision between the anthracene cations and the Ar gas in the extraction area, the gas pressure in the source is typically set to ~10^{-7} mbar. Although the plasma in the source is cold, the successive dissociation of anthracene cations (Figure 3.5) indicates that the produced anthracene cations still have broad internal energy distribution.

3.1.2 **Ion Beam Line**

The ion source offers continuous molecular ion beam, but we only store a small bunch of ions during each storage cycle. The ion bunch is produced by the BUNCHER which works for not only producing ion bunch but also inhibiting the injection during the storage cycle. Before the molecular ions being injected into the ring, the number of molecular ions in the ion bunch must be restricted to protect the detector, here a one-dimension slit is used just in front of the ring chamber. The vacuum in the ion beam line is typically ~10^{-8} mbar. In order to obtain better injection and storage conditions, a set of lens and two pairs of steerers, together called injection optics are placed just in front of the ring electrodes. The schematic view of the ion beam line is presented in Figure 3.7, in this subsection, the BUNCHER and injection optics will be discussed respectively.

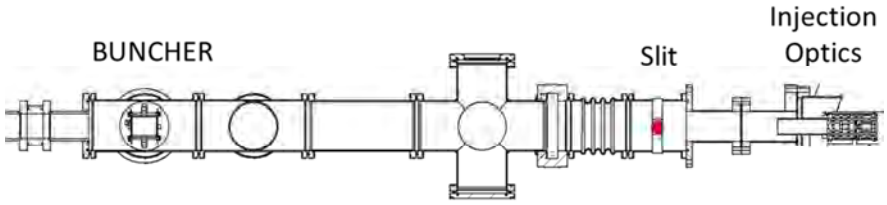

Figure 3.7 Ion beam line.

3.1.2.1 **BUNCHER**

The BUNCHER in the present work is made of two parallel-plate electrodes placed with a distance of 10 mm. When the voltages on the two electrodes are set to 0 V, the ion beam passes through the BUNCHER; when the voltage on one of the electrodes is set to a high enough voltage, typically +130 V while the voltage on the other is still 0 V, the ion beam trajectory can be bent and the injection is inhibited. In order to produce an ion bunch, the voltage on the BUNCHER must be rapidly switched off and then switched on again with a certain delay. To produce an ion bunch in nice square profile with typical width of 1 ~ 2 μs, the rise and fall times of the voltage must be short enough (< 100 ns) to avoid affecting the profile of the ion bunch.

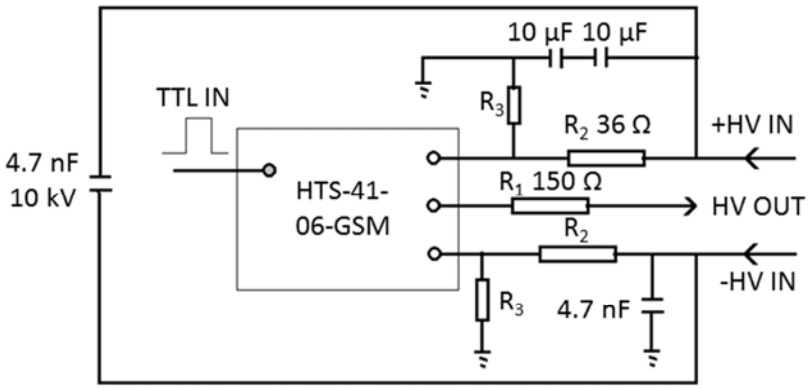

Figure 3.8 Circuit of the fast switch.

A special switch is used to change the voltage on the BUNCHER. The most important component of the switch is an HTS-41-06-GSM module from Belke Company. This is a high-voltage (up to 6 kV), high-current, fast transistor switch. Using this switch, the rise and fall times of the voltage are in tens of ns range, fast enough to accomplish the requirements. As illustrated in Figure 3.8, in order to output a positive high voltage, the –HV IN is connected to ground while the +HV IN is connected to a high-voltage high-current power supply (±2000 V, 60 mA); the HV OUT is connected to the electrode of the BUNCHER. The switch is driven by a TTL

pulse, when 0 V is applied to the TTL IN, the HV OUT outputs a voltage value as that of the +HV IN, which will bend the ion beam trajectory and inhibit the injection; when the positive 5 V is applied to the TTL IN, the HV OUT outputs 0 V, the ion beam then can pass through the BUNCHER. Hence, the width of the TTL pulse determines the width of the ion bunch.

The same transistor switches and circuits are also used to switch on and off the voltages on deflector D_1 of the ring, which will be discussed later.

3.1.2.2 **Injection Optics**

After passing through the vertical slit in front of the chamber, the ion bunch is delivered into the ring chamber and prepared to be injected into the storage orbits. A set of injection optics including a lens and two pairs of steerers, are placed just in front of the ring electrodes to tune the injection angle, injection position of the ion bunch, and to focus the ion bunch. The dimensions of the lens and steerers are shown in Figure 3.9.

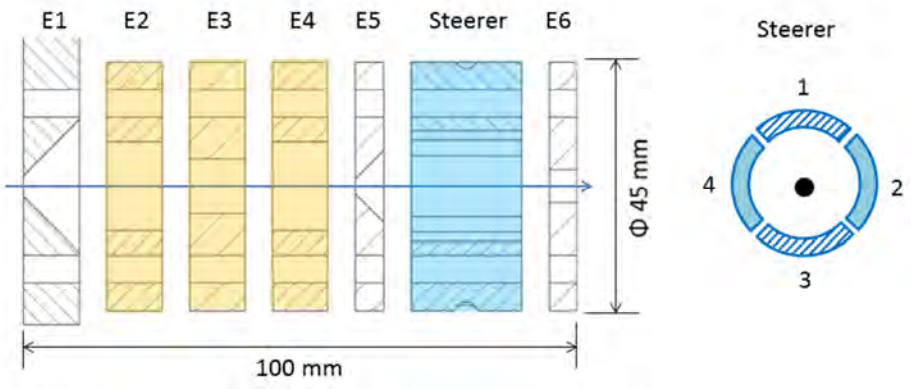

Figure 3.9 The dimensions of the lens and steerers. The electrodes are in cylindrical shape, the steerers are divided into four individual electrodes (right). The steerers are in two groups, in charge of the corrections in horizontal and vertical directions, respectively.

The lens (E2-E4) is used here to focus the ion bunch in both horizontal and vertical directions to get approximately parallel ion beam. The two pairs of steerers are in charge of the corrections of ion injection direction and position in horizontal and vertical direction, respectively. Although the corrections of the steerers are usually small, it is of importance for optimizing the ion injection condition. In addition, several apertures (E1, E5 and E6) are designed along the ion beam line, the smallest one (E5) has a diameter of only 5 mm. These apertures together with the slit in front of the ring chamber are helpful to restrict the ions' trajectories to get better ion emittance.

3.1.3 **Mini-Ring**

The core part of the setup, the Mini-Ring is placed in a high vacuum chamber under the pressure of 2×10^{-9} mbar, under such vacuum condition, the collision of the stored ions and the residual gas is very rare. In this subsection, the Mini-Ring including its electrode design, the diagnostics and detectors will be presented.

3.1.3.1 **Electrode Design**

As introduced at the beginning of this chapter, the Mini-Ring contains only ten electrodes plus the ground. These ten electrodes together with the ground form two kinds of electrostatic elements including four pairs of deflectors D_1 to D_4 and two cones C_1 and C_2. The geometries of the cone and the deflector are illustrated in Figure 3.10.

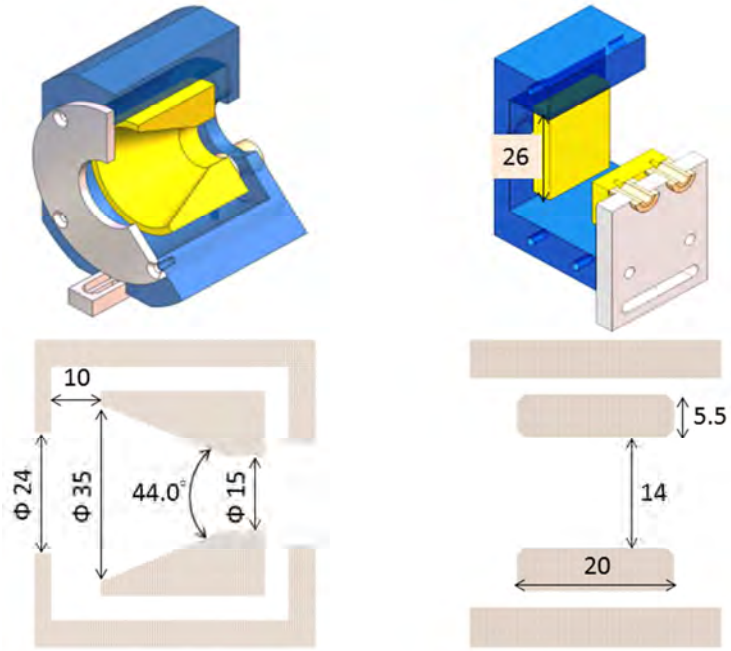

Figure 3.10 The geometries of the cone (left) and the deflector (right), the yellow parts are the electrodes, the gray and blue parts are ground; dimensions are given in mm.

The electrodes in the cone including the grounded ones have cylindrical symmetry. Comparing to the opening angle of 18° in the ConeTrap, the cone used in Mini-Ring has a much larger opening angle 44°. Once a high voltage is applied on the cone electrode (yellow part on the left of Figure 3.10), electrostatic potential surfaces that bends along the inner shape of the cone electrode are created close to the cone electrode, while almost flat potential surfaces are created close to the front grounded electrode. These potential surfaces are very sensitive to the distance (10 mm in the

present cone) between the cone electrode and the front grounded electrode. By such a configuration, the charged particles entering the cone will be reflected just like the light being reflected by an optical spherical mirror, thus the cone is also called electrostatic mirror. Beside reflection effect, the cone also focuses the charged particles; the focusing effect of the cone will be discussed later in paragraph 3.2.1.1.

The deflector is formed by two parallel-plate electrodes, in the present work, positive and negative voltages at the same value are applied to the two parallel-plate electrodes individually, thus the electrostatic potential in the middle of the deflector is close to zero. This design helps to reduce the acceleration and deceleration of charged particles when they pass through the deflector.

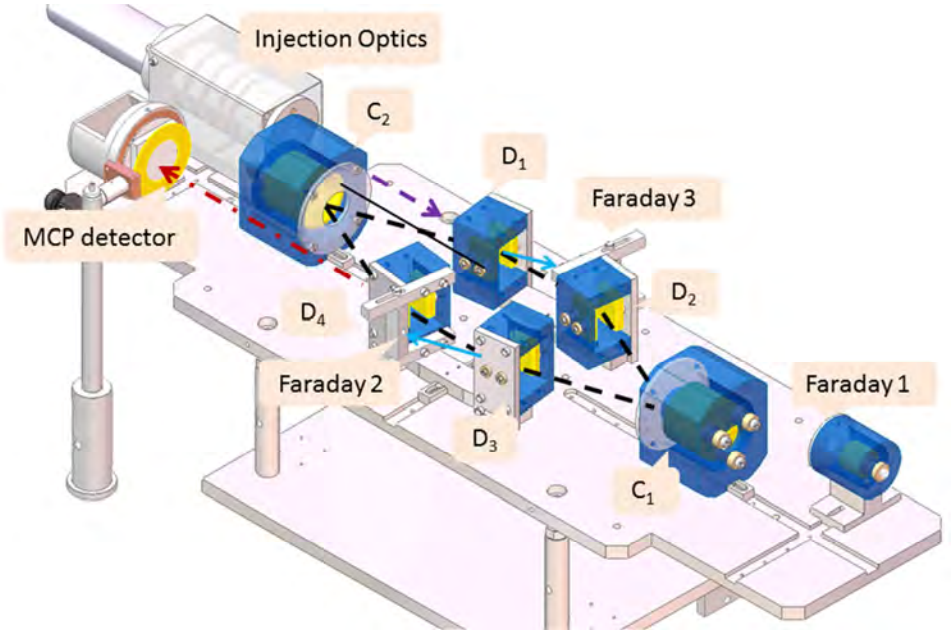

Figure 3.11 The configuration of Mini-Ring. The black dash line stands for the storage orbit, the circumference of which is 0.73 m; the blue dash line with arrow stands for ion injection; the red dash-dot line for emitted neutrals.

Four pairs of deflectors and two cones are placed separately inside grounded shields on a common grounded plate with positioning precision of 0.1 mm, as illustrated in Figure 3.11. Note that the four pairs of deflectors are slightly titled by an angle of 7° from ion injection direction to optimize the ions' trajectories. The deflectors are employed to offer off-axis injection to the cone, for singly charged ions with kinetic energy of 12 keV, positive and negative voltages of about 2 kV are needed on the parallel-plates to obtain incidence angle of 18° in the cone. The cone electrode is set close to 16 kV to reflect the charged particles at the same angle.

Beside the ring electrodes, as shown in Figure 3.11, there are three Faraday cups and one Micro-Channel Plate (MCP) detector located along the ion trajectories.

Faraday 1 with a hole, located downstream of the injection direction is used when no voltage is set on D_1 or D_2; Faraday 2 located after the C_1 and D_3 is used to collect ions reflected by C_1 while no voltage is set on D_3; Faraday 3 located after C_2 and D_1 is used to collect the ions reflected by C_2 when no voltage is set on D_1. The MCP detector dedicated to neutral collection is installed on the downstream of D_3 and D_4 with a distance of 220 mm from D_4. The beam diagnostics and the collection of the neutral will be discussed in the following two paragraphs, respectively.

3.1.3.2 **Ion Beam Diagnostics**

The ion bunch is injected into the ring through the first straight section D_1 and D_2, while voltages are applied on all the ring electrodes (D_2, C_1, D_3, D_4 and C_2) except D_1. Being affected by the electric field of D_2, the ion bunch is deflected on the horizontal plane with an incident angle of 18º towards the cone C_1. With a proper choice of the voltage and dimension, the equipotential surface of C_1 is similar to a spherical optical mirror; the ion bunch is reflected on the horizontal plane with the angle of 18º towards the third deflector D_3. By optimizing the voltages on D_3, the trajectory of the ion bunch can be deflected back parallel to the ion bunch injection direction. That is half turn of the storage process, which can be considered as three steps: deflection (by D_2), reflection (by C_1) and deflection (by D_3). The storage processes of the rest half turn are similar as the first half: the ion bunch is deflected by D_4 with the same angle of 18º towards C_2, and then reflected by C_2 towards D_1, and finally deflected back to the initial injection direction by D_1. Meanwhile at about half turn the voltages on D_1 must be applied before the ion bunch getting close. For long time storage, the ion bunch just repeats the trajectory turn by turn. When one storage cycle is finished, the voltages on D_1 are switched off and the ring then is open again, the ion bunch escapes from the ring and flies towards Faraday 3.

The voltages on D_1 are also controlled by two fast-switches as that used for the BUNCHER. The way to control the positive voltage has been explained already. In order to control the negative voltage, the –HV IN is connected to the power supply while the +HV IN is connected to ground, and the HV OUT is connected to the parallel-plate electrode. The two fast-switches for D_1 are driven by the same TTL pulse to change the positive and negative voltages on the two parallel-plate electrodes respectively and synchronously. Similar to the BUNCHER, the duration of the driven TTL pulse corresponds to the storage cycle of the ion bunch. The only difference is that the voltages on deflector D_1 are about ±2 kV, higher than that on the BUNCHER.

In order to give some realistic values in the following, let's take anthracene cation with kinetic energy of 12 keV as an example, the revolution period of which inside Mini-Ring is about 6.5 μs. To reduce the influence to the ions' trajectories, the

voltages on D_1 are switched on when the ion bunch is far away from D_1, usually between C_1 and D_3. In the experiments, the ion bunch production time, i.e., the time to switch the voltage on the BUNCHER is used as time reference. Then the D_1 switch time must be carefully controlled with a delay from the TTL pulse used to drive the BUNCHER, as shown in Figure 3.12. This delay called Storage Delay corresponds to the time of flight of the ion bunch from the BUNCHER to D_3. On the other hand, the rising times of the voltages on D_1 are much shorter than half of the revolution period 3.2 μs; after 3.2 μs when the ion bunch arrives in the electric field of D_1, the voltages on D_1 are already stable. The voltage ripple on D_1 is estimated to be better than 0.5%.

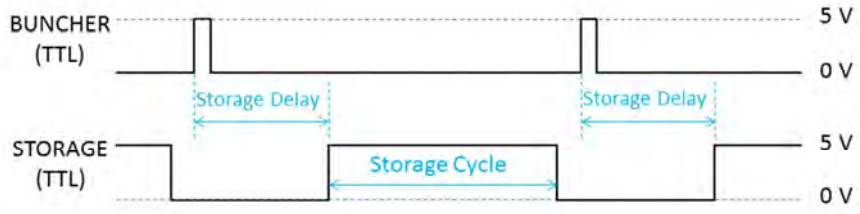

Figure 3.12 Timing chart of the Storage Delay.

3.1.3.3 **Detectors**

The hot molecular cations may dissociate spontaneously by emitting small fragments along the tangent line of their trajectories. In Mini-Ring, the neutral fragments emitted through D_3 and D_4 at each turn will be collected by the detector on the downstream of D_3 and D_4. At the beginning of this work, a channeltron with surface of 5*10 mm^2 was used, now it is replaced by a two-dimension MCP detector in order to improve the collection efficiency, and to get the position information of neutral fragments as well. The daughter ions, having less kinetic energy due to the loss of mass after dissociation process will escape from the ring after several turns.

The MCP detector used in our experiments is a Position Computer (Model 2401) from the Quantar Technology INC (Surface Science Laboratories, INC), Santa Cruz, California, US. It consists of two micro-channel plates, a resistive anode, signal amplifiers and a position analyzer. The two micro-channel plates (25 mm in diameter) are used as electron multipliers to convert each incoming particle to a pulse of charge. The charge pulse is guided by the electric potential until it arrives at the resistive anode. This charge pulse is then divided among the four corners of the resistive anode depending on the incidence position. The signals from the four corners are amplified and shaped by the pre-amplifiers and amplifiers, then sent to the position analyzer. The position analyzer delivers two analog signals with amplitudes proportional to the X and Y position respectively. The two analog signals will be converted to digital signals by analog-digital convertor, and then the incident position of the particle can

be obtained. The dead time of the analog system is about 3 µs, which gives the limit of the maximum output rate ~10^5 per second.

For each incoming particle, once the position signals are valid, a TTL pulse of 2 µs in width is generated, which is used as the time signal of the detected particle in the experiments. Obviously, there is a delay from the real arrival time of the particle to the generation of the TTL pulse, but this delay is identical for each particle. Since the time to produce the ion bunch is used as time reference for all neutral events, the time measurements, here being relative measurements, will not be affected by the identical time delay.

The detection efficiency of the MCP detector for the neutral particles has been studied in the kinetic energy range from eV to several keV [135] [136] [137]. From the earlier works, the detection efficiency of the neutral fragment C_2H_2 (kinetic energy 1.75 keV) has been estimated to be about 40%, and H (kinetic energy 67 eV) less than 1%. On the other hand, the branching ratio of the two fragments C_2H_2 and H is comparable. Therefore, the time signals processed by the detector are predominantly contributed by the fragment C_2H_2, while the fragment H is hardly detected.

In addition, there are four Edge Gating Controls: +Y, -Y, +X and –X in the position analyzer, which allow us to select the desired part of the image and erase the rest part, which can help to select the main product C_2H_2 and reduce the noise counts in the experiments.

Note that, there are six straight sections in Mini-Ring which offer six possible positions to install the detectors. Beside the present position of the detector and a reserved section for laser irradiation, there are still four possible positions. Recently, a new channeltron detector with a surface of 1 cm^2 was installed on the downstream of D_2 and C_1 to collect neutral fragments in shorter time after laser irradiation. This new channeltron detector isn't used in this thesis work, thus it is not illustrated in the configuration of Mini-Ring.

3.1.4 **Laser Pulse Equipment**

The anthracene cations extracted at 12 kV from the ion source are injected into the ring after a time of flight of about 30 µs, and then stored in Mini-Ring with a revolution period of 6.5 µs. To probe the internal energy distribution of the stored ions, it is essential to study the neutral yields from the very first microseconds. Thus the re-excitation of the stored molecular ions during the storage cycle becomes important. In this work, a tunable Nd:YAG laser equipment NT242 from EKSPLA Company is employed to excite the stored molecular ions.

The laser equipment consists of the pump laser NL220, harmonics generators (SHG, THG), optical parametric oscillator (OPO) and sum frequency generation (SFG) combined in a single device, as illustrated in Figure 3.13. The laser equipment works at a constant temperature 24.8 ºC which is fulfilled by a stand-alone chiller.

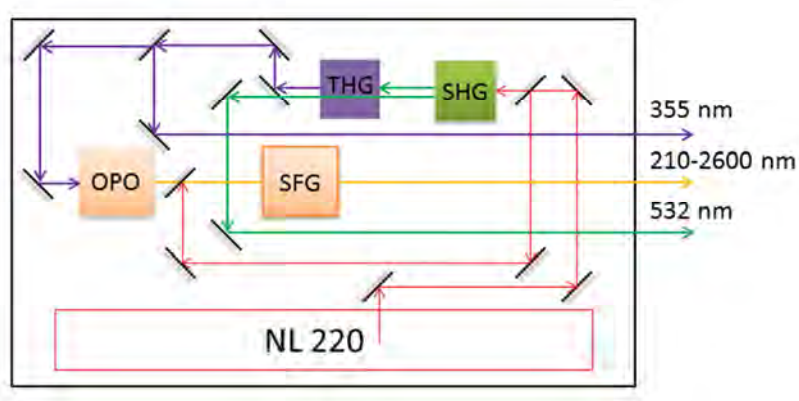

Figure 3.13 Schematic view of the laser pulse system.

As we can see from the figure, there are three outputs which offer laser pulses with second harmonic photons (532 nm), photons with variable wavelength from 210 nm up to 2600 nm and third harmonic photons (355 nm), more details concerning the laser path and the mirrors can be found in the User's Manual. The pulse duration is about 6 ± 1 ns, the maximum pulse energies are about 2.7 mJ at 355 nm and 1.8 mJ at 532 nm, the pulse energy from OPO varies with wavelength, as shown in Figure 3.14.

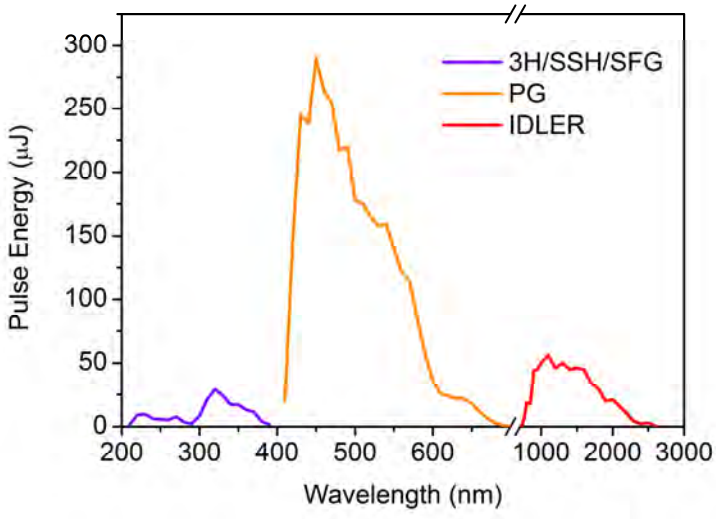

Figure 3.14 Output pulse energy of laser equipment.

The pulse energy is of importance to estimate the number of molecular ions being excited during the laser irradiation. At a given wavelength, the output pulse energy can

be reduced by changing the Q-switch delay, as shown in Figure 3.15, the output pulse energy has been measured by a power meter at 532 and 355 nm as a function of Q-switch delay time. The maximum pulse energy is at Q-switch delay time 196 μs, and the pulse energy decreases with the increase of the Q-switch delay. The Q-switch delay is usually set at 300 μs before and after experiments for safety.

Another important feature of this laser equipment is its high repetition rate of 1 kHz. This maximum repetition rate can be divided by Q-switch divider 1, 2, 3 … thus we can obtain the repetition rates: 1000, 500, 333 Hz … Due to such high repetition rate, the stored ion bunch can be irradiated several times during one storage cycle. During the operation of the laser equipment, synchronized TTL pulses following the chosen repetition rate are produced. Since we cannot choose the laser pulse shooting time, the synchronized TTL pulse is used to trigger both of the control and data acquisition systems.

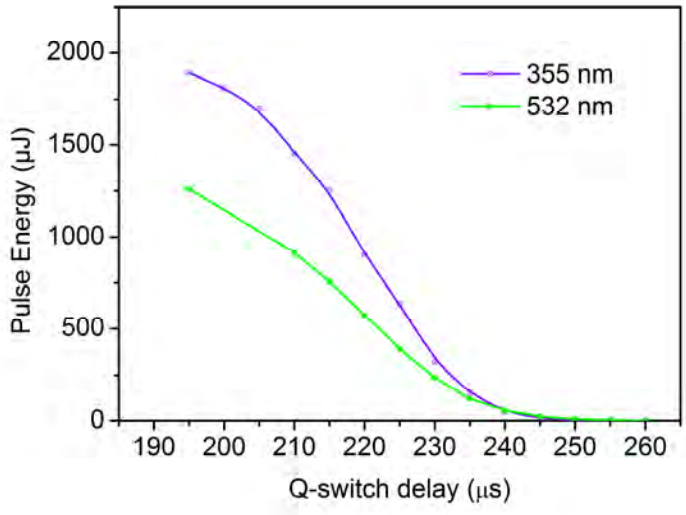

Figure 3.15 Pulse energy as a function of Q-switch delay time.

Figure 3.16 (a) illustrates the schematic of the laser beam path between the laser outputs and the Mini-Ring, (b) is a photograph of the laser path, laser equipment and the ring chamber taken with photon wavelength 532 nm. The laser pulse from the equipment is sent into the ring through D_2 and D_1 via several mirrors. Among these mirrors, the mirrors M-2 and M-X_2 can be flipped to be along the laser path or not while the other mirrors are always on the laser path. For example if one needs photons with wavelength 532 nm, the mirrors M-2 should be flipped along the laser path while M-X_2 not; if one wants to use OPO, both M-2 and M-X_2 should not be flipped along the laser path; if photons with wavelength 355 nm are required, all the mirrors can be flipped along the laser path, but some of them are not used, like M-1, M-2 and M-X_1.

The diameter of the laser pulse is estimated to be about 2.5 mm near the ring chamber, which can be restricted again by the two irises in front of the ring chamber. Considering the depletion of the transmission efficiency of the mirrors, we should use as few mirrors as possible while the injection of the laser pulse can still be finely adjusted. To this purpose, the three mirrors M-X_1, M-X_2 and M-Y are set on translation stages in order to tune accurately the injection of laser beam. Following the coordinate axes in Figure 3.16 (a), the injection X position of the laser pulse is controlled by the mirrors M-X_1 or M-X_2 depending on the wavelength we choose; the injection Y position is controlled by the mirror M-Y while the injection direction can be optimized by the mirror M-Angle. All the mirrors work independently, when we optimize one of them, only the attribution (X position, Y position or injection direction) under its control will change without affecting the other two; so that we can control the laser path precisely to overlap the ion bunch between D_1 and D_2. The detailed overlap condition will be discussed in the paragraph 4.1.2.2 in the next chapter.

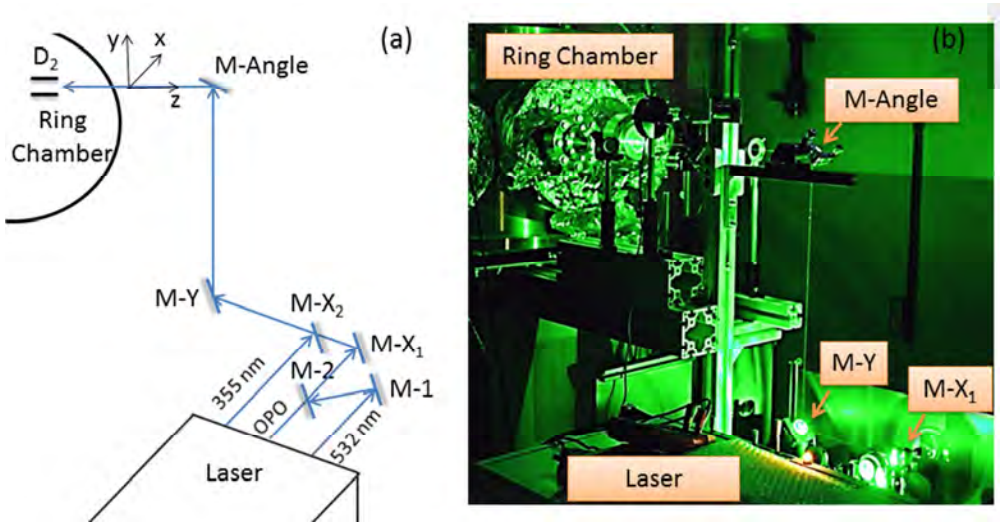

Figure 3.16 (a) Schematic view of the laser path; (b) Photograph of laser path taken with photon wavelength 532 nm.

Although the transmission efficiency of the mirror is wavelength dependent, three mirrors (M-X_1, M-Y and M-Angle) on the laser path are still used for various wavelengths. The total transmission efficiency of the entire laser path is measured to be about 80 % at both 532 and 355 nm.

3.1.5 **Data Acquisition System**

The MCP detector produces a TTL pulse in width of 2 µs each time when the X, Y position signals are available. The channeltron provides only fast time signal. These time and/or position signals will be processed by the subsequent data acquisition

system. Two acquisition systems, the CAMAC controlled by a Kmax program and a National Instruments PCI card controlled by a LabVIEW program are employed in this thesis work. In this subsection, the two acquisition systems will be briefly introduced.

3.1.5.1 **CAMAC Acquisition System**

The CAMAC acquisition system is developed for the MCP detector which provides both time and position signals, it can also be used for the channeltron detector from which only time signal is provided. To build up the CAMAC acquisition system, the following package boards are employed: one time to digital convertor TDC 4208 (full time range 8 ms, resolution 1 ns), one SCALER, one analog to digital convertor AD811 ORTEC (8 channels, 11 bits) to convert the position signals, and a list processor HYTEC LP1342. This processor is able to read various data (X and Y position, time, stop number, etc.) from each storage cycle up to 1 kHz.

The time signal from the position analyzer is converted to TTL or NIM type and delivered individually to five channels, as shown in Figure 3.17. The first channel ①SCALER counts the total number of events occurred during one storage cycle. The second channel is the Time on the TDC 4208 which is a multi-hit TDC with maximum eight stops. In another word, this TDC can record up to eight events during 8 ms. The third channel is the COUNT RATE on a rate meter in a NIM crate, which gives the count per second directly. The fourth channel is the STROBE on the mono-hit AD811, the STROBE signal here provides the trigger for AD811 to start to convert the position signals to digital data. The fifth channel is also used as a trigger, with a proper delay (the dead time for the AD811 to process the position signals for one event, ~100 μs) to trigger the list processor HYTEC LP1342 to read the data from AD811 and empty it for the next event.

The X, Y position signals are sent to channel 7 and 6 of the AD811 with the ④STROBE as a trigger, the position information of the neutral particles then can be calculated. In order to obtain the coincidence between the position information and the time information, a sawtooth-shaped RAMP pulse produced by a function generator is sent to the channel 5 of AD811 with voltage 0 V as time zero to estimate the event time. The precision of this time measurement is limited by the quality of the sawtooth-shaped RAMP pulse. However, a more precise time measurement is obtained from TDC. The detailed timing chart of the acquisition and the control systems is illustrated in Figure 3.18.

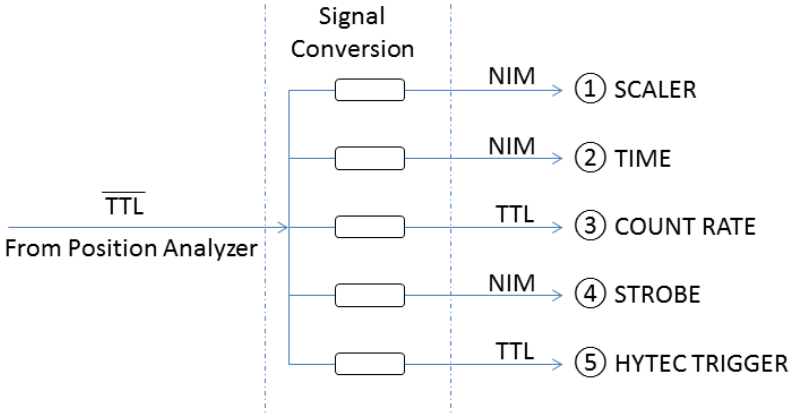

Figure 3.17 Processing of time signal in the data acquisition system, NIM and TTL stand for the signal type.

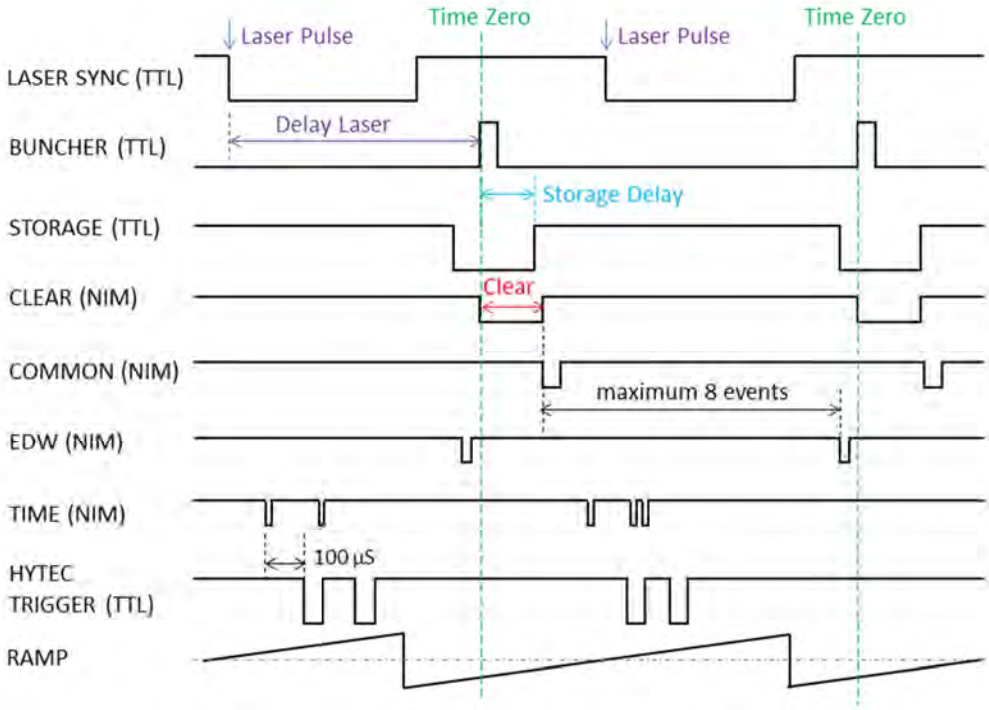

Figure 3.18 Timing chart of the acquisition and control systems.

The LASER SYNC pulse is used as a trigger to activate the control and acquisition systems with a delay called Delay Laser. Once the control system is activated, the BUNCHER starts to produce an ion bunch; the time to produce the ion bunch is used as time reference in the later acquisition and control systems for each storage cycle. The STORAGE, CLEAR and EDW pulses are produced with different delays and widths from this time zero. The Storage Delay is the delay to start the STORAGE, as mentioned in paragraph 3.1.3.2, it corresponds to the time of flight of the ion bunch from BUNCHER to D_3. The CLEAR pulse is sent to the TDC to clear

the data buffer. The COMMON pulse synchronized with the end of the CLEAR pulse provides the time reference for TDC. The TDC is limited to a maximum time range of 8 ms and a maximum number of stops, 8 stops; in order to the full advantage of the TDC, the CLEAR pulse can erase the events at the beginning of the storage and shift the acquisition time range 8 ms to longer storage time as well. The EDW pulse ends the signal processing on the TDC and triggers the list processor HYTEC LP1342 to read all the event records on the TDC.

The COUNTS and HYTEC TRIGGER are drawn here to show the difference between the TDC and AD811. The time resolution for TDC is 1 ns but for AD811 with TRIGGER is about 100 μs, if there are two events close to each other (less than 100 μs), we can record both of them on the TDC, but only the first one on the AD811.

All the event records from the TDC and AD811 are read by the list processor HYTEC LP1342 after or during the storage cycle; here we don't give the detail about the command sequence of the list processor. Finally the event records are sent to the computer to display the time and position information of the detected events, the software interface based on Kmax is shown in Figure 3.19. As we can see, there are six main display regions: A, B, C, D, E and F. The time information processed by the TDC is displayed in A with scale of 129 ns per channel. The coincidence time information and position information obtained from the AD811 are displayed separately in B and C. Once a certain time range is selected in region B, the corresponding position information will be displayed in D. By varying the selected time range in region B, the evolution of position information of the detected neutrals can be obtained. The region E displays the number of events recorded by TDC and F displays the total number of events during each storage cycle.

If the neutral events distributed homogeneously during one storage cycle and the TDC records less than eight events, then the AD811 is considered to be fast enough to record all of them. In another word, all the events can be recorded by both TDC and AD811. But the assumption doesn't work for the laser induced events which usually distribute concentratively just after laser irradiation, then the AD811 may miss some events. Since the AD811 is in charge of recording the positions of the neutral events, the missing of a few events will not strongly affect the image of the detected neutrals. In the experiments, the opening of the slit in front of the ring chamber is controlled to limit the number of ions ($\sim 10^3$) in each ion bunch, and therefore to limit the number of events recorded during each storage cycle to be lower than eight.

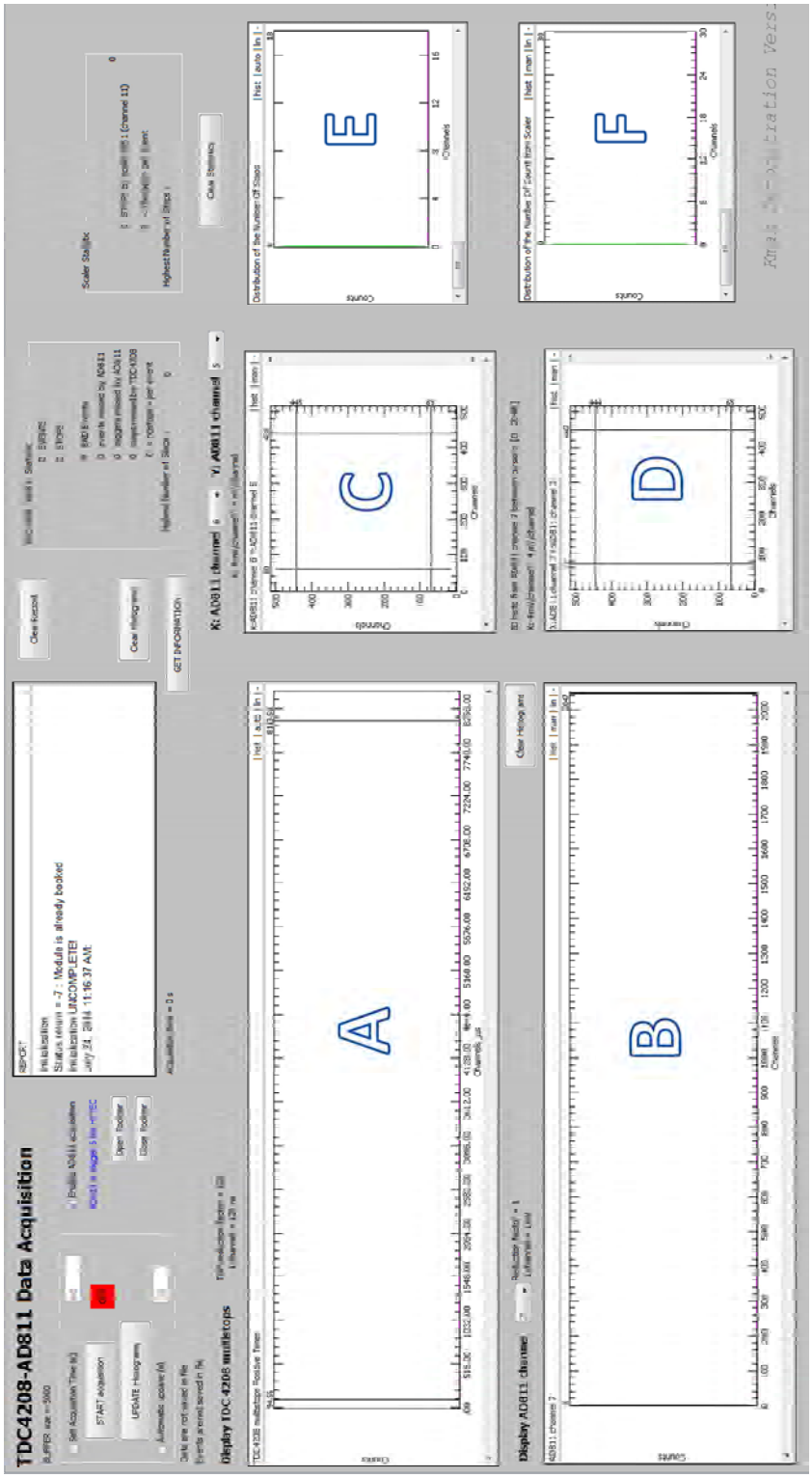

Figure 3.19 The interface of the CAMAC data acquisition.

In conclusion, the CAMAC acquisition system offers high time resolution while displaying the position of the neutral event. There are still three limits for this

acquisition system: the limit count rate of the MCP detector, as discussed above ~10^5; the limit eight stops during one storage cycle, and the limit 8 ms in the acquisition time range. These three limits have more or less consequences in the experiments and in data analysis.

3.1.5.2 **LabVIEW Acquisition System**

The LabVIEW acquisition system is developed using a National Instrument data acquisition PCI card (NI 6602) to record time signal instead of using TDC. Comparing to the CAMAC TDC, the time resolution 0.4 μs is much poorer. The main advantage of this acquisition system is that there is no limit for stops or for time range. Therefore, for long storage time experiment like lifetime measurement due to collision with residual gas, the LabVIEW acquisition system brings convenience to record neutral yields up to second.

The two acquisition systems now work in parallel. By processing the time signals provided by the channeltron detector on the downstream of D_2 and C_1 with LabVIEW acquisition system, the neutral yields recorded by the two systems can be compared and additional information may be obtained. However, this is out of the frame of the present work, will not be discussed here.

In this section, a detailed description of the experimental setup together with laser equipment and data acquisition system have been given, the technical design and basic parameters of each part of Mini-Ring have also been presented and discussed.

3.2 Simulations of Mini-Ring

A virtual “Mini-Ring” which shares the same dimensions as the real one operating in our laboratory has been drawn in SIMION 8.0.4 software. Simulations concerning the design of each electrode and the stable storage condition were started in 2005 during the conception phase of Mini-Ring [21]. The main improvement in this work is that all the electrodes are redrawn in 3D in one large potential array (PA) as shown in Figure 3.20. Note that the coordinate origin (0, 0, 0) locates in the center of the left-down corner of the PA, and the ion trajectory in the figure is at x-y plane where z =0. In this section, first, the optical properties of the two kinds of elements: the cone and the deflector will be simulated again individually. Then the simulations on the stable storage region, the acceptance of ion beam emittance in the ring, the betatron

oscillations on y-axis and z-axis will be performed. In addition, for the first time, the signal collection of the MCP detector will be simulated.

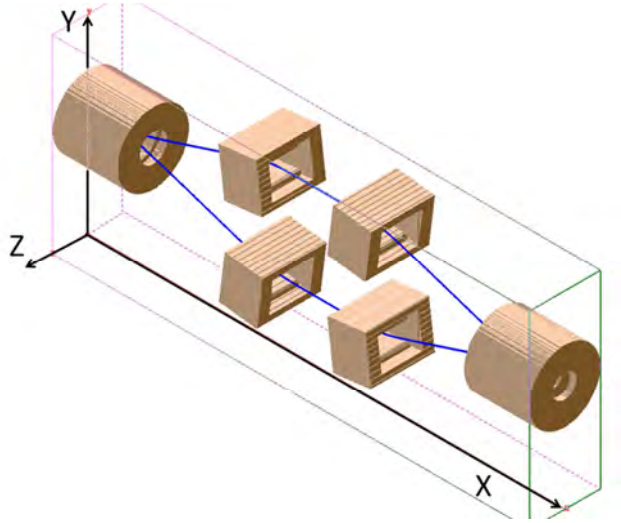

Figure 3.20 The coordinates of Mini-Ring in the simulation of this section, the blue line stands for the ion trajectories.

Considering the computing time limit, the choice of suitable variables is of importance for the simulation, for instance the grid size for drawing electrodes (0.5 mm/gu), the number of ions in random repetition (5000 ~ 50000), the trajectory quality (103), and the upper storage time limit (10 ms), etc. Using the values in the brackets, it usually takes tens of hours to perform one simulation issue. The values used in this work may not correspond exactly to the experimental ones, but they indeed help to show the operation of Mini-Ring.

3.2.1 **Cone and Deflector**

The mechanical design of Mini-Ring has already been shown in Figure 3.10, the two kinds of ion optical elements, the cone and the deflector are the core part of the entire setup. In this subsection, the optical properties of these two elements will be described separately by simulation.

3.2.1.1 **Cone**

Although the optical properties of the conical electrostatic mirror have already been described in the earlier works on the ConeTrap [28], the present cones in Mini-Ring have much larger opening angle (44.0° comparing to 18°). The large opening angle of the cone plays an important role in increasing the acceptance for off axis ion trajectories, thus it is still worthy to study their optical properties.

The simulations of the ion trajectory had been performed to optimize the design of the conical mirrors and their shields several years ago [21]. In this work, we perform the simulation with all the electrodes drawn in 3D. Following the discussion in the subsection 1.2.1 of chapter 1, the following condition must be fulfilled to obtain stable storage orbits,

$$L_x / 4 \leq f_m < \infty$$

Equation 3-2

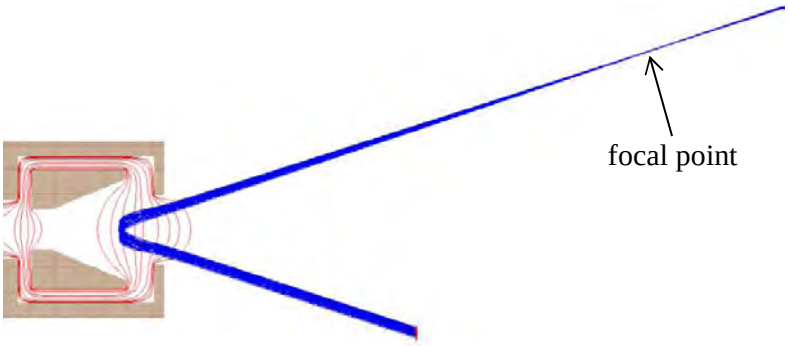

Figure 3.21 Ion optical simulation of a single conical mirror, the focal point is shown for ξ_m =1.35, the equipotential curves are in red.

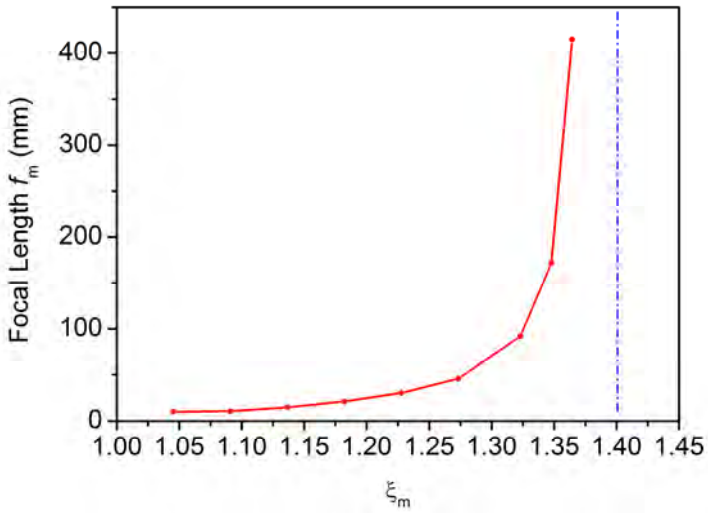

Figure 3.22 Ion optical simulations of the focal length as a function of ξ_m, the blue dash dot line indicates the upper limit of ξ_m for stable ion trajectory.

Hereby, for a single conical mirror, a dimensionless parameter $\xi_m = qV_m / E_k$ is defined where q is the charge of the ion, V_m is the voltage on the mirror electrode, and

E_k is the kinetic energy of the ion. The focal point of the cone is shown in Figure 3.21 in the case of ξ_m =1.35, the injection angle is about 18º as the real case in the experiments. The focal distance of the mirror f_m varies as a function of ξ_m, as shown in Figure 3.22, a strong increase occurs close to ξ_m =1.4, when ξ_m >1.4, the mirror starts to defocus the ions, so ξ_m =1.4 is the upper limit for the cone.

3.2.1.2 **Deflector**

As described in the subsection 3.1.3, the deflectors are used to offer off-axis injection to the cones, and deflection of ion trajectories back to the injection direction. The rectangular shields of the deflectors are placed at ground potential, which are important to build the electric fields. In order to obtain stable storage, similar condition as that for the cone must be fulfilled,

$$\frac{L_y}{4} \le f_D < \infty$$

Equation 3-3

where f_D stands for the focal distance on the horizontal plane, and L_y =80 mm for the distance between the deflector sections D_1, D_2 and D_3, D_4. To describe the optical property, a second dimensionless parameter $\xi_D = \frac{q(V_{D+} - V_{D-})}{2E_k}$ is defined, where V_{D+}, V_{D-} stand for the voltages applied on the positive and negative parallel-plate electrodes. The deflection angle of the deflector increases with ξ_D, Figure 3.23 (a) shows the focal point of the deflector in horizontal plane while ξ_D=0.16, the deflector and its shield are also titled by an angle of 7º as that in the real case. It is noteworthy that the deflector with its grounded shield can focus not only in horizontal plane, but also in vertical direction, although the focusing effect in vertical direction is weak, as shown in Figure 3.23 (b), the focal length is about 1 m with ξ_D = 0.16.

The horizontal focal length f_D of the deflector varies with ξ_D, as shown in Figure 3.24. The deflection angle which increases linearly with ξ_D is also shown on the top of the figure. Since the vertical focusing effect is weak, it is not shown here.

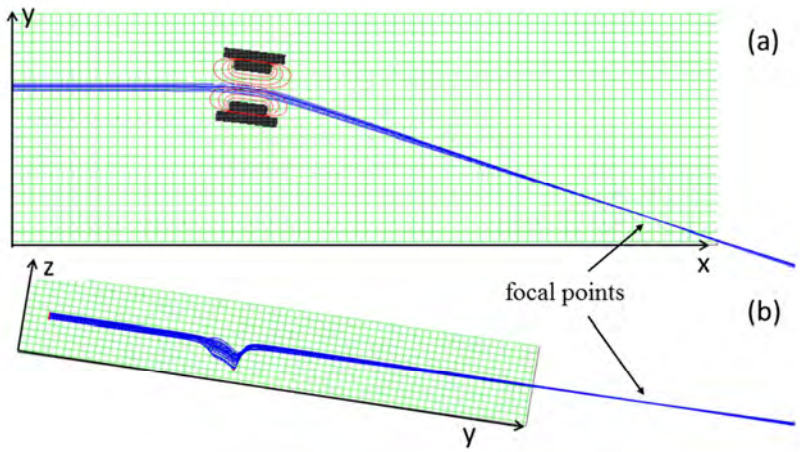

Figure 3.23 Focal points of the deflector in (a) horizontal plane and (b) vertical direction. The equipotential curves are shown in red.

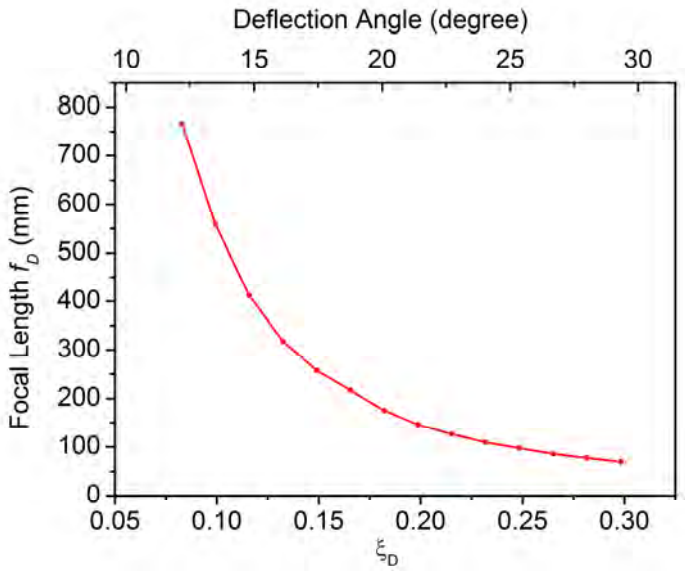

Figure 3.24 Horizontal focal length of the deflector varies with ξ_D, the top axis shows the deflection angle in degree.

As mentioned above, for such a deflector with grounded shield, the main focusing effect is in horizontal plane while the focusing effect in vertical direction is weak. The cone, with its symmetrical shape, focuses the ion bunch in both horizontal and vertical directions. As a result, the net focusing effects of the Mini-Ring in horizontal plane and in the perpendicular direction are not the same. Nevertheless, with suitable geometries for the cones and the deflectors, the focusing condition can be fulfilled in both vertical and horizontal directions for the entire ion optical system. In addition, the geometry of the ring is not unique, i.e. the focusing condition can be fulfilled with different geometries.

In the current geometry, as shown in Figure 3.25, the distance between the two mirrors in Mini-Ring is chosen as 294 mm, and the centers of the four deflectors are placed at distances of 40 mm off the center axis of the cones, D_1, D_2 and D_3, D_4 are in opposite sides, the distance between D_1 and D_2 (D_3 and D_4) is 92 mm. With this geometry, the deflection angle for stable storage is close to 18º, and the entrance angles for D_2 and D_4 are 0º while for D_3 and D_1 are 18º. Considering the deflection angles and entrance angles, the four pairs of deflectors are slightly titled with approximately half of the deflection angle, 7º to optimize the ion trajectories.

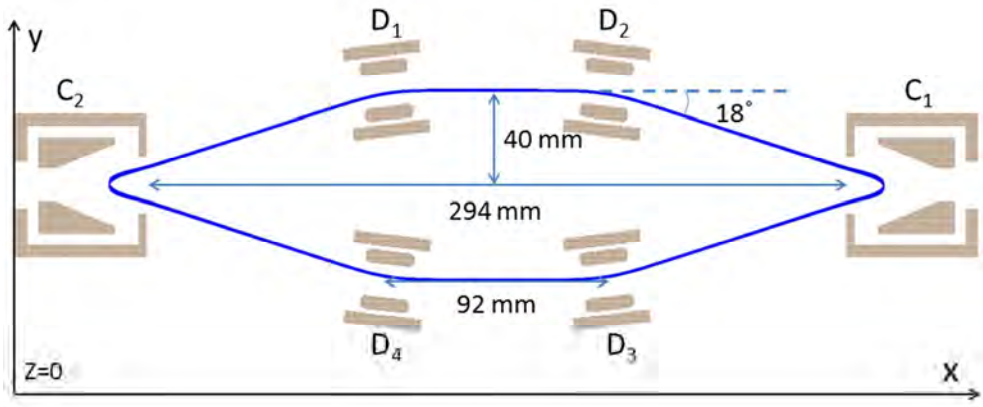

Figure 3.25 Geometry of Mini-Ring at horizontal plane z = 0, the blue curve stands for ion trajectory.

3.2.2 **Storage Condition**

The basic optical properties of the electrodes used in Mini-Ring have been described in the above subsection; further simulations are still needed to characterize the Mini-Ring design. As shown in Figure 3.20 and Figure 3.25, the ion trajectory was simulated for 12 keV anthracene cation launched at the center between D_1 and D_2, the voltages on the cones and deflectors were set to V_m =16035 V and V_D =1926 V, respectively. The center between D_1 and D_2, coordinates noted as (x_c, y_c, z_c) = (202.5, 130, 0) mm in the PA is the location around where the ions are usually launched. In order to know the sensitivity of the storage to the voltages V_m and V_D, the simulations on the stable storage region in (ξ_D, ξ_m) coordinates will be performed, the acceptance of ion emittance and the betatron oscillation of the ions will also be simulated in this subsection.

3.2.2.1 **Stable Storage Region**

As discussed above, we need to determine the sensitivity of the storage to the voltages on the cones and deflectors, i.e. to find the voltage ranges of V_m and V_D where the anthracene molecular ions can be well stored in Mini-Ring. These voltage ranges reduced in (ξ_D, ξ_m) coordinates are called the stable storage region.

The anthracene cations (12.075 keV) are launched at (x_c, y_c, z_c + 0.5) = (202.5, 130, 0.5) mm without any transversal velocity components. Note that the ideal injection exists rarely in the experiments, the ion injection here is chosen with a small deviation z_c + 0.5 mm to simulate the real case. Other additional deviations on y-axis and/or z-axis will not strongly affect the size or shape of the stable storage region, but may slightly shift this region. The voltages V_m and V_D have been varied through a limited region with certain steps; for each pair of V_m and V_D values, the ion trajectory is simulated and the storage time is recorded. The trajectory quality is chosen at T_{qual} = 103 and the maximum storage time is limited at 10 ms. This simulation of the stable storage region takes about 50 hours. As shown in Figure 3.26, the voltages V_m and V_D are shown in (ξ_D, ξ_m) coordinates, for each pair of ξ_D and ξ_m values, the simulated storage time from 0 to 10^4 μs is illustrated by the change of color from white to blue.

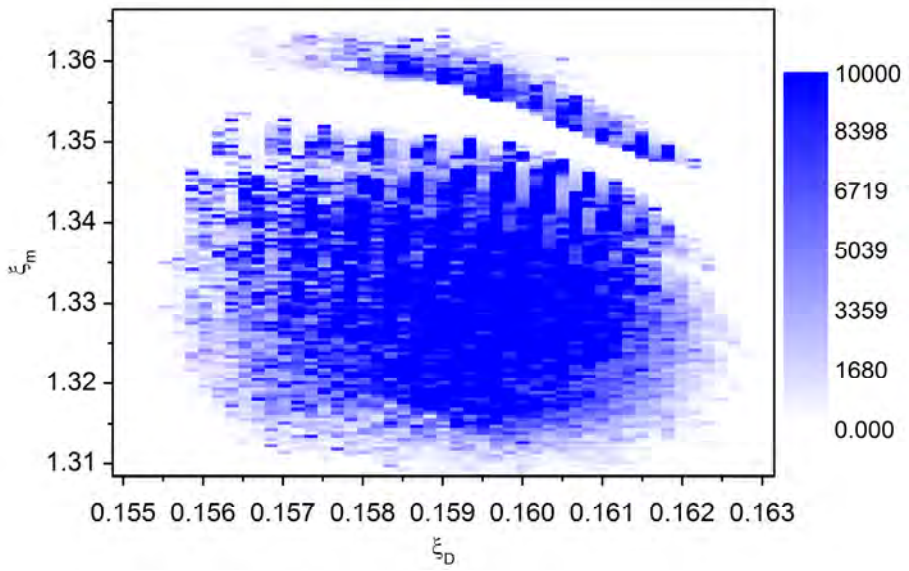

Figure 3.26 Stable storage region of Mini-Ring in (ξ_D, ξ_m) coordinates. The ion trajectory of 12.075 keV anthracene cation is simulated and the storage time is recorded. The change of color from white to blue illustrates the increase of storage time from 0 to 10^4 μs.

From this figure, a broad stable storage region ξ_D (0.1575 ~ 0.1615) and ξ_m (1.315 ~ 1.345) is obtained, this region corresponds to the voltage ranges 1926 ± 25 V for V_D and 16035 ± 180 V for V_m. A strange appearance is that there is a gap between two storage regions at high ξ_m values. Since we titled the four pairs of deflectors by an angle of 7°, the ion trajectory has been optimized with higher V_m on the cone. However, for some cone voltage values (the V_m in the gap), the small deviation z_c + 0.5 mm is amplified each time when the ion approaches the cone, and soon the ion is kicked out from the ring.

In this stable storage region, the center value (ξ_D = 0.1595, ξ_m = 1.328) is chosen to be applied on the cones and deflectors in the following simulations.

3.2.2.2 **Acceptance of Ion Beam Emittance**

For the storage devices, the acceptance of the ion emittance for stable storage trajectories is also an important label to qualify the setup. Here, the simulations to estimate the acceptance of ion beam emittance have also been performed, the parameters ξ_m and ξ_D have been chosen from the center of the stable storage region, and the ions are launched in the center between D_1 and D_2, x_c = 202.5 mm.

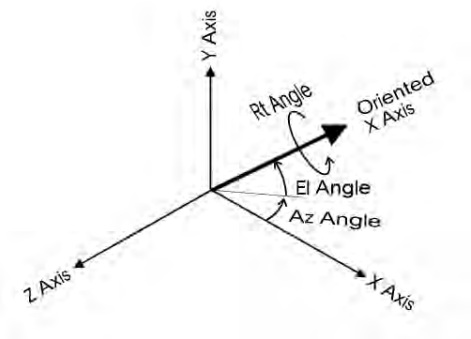

Figure 3.27 Angular orientations, from SIMION's user manual.

Following the angular orientation shown in Figure 3.27, for each y position in the range of y_c ± 4 mm while z = z_c = 0 mm, the azimuth angle α_y has been varied from -30 to 30 mrad to find the corresponding limit for the stable storage. The simulated storage times are plotted in Figure 3.28 (a) in color. Similar simulation has also been performed on z axis and elevation angle β_z to find the acceptance for stable storage on (z, β_z) plane, as shown in Figure 3.28 (b).

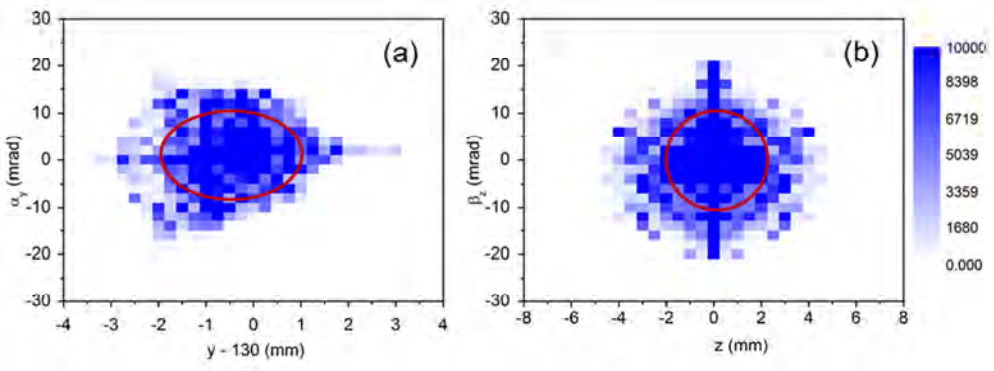

Figure 3.28 Phase space diagrams for ion beam acceptance in Mini-Ring, the change of color from white to blue illustrates the increase of storage time from 0 to 10 ms. Ellipses are used to fit the acceptance. (a) acceptance for stable storage in (y, α_y) plane, α_y is the azimuth angle; (b) acceptance for stable storage in (z, β_z) plane, β_z is the elevation angle.

To describe the acceptance of ion beam emittance in Mini-Ring, ellipses are used to fit the stable storage regions in (y, α_y) plane in Figure 3.28 (a) and (z, β_z) plane in (b), we obtain the acceptances of ion beam emittance 15 π mm × mrad and 20 π mm × mrad, respectively. Comparing to the acceptance of ion beam emittance of 60 π mm × mrad in the large ring ELISA [20], the simulated acceptance of Mini-Ring is much smaller. The small acceptance of Mini-Ring requires strict ion beam injection condition.

3.2.2.3 **Betatron Oscillation**

When the ion bunch is circulating inside Mini-Ring, it is also interesting to follow the ion trajectory turn by turn, especially to study the ion movement in the perpendicular directions to the circulating direction.

In this series of simulations, 12.075 keV anthracene cations are launched at the center of D_1 and D_2 (x_c, y_c, z_c) with small displacements on y or z direction but no transversal velocity component. When the ion is launched at $y = y_c + 0.5$ mm, the y position of the ion is monitored each time when the ion passes the yz plane between D_1 and D_2. As shown in Figure 3.29 (a), the betatron oscillation period is calculated by fast Fourier transform (FFT) to be about 31 μs while the revolution period is 6.5 μs. When the displacement is increased to 2 mm, as shown in Figure 3.29 (b), the betatron oscillation period slightly decreases to 28 μs while the oscillation amplitude increases. On vertical direction, similar simulation has been performed with displacement of $z = z_c + 0.5$ mm, the oscillation period is about 16.5 μs, as shown in Figure 3.29 (c). In conclusion, when the ions are injected with small displacements, the betatron oscillation do exists in both horizontal and vertical directions; and the betatron

oscillation amplitude increases with the increasing displacement while the betatron oscillation period is not significantly affected.

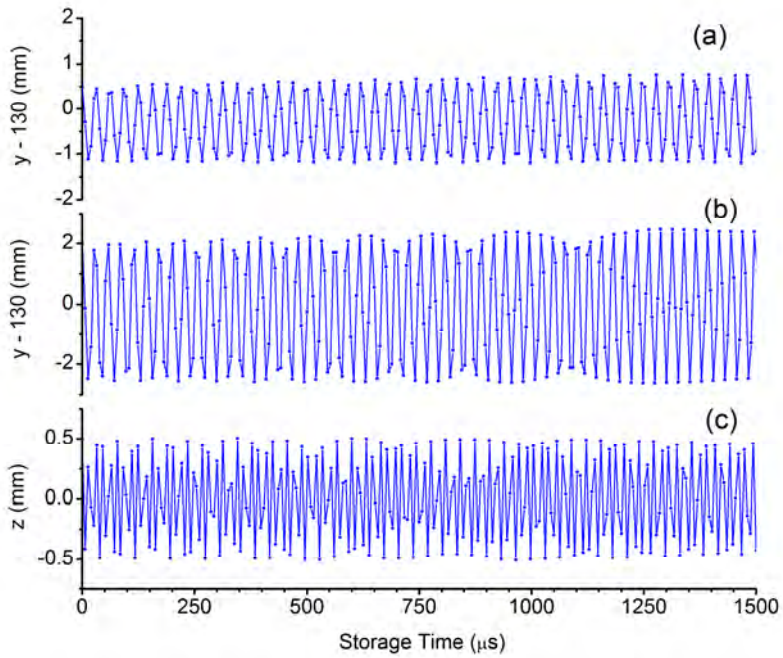

Figure 3.29 Betatron oscillation in horizontal direction with ion launched at (a) $y = y_c + 0.5$ mm and (b) $y = y_c + 2$ mm. (c) Betatron oscillation in vertical direction with $z = z_c + 0.5$ mm. The oscillation periods for these three simulations are simulated as 31 μs, 28 μs and 16.5 μs, respectively.

3.2.2.4 **Kinetic Energy Selectivity**

In the above simulations, by choosing the fixed kinetic energy 12.075 keV of the anthracene cation, we obtained the stable storage region and the suitable geometry of Mini-Ring. Once the geometry of the ring as well as the voltages applied on the cones and deflectors are settled, the kinetic energy selectivity is another feature of the Mini-Ring.

In the present simulation, the voltages (V_D, V_m) = (1926, 16035) V are applied to the deflectors and the cones. With kinetic energy varying from 11.8 to 12.3 keV, the launched ions from the center between D_1 and D_2 with a small displacement on z axis (x_c, y_c, $z_c + 0.5$) = (202.5, 130, 0.5) mm, are circulating inside Mini-Ring. The storage time is recorded as a function of kinetic energy and plotted as blue square in Figure 3.30. The storage time increases strongly at around 11.95 keV and decreases rapidly after 12.15 keV. By choosing 10 ms as the stable storage time limit, a rough kinetic

energy range of about 200 eV in width is obtained; this energy range is the selectivity of Mini-Ring at around 12 keV.

This kinetic energy selectivity is also verified experimentally by changing the extraction voltage of the ECR ion source and monitoring the count rate on MCP detector at the storage time 1.2 ms with time window 500 μs. The count rates are also plotted in the figure as red circles with dash-dot line to guide the eyes. The experimental kinetic energy selectivity is found to be about half of the simulated one, about 100 eV in width. This difference is not surprising since in the simulation we didn't consider all the parameters, for example, the ion launching position and angles dispersions. In addition, the small positioning error of the electrodes, especially the cones in the experiments may also bring influence. In fact, we have observed a small deviation of the ion beam from the horizontal plane after the reflection of the cones in the experiments.

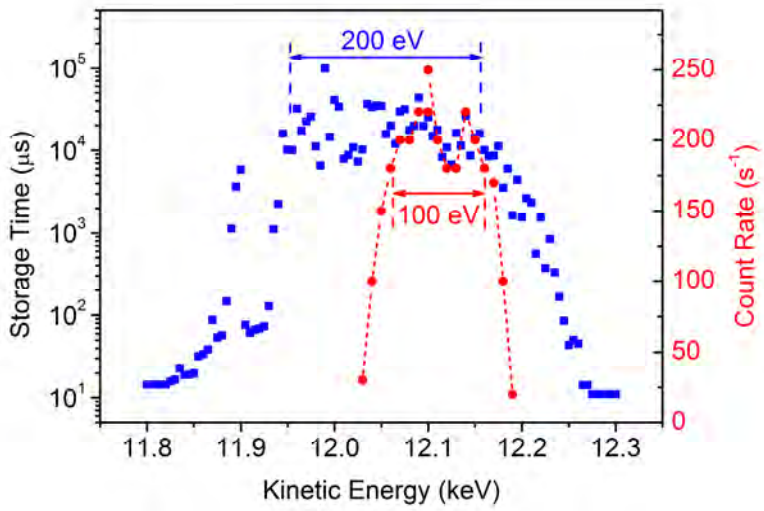

Figure 3.30 Blue square (left axis): storage time of ions as a function of kinetic energy for fixed storage condition of Mini-Ring. Red circle (right axis): count rate on the MCP detector picked up at the storage time 1.2 ms with time window 500 μs, the red dash-dot line is to guide the eyes.

The kinetic energy selectivity indicates that ions with different kinetic energies can be stored together in one ion bunch in Mini-Ring. Note that the different kinetic energies lead to different revolution periods, the direct appearance in the experiment is that the width of the ion bunch increases with storage time, and this brings difficulties to the data analysis.

The kinetic energy selectivity is also of importance to kick out the daughter ions from Mini-Ring after the dissociation process. Here we define the kinetic energy selectivity of Mini-Ring as

$$\frac{\Delta E_k}{E_k} = \frac{\pm 50\ \text{eV}}{12.075\ \text{keV}} = \pm 0.41\%$$

Equation 3-4

This selectivity shows that ions with kinetic energy dispersion of 0.41% around 12 keV can be stored in Mini-Ring. On the other hand, the kinetic energy change from parent ion to daughter ion after dissociation process is proportional to the change of the mass. For the daughter ion, if the loss of kinetic energy due to loss of mass Δm is beyond the kinetic energy selectivity of Mini-Ring, the daughter ions will be ejected out from the ring after dissociation process. This leads to the mass selection of Mini-Ring for the stored ions after dissociation, and the mass selection ability is estimated to be $\frac{m}{\Delta m} = \frac{E_k}{\Delta E_k} \approx 250$. In the case of anthracene cation (m = 178), the loss of H (Δm = 1) and loss of C_2H_2 (Δm = 26) are under the mass selection ability of Mini-Ring. Thus, the daughter ions of anthracene cation after dissociation process will escape from the ring soon after dissociation; and the stored specie is only parent anthracene cation. This is one of the outstanding features of the Mini-Ring.

3.2.3 **Collection of Neutral Fragments**

To estimate the collection of neutral fragments on the MCP detector locating on the downstream of D_3 and D_4, the dissociation of anthracene cation ($C_{14}H_{10}^+$) is taken into account in the simulation. The anthracene cations are launched around (x_c, y_c, z_c) with beam profile in Gaussian distribution with full width at half maximum (FWHM) 0.5 mm; the ion emittance is also in Gaussian distribution with FWHM 0.4°. The anthracene cations are simulated to dissociate at random dissociation times with kinetic energy release (KER) of 0.3 eV. This KER is mainly taken by the lighter fragment after dissociation; the additional velocity to the lighter fragment due to KER is randomly assigned to the x, y and/or z directions in the simulation. The neutral fragments emitted along D_3 and D_4 are collected at the detector position.

As shown in Figure 3.31, the distributions of the emitted neutral fragments are projected to y-axis and z-axis, illustrated in (a) and (b) respectively. In addition, the distribution of neutrals without KER is also simulated to illustrate the ion beam size at the detector position. As noticed, the shape of the neutral distributions on y-axis is not as symmetry as that on z-axis, this may be explained by the turning points of the trajectories at D_3 and/or D_4. The FWHM of the neutral distributions projected on z-axis are estimated to be 2.3, 4.7 and 28 mm for the beam size, C_2H_2 and H, respectively. The position and size of the real MCP detector used in our experiment are also illustrated in the figures by orange arrows. The diameter of the MCP (25 mm)

is smaller than the simulated FWHM of the distribution of H fragments (28 mm) but much larger than that of C_2H_2 fragments (4.7 mm). Thus, we can deduce that some of the H fragments emitted along D_3 and D_4 can't be collected by the MCP detector. The collection efficiency of the MCP is estimated to be about 100% for C_2H_2 fragments and 50% for H fragments.

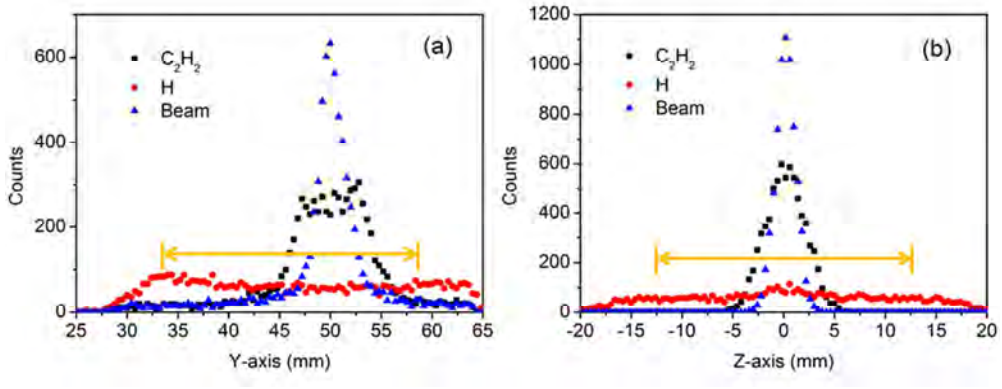

Figure 3.31 Simulation of the distributions of the neutral fragments of anthracene cation at the detector position of the Mini-Ring. Blue triangle denotes the ion beam size. Black square denotes the C_2H_2 fragments and red filled circle H fragments at the detector position. (a) Projections on y-axis (horizontal), (b) Projections on z-axis (vertical). The orange arrows show the position and size of the MCP detector.

In this section, the optical properties of the cone and the deflector have been described, and week focusing effect of the deflector in vertical direction has been found. The stable storage region in (ξ_D, ξ_m) coordinates, the acceptances of ion beam emittance, and kinetic energy selectivity have been simulated with SIMION. With small displacements in horizontal or vertical direction, the betatron oscillation of the stored ions has been discussed. Furthermore, the emitted neutrals with certain kinetic energy release have also been followed at the detector position. All these simulations, have not only confirmed the operation status of the real Mini-Ring in the laboratory, but also given us indications on the improvements of the setup as well as the design of experiments.

3.3 Optimization of Storage

In order to store ions in long time scale and avoid large betatron oscillations, two issues appear to be critical: the ion injection and storage potentials. The ion injection can be optimized by tuning the voltages on the injection optics, while the storage

potential depends on the positioning and voltages of the cones and deflectors [138]. In this section, focusing on these two issues, the optimization of the ion injection and storage will be discussed.

3.3.1 **Visualized Ion Beam Trajectory**

The control of ion injection, as mentioned above, is critical to avoid large betatron oscillation and obtain stable storage. A good ion injection condition is that for most of the ions, their trajectories can match the acceptance of Mini-Ring. In order to achieve this condition, the visualization of the ion beam becomes a powerful online tool for tuning the injection.

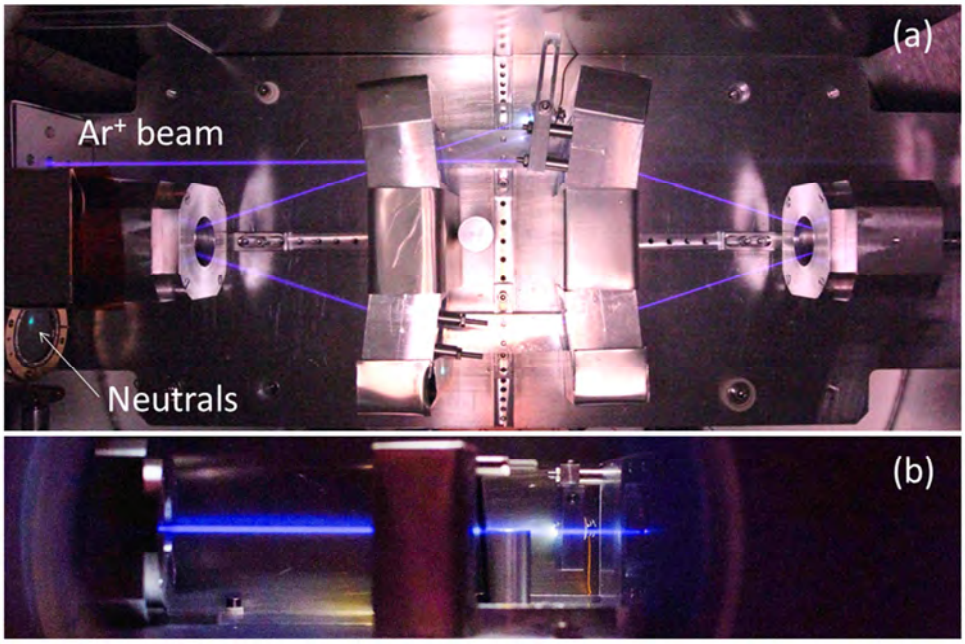

Figure 3.32 Photograph of 12 keV Ar^+ continuous beam stored for a single turn in Mini-Ring, the exposure time is 10 s; the chamber is filled with N_2 gas to 2×10^{-4} mbar. (a) Photograph taken on the top of the ring chamber, the white spot on the MCP is due to the emitted neutrals from the ring. (b) Photograph taken from side window of the ring chamber.

In this optimization experiment, the 4 μA Ar^+ beam extracted at 12 kV is injected into Mini-Ring and stored for a single turn. The voltages on the cones and deflectors are applied except on D_1; the ring chamber is filled with N_2 gas up to 2×10^{-4} mbar to increase the collision with intense ion beam. A commercial digital camera (CANON 5D mark II) equipped with a high sensitivity CMOS capture is used to take photos of the ion beam in the dark room. The camera is placed on the large top window, or in front of the small side window of the ring chamber to measure the ion beam position in horizontal and vertical plane, respectively. As shown in Figure 3.32, the blue

straight lines in the figure are the secondary light coming from the relaxation process of N_2 molecules excited by the collisions with intense ion beam. These blue lines are considered as the beam position in the first turn of storage. In addition, the width of the blue lines can be measured on the photo; the measured value 2 mm is considered as the diameter of the ion beam. The white spot on the down left of Figure 3.32 (a) was produced by the impact of the emitted neutrals on the surface of the MCP detector; the size of the spot is approximately the same as that of the ion beam.

It is noteworthy that, when the voltages on the electrodes change, we can see directly the change of beam position with bare eyes through the windows of the ring chamber. This is a real online tool for tuning the ion injection and storage conditions. By comparing the photos taken from the top and one side of Mini-Ring, the voltages on the lenses and steerers as well as the voltages applied on the cones and deflectors can be finely tuned except that on D_1 since it is turned off at the moment.

The optimization with visualized ion beam trajectory is a direct and effective method to tune the ion injection and the storage of the first turn, this method can offer great help to find the suitable conditions of the injection and storage at the beginning. The only limit is that this method is not precise enough to obtain the stable storage without large betatron oscillation.

3.3.2 **Image of the Neutrals**

After careful optimization in the previous step, we have found good injection and storage conditions. For further optimization, the image of the collected neutrals on the position sensitive MCP detector becomes indispensable. This experiment is carried out under a pressure of 2×10^{-9} mbar without additional gas injection in the chamber, and the ion beam intensity is also limited to protect the MCP detector. A typical ion bunch in width of 2 μs is injected and stored in Mini-Ring for a storage cycle of 2 ms.

The image of the neutrals emitted from D_3 and D_4 is displayed on the computer by the CAMAC data acquisition system (Figure 3.19). Figure 3.33 (a) presents the image of collected Ar atom due to collision induced neutralization from 12 keV Ar^+ beam. The projections of this image in horizontal (X) and vertical (Y) axes are shown on the top and the right side of the image, respectively. The widths of the spot then can be measured on both horizontal and vertical axes from the projections. Obviously, the two widths correspond to the storage status; the thinner widths illustrate a smaller oscillation during the storage. By tuning the voltages on D_1, as well as fine tuning of the voltages on the injection electrodes and storage electrodes, the widths of the spot on horizontal and vertical directions can be reduced. The thinnest widths we can reach on both directions are about 2 mm, which is approximately the diameter of the ion

beam, demonstrating that the scattering angle of the neutrals after collision with the residual gas is rather small. Once the spot size on the MCP equals approximately to the ion beam diameter, the betatron oscillation becomes negligible comparing to the ion beam diameter, we consider that we have approached the ideal storage condition.

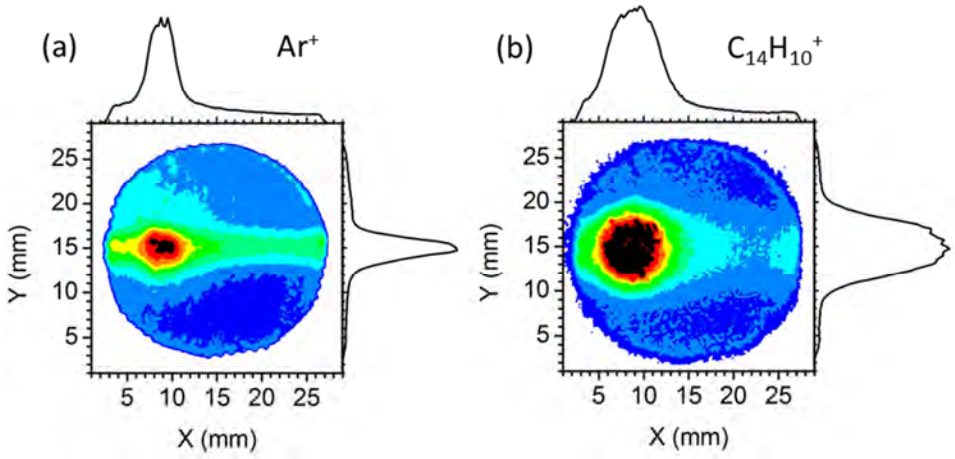

Figure 3.33 Images of the neutrals from the stored 12 keV Ar^+ (a) and anthracene cations $C_{14}H_{10}^+$ (b). The projections on horizontal and vertical directions are shown on the top of and the right of the images, respectively.

We maintain the injection and storage conditions, only change the ion specie from Ar^+ to anthracene cation ($C_{14}H_{10}^+$), the image of the neutral fragments is shown in Figure 3.33 (b), with projections on horizontal and vertical axes shown on the top and the right side of the image, respectively. As noticed, the spot size of the fragments of anthracene cations is much larger than the size of Ar atoms. The neutral Ar atoms are due to neutralization from collision induced electron capture, the scattering angle after collision is rather small; while for anthracene cation, the neutrals mainly come from dissociation process with kinetic energy release (KER). If we compare the image of the two species, the KER for certain dissociation channel, here the loss of C_2H_2 from anthracene cation might be obtained [138].

The neutrals emitted from the ring are recorded as a function of storage time. By selecting the neutral yields turn by turn in region B of Figure 3.19, the corresponding image of the neutrals can also be followed turn by turn in region D. As shown in Figure 3.34 (a), the position of the spot is shown as a function of storage time for both Ar^+ and anthracene cation. We learn that the ion bunch position is oscillating from turn to turn, especially in the first 200 μs; and the oscillation amplitudes reduce strongly after 1 ms. Figure 3.34 (b) shows that the spot diameters of the Ar^+ and anthracene cation vary strongly at the beginning of the storage, while after 1 ms the diameters tend to approximate constant values. Considering the evolution of the betatron

oscillation and bunch diameter, the experiments performed after 1 ms are expected to be more accurate.

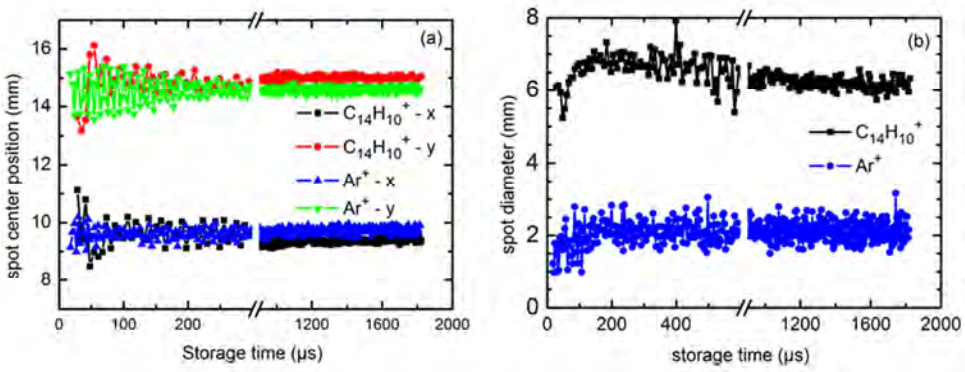

Figure 3.34 (a) Center positions of the spots of the stored ion bunch recorded as a function of storage time in x (horizontal) and y (vertical) coordinates. (b) Diameters (taken from FWHM) of the spots as a function of storage time.

In this section, the tuning process of Mini-Ring has been described; the visualized ion beam trajectory and the image of the collected neutrals have been employed to optimize the ion injection and storage conditions. Using the visualized ion beam trajectory as an online tool, the primary ion injection and storage conditions have been obtained. The second step, by fine tuning of the voltages on the injection and storage electrodes to minimize the spot size of the collected neutrals on the MCP, a good storage condition has been obtained. In addition, the betatron oscillation and the ion bunch diameter were followed as a function of the storage time, which have not only illustrated the storage status during one storage cycle, but also provided indications on the design of the experiments.

Conclusion

In this chapter, a new tabletop electrostatic storage ring, the Mini-Ring has been presented. The design and construction of the entire setup, including the laser equipment and data acquisition system have been described in detail. The simulations of Mini-Ring, concerning the optical properties and operation have been performed in SIMION software. These simulations have verified the operation status of Mini-Ring in the laboratory, and also given indications on the design of experiment. In addition, using the visualized ion beam trajectory and the image from the MCP detector, the optimization of stable storage condition has been described.

Although the design concept of Mini-Ring comes from the ConeTrap, the Mini-Ring combines the advantages of both ESRs and EIBTs. First, about 10^5 ions (ion density: ~10^5 cm^{-3}) with kinetic energy of tens of keV can be stored in the ring up to seconds. The high kinetic energy of the stored ions ensures the detection efficiency of the emitted neutrals, the large amount of ions brings convenience for the statistical experiments, and the long storage time makes the study of relaxation dynamics in different time ranges possible. Second, the excitation of the stored ions and the collection of the neutrals resulting from dissociation can be performed in different straight sections of Mini-Ring; the six straight sections in Mini-Ring bring convenience in the design of experiments. At last, due to the small size of Mini-Ring which leads to very short revolution period of stored ions, the study of relaxation process can start from the very first microseconds after laser excitation.

Chapter 4 Experiments on Anthracene Cation

To investigate the relaxation dynamics of the PAH molecules, the anthracene cation which consists of three fused benzene cycles in linear structure is chosen as a candidate among the PAH molecules in this thesis work, and all the experiments in this chapter are performed on anthracene cation. In the first section, the basics of the experiments will be presented in three subsections separately, including the experimental method, experimental parameters, and data correction. In the second section, by analyzing several different experiments, the time scales and the characteristics of Mini-Ring will be discussed. In the third section, in order to investigate the radiative cooling of anthracene molecular ions, the ions are stored in Mini-Ring up to 8 ms. The fluorescence emission rate as a function of internal energy will be obtained by analyzing the time evolution of the internal energy distribution (IED) as a function of the storage time. The fluorescence cooling rate will be estimated and compared with the infrared cooling rate.

4.1 Experimental Method and Parameters, Data Correction

To understand the relaxation dynamics of anthracene molecular cation, the time evolution of the IED of which turns to be essential. The time evolution of the IED of the stored molecular ions can be probed by analyzing the laser induced neutral yields resulting from delayed fragmentation after photon absorption at different storage times. Based on this concept, the details of the experiment, including the method, parameters and data correction will be presented in this section.

4.1.1 **Experimental Method**

The anthracene cations are produced in the ECR ion source and extracted at 12 kV. After being selected by the mass selection magnet, the ions are chopped into short ion bunches with 1 ~ 2 μs in width. After a total time of flight of 29 μs through the beam guiding line, the ion bunches enter the Mini-Ring through the first straight section D_1 and D_2. The moment to produce the ion bunch is used as the common start (time zero) of the data acquisition for each storage cycle. The molecular ions are stored with a revolution period of 6.5 μs inside the ring until the end of the storage cycle when the ions are ejected out of the ring, and then the ring is open again for the entrance of the next ion bunch. During the storage cycle, a part of the stored molecular ions dissociate spontaneously since they are hot when produced in ECR ion source, leading to the loss of neutral fragments from the ring. The neutral fragments, mainly C_2H_2 and H, emitted due to unimolecular dissociation of stored anthracene cations along D_3 and D_4 are detected at each turn by the MCP detector. With storage time going on, the neutral yield decreases. The heavy daughter ions after emitting neutral fragments are lost from the ring after several turns. At well controlled storage times, laser pulses are employed to excite the stored molecular ions, the schematic of the experiment is shown in Figure 4.1. Laser pulses in width of several nanoseconds are sent into the ring through D_1 and D_2 to merge the ion bunch.

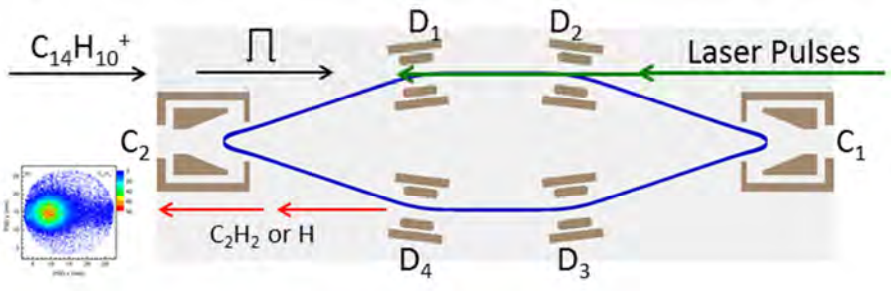

Figure 4.1 Schematic of the experiment design.

After laser irradiation, the laser excited molecular ions will lead to dominant contribution to the neutral emission. The neutral yields are recorded as a function of storage time and over 10^5 storage cycles in order to obtain enough statistics. A typical neutral yield curve is plotted in Figure 4.2, the laser firing time t_{laser} is at 2 ms. By varying t_{laser}, the stored molecular ions can be excited at different storage time, the evolution of the IED is then possible to be obtained by analyzing the laser induced neutral yields.

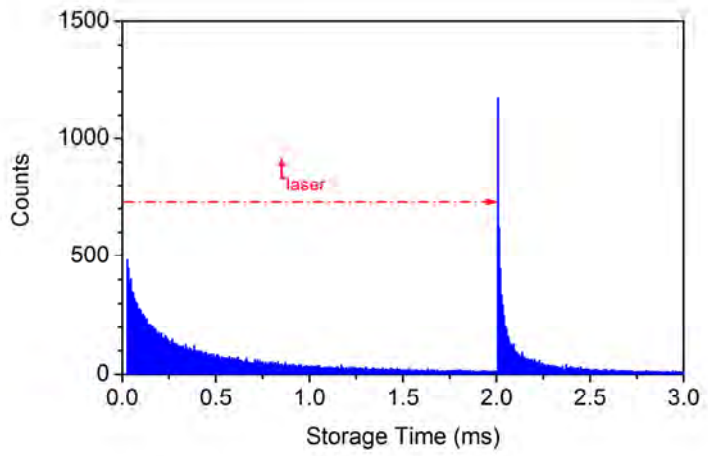

Figure 4.2 Neutral yields as a function of storage time, t_{laser} denotes the laser firing time.

A zoom-in of the laser induced neutral yields from 2 ms is shown in Figure 4.3, the periodic peaks correspond to the revolution of the ion bunch inside the ring, and the peak interval 6.5 µs is the revolution period. The width of each peak is about 1 µs, it represents the length of the zone where the ion bunch and the laser beam overlap. Taking the laser pulse firing time t_{laser} as time reference, the first peak corresponds to dissociation time at 3.25 µs, which is the time necessary for the ion bunch to perform the first half period of revolution from the excitation zone to the detection zone (between D_3 and D_4); this is the minimum time limit to detect the neutral fragments after laser excitation.

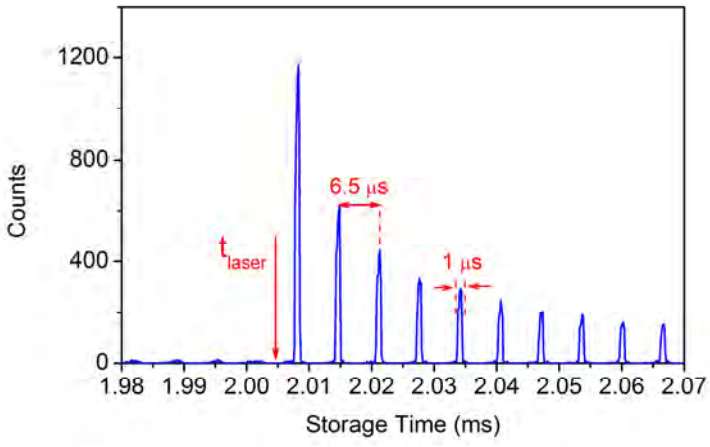

Figure 4.3 Zoom-in of the laser induced neutral yields.

4.1.2 Experimental Parameters

During the experiments, the parameters which may influence the detected neutral yields will be discussed in this subsection, and their influence on the experiments will also be evaluated. More particularly for such an experiment aiming to study the cooling regime of the molecular ions by re-exciting the stored ions with laser pulses, the parameters include the vacuum in the experimental chamber and the storage lifetime, the overlap of the laser pulse and ion bunch, the laser induced population depletion of stored ions, single photon absorption condition, and the number of stops acquired during each storage cycle.

4.1.2.1 Vacuum and Storage Lifetime

The lifetime we discuss here, is the storage lifetime of the molecular ions limited by the collision induced neutralization and/or fragmentation. Following a previous work of Bhushan et al [50], the storage lifetime is expressed as,

$$\tau = \frac{1}{n\sigma\upsilon}$$

Equation 4-1

where n is the density of residual gas, σ in this equation is the destruction cross-section and υ the velocity of stored ions. Obviously, for anthracene cation stored with kinetic energy of 12 keV, their lifetime is mainly determined by the density of residual gas, i.e., the vacuum condition in the ring chamber.

Figure 4.4 presents the neutral yields of stored anthracene cation as a function of the storage time obtained under two vacuum conditions 3×10^{-8} and 3×10^{-9} mbar. In the first several milliseconds, the neutral yields resulting from spontaneous dissociation decrease very fast; while after 10 ms, the neutral yields due to collision induced neutralization and/or fragmentation follow the exponential decay law, showing straight lines in log-linear scales. By fitting the two neutral yield curves from 10 to 100 ms, the lifetimes of anthracene cation under two different pressures are estimated to be 25.2 and 189 ms, respectively. According to Equation 4-1, the collision induced destruction cross-section for the stored anthracene cation is about 10^{-10} cm^2.

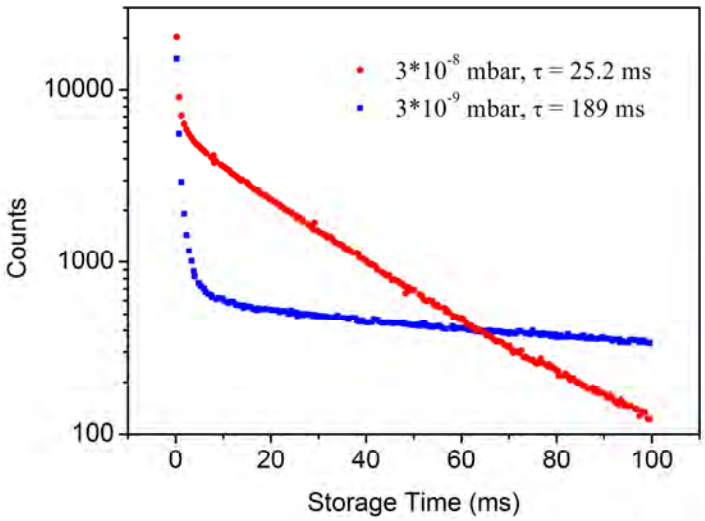

Figure 4.4 Neutral yields of anthracene cation obtained under two different vacuum conditions 3×10^{-8} and 3×10^{-9} mbar. The storage lifetimes are estimated to be 25.2 and 189 ms, respectively.

To compare with the lifetime measurements at other storage devices, the lifetime measurements of 2 and 12 keV Ar^+ ions are also performed in Mini-Ring at different pressures [21], as shown in Figure 4.5. The corresponding results from ConeTrap are also presented in triangle (Stockholm ConeTrap) and filled circle (Lyon ConeTrap), respectively.

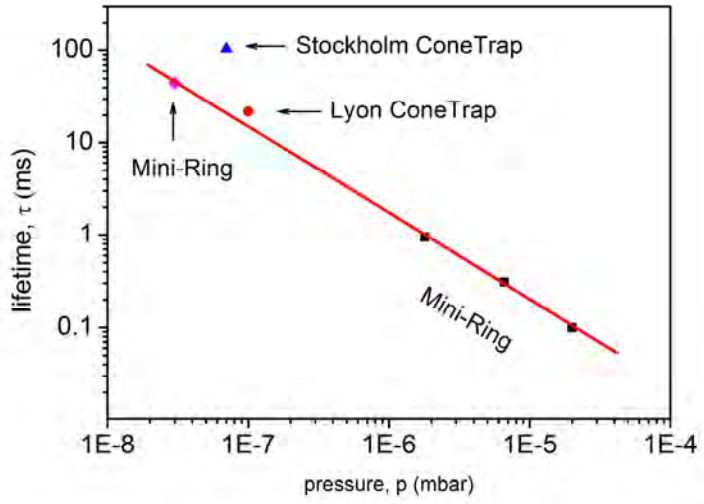

Figure 4.5 Square (diamond): measured lifetimes of 2 (12) keV Ar^+ ion in Mini-Ring. Filled circle: lifetime of 600 eV Ar^+ ions in the Lyon ConeTrap [44]. Triangle: lifetime of 4 keV Ar^+ ions in Stockholm ConeTrap [28]. Full line: a linear fit ($\tau = c/p$) of the measured lifetimes.

Although the kinetic energy of the stored ions varied by a factor of 20 (12 keV comparing to 600 eV), leading to the variation of the velocity by a factor of 4.5, the lifetime measurements can still be approximately described by a simple law: $\tau = c/p$ (shown as red full line in the figure), where p stands for the pressure, c is the fit parameter. This approximate fit illustrates that the storage lifetime is inversely proportional to the ambient pressure (density of residual gas) while the kinetic energy of stored ions plays a relatively minor role.

During the experiments on anthracene cation in this work, the pressure in the ring chamber is even lower than that mentioned above, which is maintained at 2×10^{-9} mbar. Under such vacuum condition, the collision induced neutralization is very rare, and the storage lifetime of anthracene cation is estimated to be about 300 ms.

4.1.2.2 **Overlap of Laser Pulse and Ion Bunch**

As illustrated in Figure 4.1, the laser pulses are sent though D_1 and D_2 to merge the stored ion bunch, thus the overlap of the laser pulse and ion bunch is critical to the excitation of the stored molecular ions. In this experiment, two kinds of overlaps, the time overlap and the position overlap must be well adjusted.

First, we talk about the time overlap. Since the revolution period of the anthracene molecular ions T_{ion} in the ring is only 6.5 μs, by adjusting the laser firing time t_{laser} slowly with respect to the production time of the ion bunch over one revolution period, a good time overlap is expected to be obtained when the laser induced neutral yields reach the maximum. If multiple laser pulses are employed to irradiate the molecular ions at different times during one storage cycle, the phase synchronization of the ion revolution and laser pulses becomes of importance. The phase synchronization condition is given by $\frac{f_{ion}}{f_{laser}} = \text{Integer}$, where $f_{ion} = \frac{1}{T_{ion}}$ stands for the ion revolution frequency and f_{laser} for laser pulse frequency which is variable from 900 to 1000 Hz. By changing f_{laser}, for instance to 999 Hz, thus we obtain $\frac{f_{ion}}{f_{laser}} = \frac{1}{6.5\times10^{-6}\times999} \approx 154$, the ion revolution frequency and laser pulse frequency are well synchronized, and good time overlaps are obtained at different storage times, as illustrated in Figure 4.6. The laser induced neutral yield peaks are always in the center of the ion bunch at 0.98, 1.98, 2.98 and 3.98 ms of the storage times.

The position overlap is more difficult to obtain because of the small diameters of both the laser beam and the ion bunch; which are typically about 2.5 and 2 mm, respectively. Due to the high resolution TDC 4208, the zoom-in of the laser induced

neutral yields can help to monitor the overlap condition. By adjusting the mirrors on the laser path slightly and follow the change of the laser induced neutral yields in the zoom-in, a good position overlap condition is possible to be obtained.

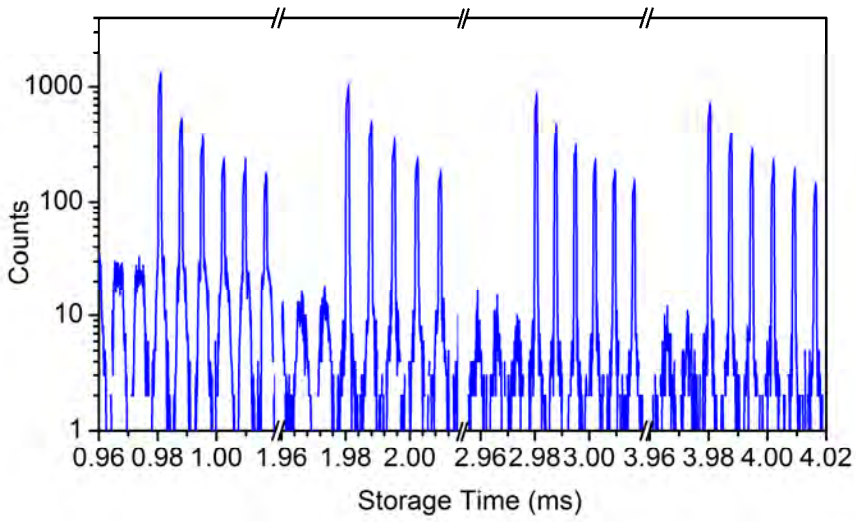

Figure 4.6 Time overlaps of laser pulses and stored ion bunch at 0.98, 1.98, 2.98 and 3.98 ms, laser pulse frequency is 999 Hz. The vertical scale is plotted in logarithmic scale to show the background counts.

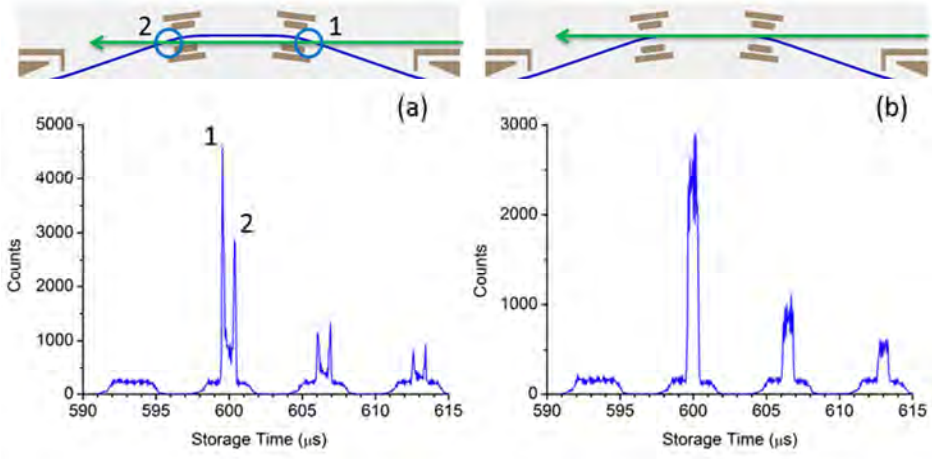

Figure 4.7 The neutral yields under two overlap conditions. (a) The laser pulse only excites two fractions of ions close to D_1 and D_2, shown with blue circles and numbers 1 and 2. (b) Good overlap condition.

For instance, if the double narrow peaks are obtained in the experiments as shown in Figure 4.7 (a), we can deduce that the laser beam is probably parallel to the ion beam in the D_1 - D_2 section but crosses the ion bunch only at two small segments close to D_1 and D_2, as illustrated on the top of (a). By tuning the laser path, a broad single

peak can be obtained, as shown in Figure 4.7 (b); the overlap condition illustrated on the top of (b) is considered as the good one.

4.1.2.3 **Population Depletion of Stored Ions**

During a storage cycle, the population depletion of the stored ion bunch can mainly be attributed to three processes: purification, neutralization and dissociation. After the injection into the ring, the ion bunch starts to lose ions with bad trajectories; this process is called purification and mainly occurs in the first tens of turns in the revolution. Under well-optimized injection and storage conditions, the purification process will not reduce the ion population significantly and therefore be considered negligible. The second process is the collision induced neutralization, which is independent of the internal energy of stored ions and always existing during the storage cycle. Under the very low pressure 2×10^{-9} mbar, as discussed in paragraph 4.1.2.1, it is a slow process with lifetime τ of about 300 ms. The spontaneous dissociation depletes the hot population of the ion bunch mainly during the first 1 ms.

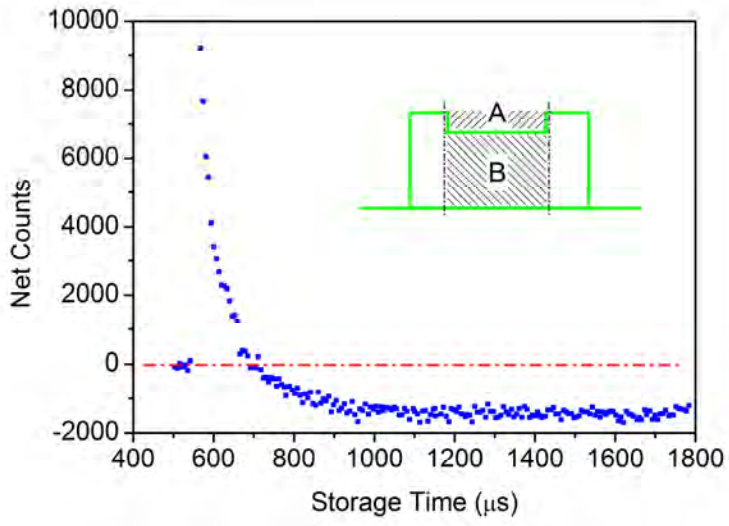

Figure 4.8 Net neutral yields with laser pulse firing at t_{laser} = 540 μs obatianed by subtracting the background neutral yields. The negative value stands for the lost population in the ion bunch, as illustrated as region A in the insert figure.

The most important population depletion process in this work is the laser induced dissociation which is used as a probe to investigate the IED of the stored ion bunch. As shown in Figure 4.2, the laser pulse brings intensely enhanced neutral yields. The percentage of the lost ion population due to laser excitation is tightly related to the rest population still stored in the ring, their determination is essential in the experiments when multiple laser pulses are used. For this purpose, two experiments under identical conditions have been performed, one with laser pulse excitation at 540 μs and the

other without laser pulse recorded as background neutral yields. By subtracting the background neutral yields from the laser induced neutral yields, the net neutral yields due to laser pulse irradiation is obtained, as illustrated in Figure 4.8.

As noticed, intense neutral yields appear after laser excitation, but after 700 μs of the storage time, the net neutral yields turn to negative values and reach about -1450 then become stable. This negative value is proportional to the lost population of the ion bunch due to laser excitation. It corresponds to the integral of the region A in the insert figure. The ratio $\frac{Sum(\mathrm{A})}{Sum(\mathrm{A}+\mathrm{B})}$ corresponds to the percentage of the lost population due to laser irradiation. It is estimated to be about 15% under the laser pulse irradiation of full power 2000 μJ per pulse. In the following experiments, the laser pulses work with much lower power like 400 μJ per pulse, thus the lost population due to each laser pulse excitation is estimated to be about 3 ~ 4%.

4.1.2.4 **Single Photon Absorption and Energy Shift**

For anthracene molecular cation, as discussed in subsection 2.1.1 of chapter 2, the internal conversion process transfers the absorbed photon energy to vibrational degrees of freedom in fs to ps time scale, which is much shorter than the duration of the laser pulse in ns scale. Therefore, during one laser pulse irradiation, the absorbed photon energy maybe redistributed to the vibrational modes of the molecular cation instantaneously before the next photon being absorbed. Then the molecular cation may absorb several photons during one laser pulse. The multiphoton absorption probability P_n follows the Poisson distribution [59] [63] [139]:

$$P_n = \frac{A^n}{n!}e^{-A}$$

Equation 4-2

where n stands for the number of photons absorbed, and A equals to the photon absorption cross-section σ times the photon flux D:

$$A = \sigma D$$

Equation 4-3

The photon flux D is proportional to the power of laser pulse. Assuming that the absorption cross-section σ is constant for given molecular cations absorbing photons with a given wavelength, then A is proportional to the power of laser pulse. Following Equation 4-2, the photon absorption probabilities P_1 - P_4 are plotted as a function of A, as shown in Figure 4.9. The photon absorption probability curves are roughly

partitioned into two regions by $A = 1$. In the region $A < 1$, the one photon absorption is the dominant process and n-photon absorption probability P_n is approximately proportional to $A^n/n!$. In the region $A > 1$, the absorption probability curves reach their maximum values. At the maximum of each curve for a given n, from the derivative of $P_n(A)$ with respect to A, $\frac{\partial P_n(A)}{\partial A} = 0$, we obtain $A = n$. Thus in the region $A > 1$, $n = A = \sigma D$ indicates the average number of photons absorbed during one laser pulse.

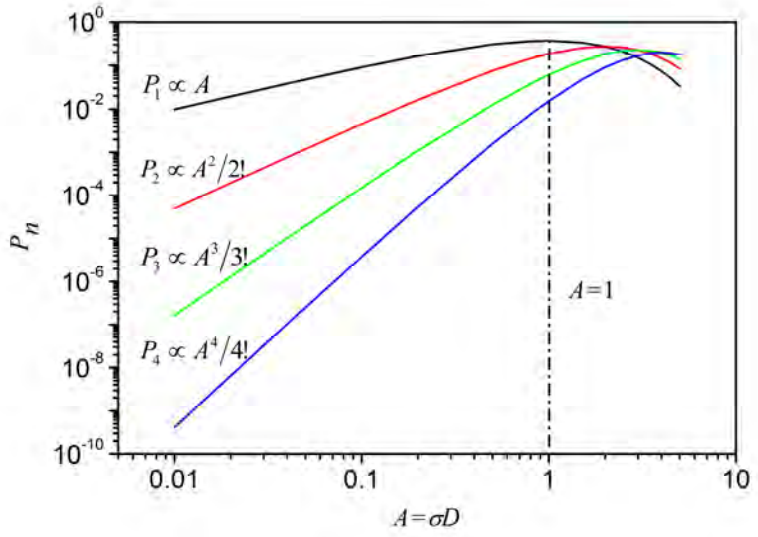

Figure 4.9 Photon absorption probabilities as a function of $A = \sigma D$.

Under low laser power condition ($A < 1$), the laser induced neutral yields from laser excited population is mainly due to single photon absorption and should be proportional to the single photon absorption probability P_1. In addition, considering the approximation $P_1 \approx A$ and $A = \sigma D$, the laser induced neutral yields due to single photon absorption should increase linearly with the power of laser pulse. The experiments on anthracene cation in this work are always performed under the condition $A < 1$ by limiting the power of the laser pulse. The single photon absorption condition is ensured by verifying the linear dependence of laser induced neutral yields on the power of the laser pulse.

Apart from the absolute value of the neutral yield, the dependence of the neutral yield curve on the laser power should be also verified. As illustrated in Figure 4.10, a part of the population excited by two photons into the sensitive energy window should be much more sensitive to the power of laser pulse comparing to the population excited by one photon, leading to significant modification of the energy distribution when the power of laser pulse changes. Note that, an assumption is made here that the entire photon energy has been transferred to vibrational excitation after the photon

absorption. Following the calculations in subsection 2.3.5 of chapter 2, the decay factor α is very sensitive to the variation of population inside the sensitive energy window. Thus, the dependence of α on the power of laser pulse may also offer information about the number of absorbed photons. If α increases fast with the power of laser pulse, multi-photon absorption may play important role in experiments. However, which is not the case in our experiment where the decay factor α barely increases with the power of laser pulse, indicating that the multi-photon absorption in our experiment is negligible.

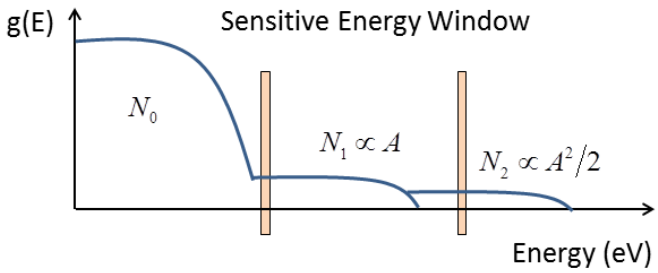

Figure 4.10 Illustration of the population excited by single photon and two photon absorption process, noted as N_1 and N_2, respectively; N_0 stands for initial population.

With each laser pulse, only a small fraction of ions inside the ion bunch are excited, their internal energies are shifted to higher values by the amount of the photon energy, the IEDs before and after laser excitation can be illustrated as in Figure 4.11. The IED of the ion bunch after laser excitation can be expressed as,

$$g'(E) = g(E) \times (1 - P_1) + g(E - h\nu) \times P_1$$

Equation 4-4

where $g(E)$ stands for the IED before laser excitation, P_1 for single photon absorption probability and $h\nu$ for the photon energy. The second term in this equation represents the laser excited ion population while the first term represents the unexcited population. Since the laser excited population contributes dominantly to the laser induced neutral yields, hereafter when we talk about the IED after laser excitation we always refer to the laser excited population part while the unexcited part are not considered. Therefore, we have

$$g'(E) = g(E - h\nu) \times P_1$$

Equation 4-5

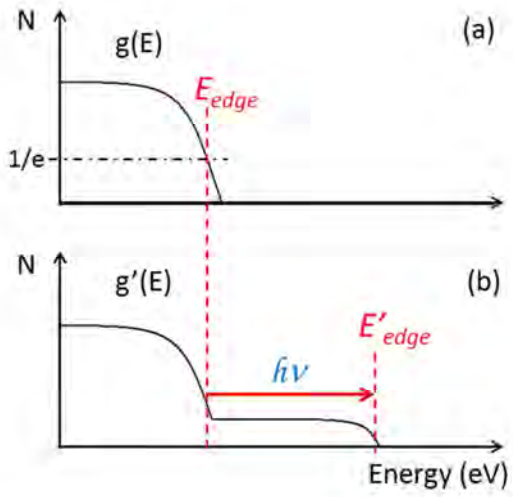

Figure 4.11 The IEDs and high energy edges of molecular ion bunch before and after laser excitation.

As discussed in subsection 2.2.2, for hot anthracene cations with energy difference of 1 ~2 eV, the absorption cross-section of a given photon is assumed to be constant. Thus for the molecular ions at around the high energy edge, the absorption cross-section P_1 is considered to be constant as a function of energy E. Then the high energy edge of the IED $g'(E)$ after laser excitation is expected to be the same shape as the IED $g(E)$ before laser excitation. In the following discussions on the profile of the IED in this chapter, P_1 in Equation 4-5 will be replaced as 1 for simplicity.

Following the definition of E_{edge} (Equation 2-16), the high energy edge of the IED $g'(E)$ is defined with $g'(E'_{edge}) = g_0'/e$. The relation between the two energy edges before and after laser excitation under single photon absorption condition is obtained,

$$E'_{edge} = E_{edge} + h\nu$$

Equation 4-6

With this relation, we can easily subtract the photon energy to obtain the IED before laser excitation.

4.1.2.5 **Number of Stops per Storage Cycle**

As discussed in subsection 3.1.5 of chapter 3, the fast TDC 4208 has maximum 8 stops and full time range 8 ms, thus the TDC can only record up to 8 events during 8 ms in one storage cycle, and the number of stops is monitored on the interface of the CAMAC acquisition system. In order to record less than 8 events during each storage

cycle, the number of the injected ions is limited by the slit in front of the ring chamber. In addition, the Clear function can be used to skip the uninteresting events to take full advantage of the 8 stops, and shift the recording time range as well. Therefore, the consequence due to the limits of TDC 4208 can be easily reduced. Another limit of the acquisition is due to the long conversion dead time of MCP electronics, 3 μs. Since the conversion dead time 3 μs is longer than the typical bunch width 1 ~ 2 μs, the MCP electronics can only process one event in one revolution period. If two events occur close to each other in one revolution period, the second one will not be recorded. In this paragraph, the possibility of losing event will be discussed by monitoring the number of stops during each storage cycle.

Considering an experiment with storage time 2 ms and recording up to 8 stops per storage cycle. The revolution period of anthracene cation in Mini-Ring is 6.5 μs, thus during each storage cycle the number of revolution periods is $2\ \text{ms}/6.5\ \mu\text{s} \approx 307$. For statistically distributed 8 events, the average possibility to record one event per revolution period is then obtained,

$$\overline{p_1} = \frac{8}{307} = 2.6\%$$

The possibility to record two events (if possible) in one revolution period is,

$$\overline{p_2} = \overline{p_1}^2 = 0.07\%$$

This possibility is pretty small and can be neglected. In another word, even if we record up to 8 stops per storage cycle 2 ms, the possibility to have two events in one revolution period is still negligible.

However, the discussion above bases on the assumption that the events are statistically distributed when each revolution period has almost the same weight. For the laser induced dissociation, the neutral events distribute intensively after laser firing time, as shown in Figure 4.12. In this experiment, the average number of stops is 8, but the weight of each revolution period is very different. Here we choose the first peak after laser irradiation which has maximum weight, noted as W_1,

$$W_1 = \frac{\text{Count}_{\text{1st peak}}}{\text{Count}_{\text{Total}}} = \frac{11890}{530330} = 2.24\%$$

where the numerator and denominator are the total count of the first peak and that of all peaks, respectively. The possibility to record one event during the first revolution period after laser irradiation is

$$p_1 = W_1 \times 8 = 18\%$$

where 8 is the average number of stops. Then the possibility for two events to occur during the first revolution period after laser irradiation is

$$p_2 = p_1^2 = 3.2\%$$

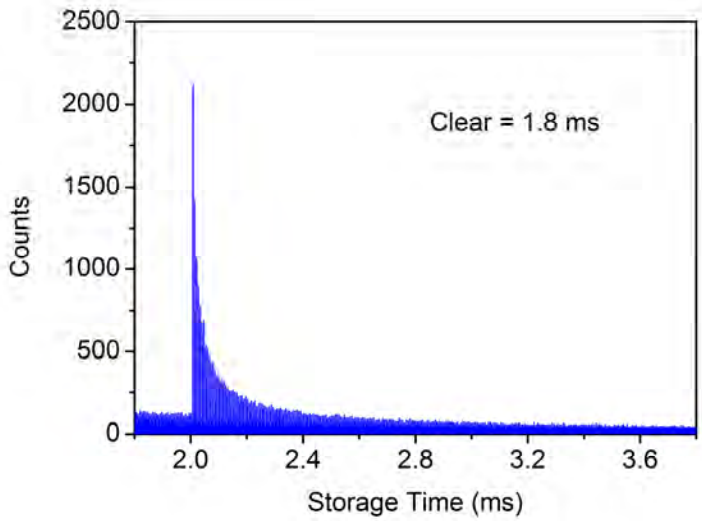

Figure 4.12 Laser induced neutral yields with t_{laser} = 2 ms, Clear = 1.8 ms. The average number of stops is 8.

Thus we can deduce that, about 3% of total events are lost in the first revolution period after laser irradiation. Fortunately, the percentage decreases quadratically with the average number of stops. In this thesis work, the average number of stops is always limited at around 4, then the lost events reduced to less than 1% are considered to be negligible.

Although the number of stops limited in the experiments is low, benefiting from the high repetition rate of the laser pulses, the experiment can be repeated in high frequency, for instance 200 Hz for storage time of 5 ms. It usually takes about 60 min to record one neutral yield spectrum accumulating ~10^5 storage cycles with enough statistics.

4.1.3 **Data Correction**

In the above subsection, several manageable experimental conditions have been discussed, however, there are also some other experimental conditions that are not easy to control due to the design of the experiment. Thus, suitable data corrections are of importance to reduce the influence of these uncontrollable experimental conditions.

In this subsection, the corrections concerning the background counts, change of ion beam intensity, and the evolution of ion bunch profile will be discussed.

4.1.3.1 **Background Counts and Ion Beam Intensity**

During the experiment, the neutral yields contributed by spontaneous dissociation and especially collision induced neutralization are usually considered as background counts. As illustrated in Figure 4.13 (a) and region (II) in (b), the background counts exist during the entire storage cycle. In the experiments with laser pulse irradiation (Figure 4.13 (b)), in order to obtain the net laser induced neutral yield decay curves, the correction of background counts is essential. With a first method, we analyze ten revolution periods on the neutral yield spectrum just before the first laser induced peak. For each background neutral peak, we estimate the total count in a selected time interval at the same phase as the laser induced peaks. The obtained neutral yields for the selected ten revolution periods are fitted with an exponential decay law. This fit is extended to the time region after laser excitation and considered as the background yield versus storage time. By subtracting the estimated background yield, the net laser induced neutral yield curve is obtained. With a second method, we record a background spectrum (Figure 4.13 (a)) under the identical experimental conditions as that for the laser induced spectrum (Figure 4.13(b)). Then by subtracting the first spectrum from the second one, the net laser induced neutral yield spectrum is obtained.

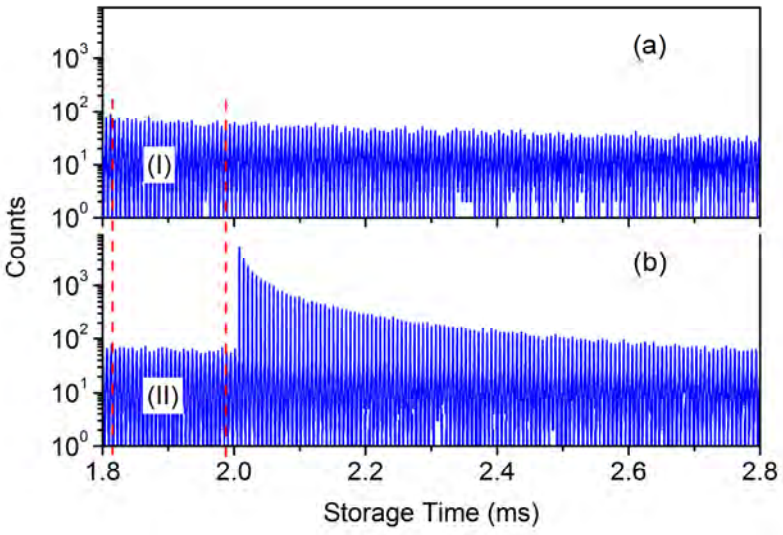

Figure 4.13 Neutral yield spectra acquired without laser pulse (a) and with laser pulses (b) excitation, the vertical scales are plotted in logarithmic scale to show the background counts.

The background counts have linear dependency on the number of ions in the ion bunch which is proportional to the ion beam intensity. During a series of experiments

especially when the experiments are performed during several days, the ion beam intensity may fluctuate slightly. The background counts can be used to normalize the neutral yield spectra performed under different beam intensities. For instance, by selecting the same time range (noted as I and II in Figure 4.13) before the laser firing time on two spectra, we can normalize two spectra with the ratio of the total count of the region I and II.

4.1.3.2 **Time Evolution of the Ion Bunch Profile**

After being injected into the ring, the evolution of the ion bunch profile as a function of time plays an important role in the experiments. For instance to compare the laser induced neutral yield curves obtained at two different storage times, the influence due to the time evolution of ion bunch profile should be excluded. The time evolution of the ion bunch profile can be resulted from the following aspects: the kinetic energy dispersion, different trajectories, Coulomb repulsion between ions and scattering due to elastic collisions with residual gas. Due to the relative low molecular ion density and high vacuum condition, the contribution from Coulomb repulsion and scattering due to collision are considered negligible. Then the kinetic energy dispersion and different trajectories are the main factors causing the evolution.

As discussed in 4.1.3.1, the neutral yields resulting from spontaneous dissociation and/or collision induced neutralization have linear dependency on the number of ions in the ion bunch. Therefore, for each revolution period, the time spreading of the neutral yields is directly related to the profile of the ion bunch. To follow the evolution of the ion bunch profile as a function of time, a multi-parameter function $h(t)$ is employed to fit the time dependence of the neutral yields period by period,

$$h(t) = A \times \frac{1}{e^{\frac{t-t_1}{\tau}} + 1} \times \frac{1}{e^{-\frac{t-t_2}{\tau}} + 1}$$

Equation 4-7

where A stands for the amplitude, $\frac{1}{e^{\frac{t-t_1}{\tau}} + 1}$ and $\frac{1}{e^{-\frac{t-t_2}{\tau}} + 1}$ are used to describe the right and left edge of the neutral yield peak respectively. t_1 and t_2 are the time corresponding to the half-maximum amplitude, τ is a parameter to describe the deviation from the square shape, as illustrated in Figure 4.14.

Defining the center time of the ion bunch $t_c = (t_1 + t_2)/2$, and the half width at half maximum (HWHM) $\Delta t = (t_1 - t_2)/2$, the Equation 4-7 can be simplified as

$$h(t)=\frac{A}{2e^{-\frac{\Delta t}{\tau}}\cosh(\frac{t-t_c}{\tau})+e^{-\frac{2\Delta t}{\tau}}+1}$$

Equation 4-8

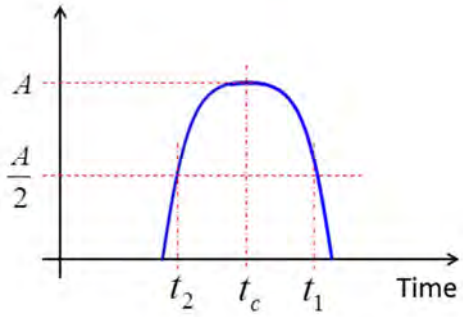

Figure 4.14 Multi-parameter function to fit the ion bunch profile.

For each neutral yield peak, the central time t_c is given, and the evolution of peak profile can be described by the other parameters: Amplitude *A*, HWHM *Δt* and deviation from square shape τ. Figure 4.15 illustrates the fits of the experiment neutral yield up to 2 ms, the vertical scale is plotted in log scale to show the small counts at long time range. The fitted parameters *Δt* and τ are plotted in Figure 4.16 (a) and (b), respectively.

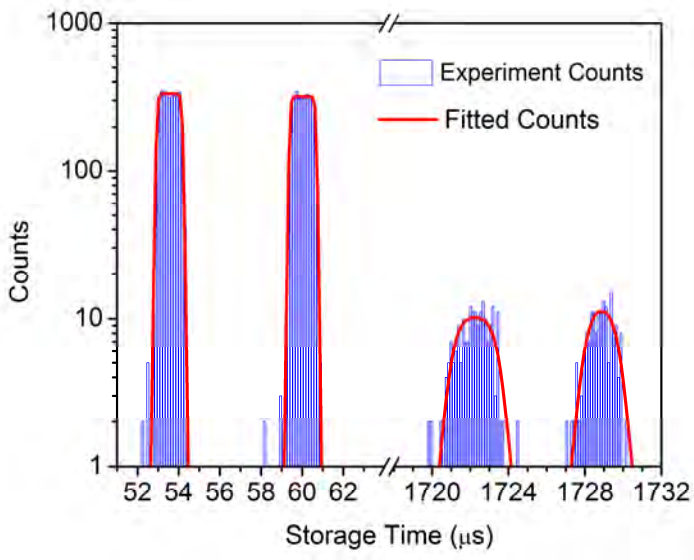

Figure 4.15 Fit of the time dependence of the neutral yield peak period by period.

Although the counts are low at long time range, as shown in Figure 4.15, which leads to the uncertainty of the fit as well as the dispersion of the parameters, we can still follow the tendency of the two parameters. The HWHM of the neutral yield, *Δt*

slightly increases with storage time. The time constant τ increases almost linearly with time. The variations of the two parameters indicate that the width of the ion bunch increases slowly with storage time, and the shape of the ion bunch deviates gradually from the initial square shape and tends to a smooth shape.

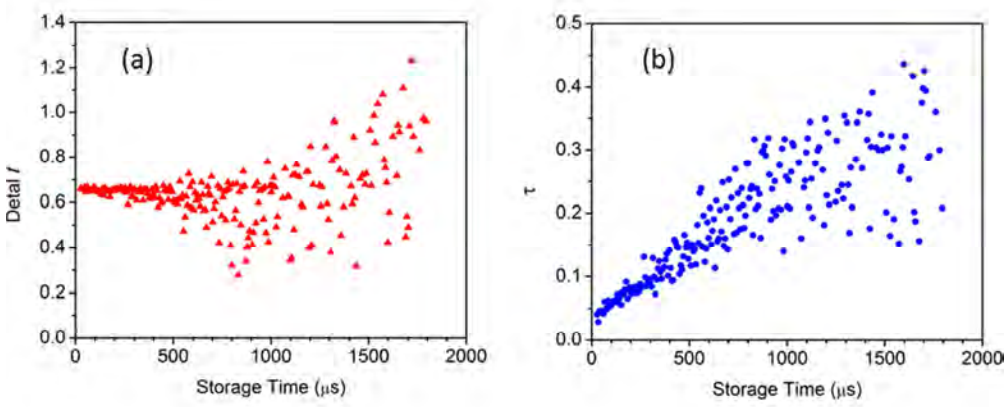

Figure 4.16 Fitted parameters of the neutral yield peaks as a function of time. (a) HWHM Δt; (b) deviation τ from square shape.

Note that the variation of ion bunch profile is a slow process, its effect becomes visible in millisecond time range. For the laser induced neutral yields in a time range of about 100 μs, the change of the ion bunch profile is negligible. However, to compare the laser induced neutral yields due to two laser pulses irradiating at very different storage times t_{laser1} and t_{laser2}, $t_{laser2} - t_{laser1} > 1\,\text{ms}$, the effect due to the evolution of ion bunch profile must be corrected.

In this section, a basic description of the experiment has been presented: the experimental method was introduced in the first subsection, the schematic of the experiment and the neutral yields obtained from experiment have been presented. The experimental parameters like vacuum condition and molecular ions lifetime, depletion of ions due to laser irradiation, the single photon absorption condition as well as the number of stops during each storage cycle have also been discussed in detail. Finally, the corrections of the neutral yield from the experiments have been discussed, and net laser induced neutral yields can be obtained from the experiments with suitable corrections.

4.2 Time Scales in Mini-Ring Experiments

Three experiments on anthracene cation at different storage time ranges will be presented in this section. The characteristics of Mini-Ring and the design of the experiment like the choice of the time range and photon wavelength chosen to excite the stored ions will be discussed in detail. In the first subsection, an experiment performed without laser pulse irradiation will be discussed, by analyzing the obtained spontaneous neutral yield curve, the cooling processes and their corresponding time ranges can be roughly determined. In the second subsection, the decay factor α is used to describe the decay tendency of the laser induced neutral yield curves, and furthermore to help to probe the shift of the IED of the molecular ion ensemble. The characteristic time window and the corresponding energy window of Mini-Ring will be discussed, and the relative neutral yields we can collect in Mini-Ring will be compared with a larger electrostatic storage device. In the third subsection, by irradiating the stored molecular ions with two different photon energies independently, two series of decay factor α will be obtained, and the energy shift rate of the IEDs can be easily estimated. In the fourth subsection, by reproducing the experimental neutral yields, three different multi-parameter functions will be compared to evaluate their ability to represent the IED of stored molecular ions.

4.2.1 **Spontaneous Dissociation**

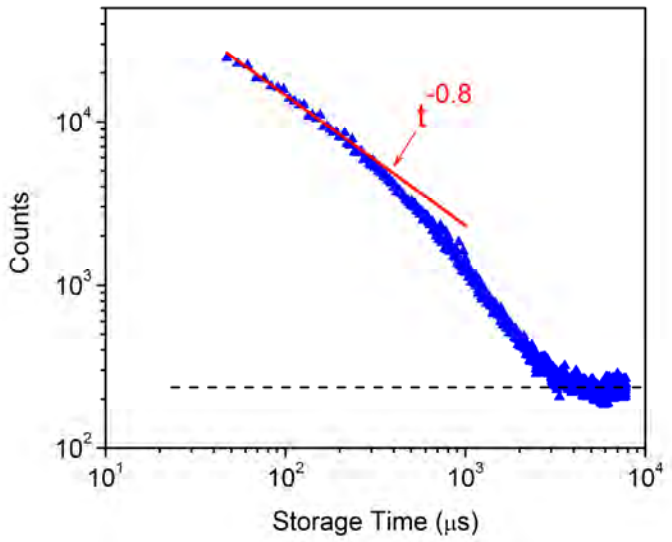

Figure 4.17 A spontaneous neutral yield curve without laser irradiation. The black dash line shows the contribution of collisions with the residual gas.

To get a spontaneous neutral yield curve, the laser pulses are not used; only the neutral yields due to spontaneous dissociation as well as the collision induced dissociation and/or neutralization are collected by the detector. The count of the

neutral yields integrated over each revolution period is plotted as a function of the storage time. Figure 4.17 displays such a neutral yield curve accumulated over about 3×10^5 ion bunches, note the logarithmic scales.

As we can see from the figure, the neutral yield curve presents three distinct regions: the time dependent power law distribution in short time range, the exponential decay in long time range and a fast decrease in the intermediate time range. These distinct regions indicate different physical regimes involved in the cooling process of the molecular ions. The spontaneous neutral yield curve can be fitted by a multi-parameter function as in the work of J. U. Andersen et al on amino acids [64],

$$N(t) = \frac{N_0}{e^{t/\tau} - 1}\left(\frac{t}{\tau}\right)^{\delta} + N_{BG}(t)$$

Equation 4-9

where τ is a time constant, δ a dimensionless parameter, N_{BG} the contribution of collision with residual gas and N_0 a normalization constant. From the obtained fitting parameters (δ = 0.2 and τ = 1 ms), we notice that the neutral yield curve at short time range ($t < \tau$) follows approximately $t^{-\alpha}$ distribution, here α is the decay factor, $\alpha = 1 - \delta = 0.8$. This distribution is attributed to the delayed dissociation of hot anthracene cations produced in the ECR ion source. In the intermediate time range from about 1 to 3 ms, the neutral yield curve decreases very fast and deviates significantly from $t^{-0.8}$ distribution. This suggests the appearance of other competing cooling mechanisms which does not lead to the loss of neutral fragments. Similar behavior has been observed from amino acids and interpreted as a quenching of dissociation by radiative cooling [64]. Following this previous work, our fitted characteristic time τ is interpreted as the quenching time, after which the radiative cooling becomes competitive with dissociation. The quenching time τ has been found typical in the range of 9 to 17 ms for amino acids, around 1 ms for the electron detachment of aluminum cluster anions [69] and 1 ms in the present work. At longer time range (t > 3 ms), the neutral yield curve follows an exponential decay with time constant of about 300 ms, which is the storage lifetime limited by the collision with residual gas. This suggests that at longer time scale (t > 3 ms), the neutral yields are mainly produced by the collision induced dissociation and/or neutralization.

Therefore, from the analysis of the spontaneous dissociation neutral yield curve of anthracene cation, we deduce that the cooling processes occur as a function of the storage time as following: after the extraction in the ECR source, the molecular ion ensemble is first “cooled” down by the depletion of high energy population dominantly via dissociation process until the quenching time 1 ms. After the quenching time, as discussed above, the radiative cooling process becomes

competitive with dissociation. Thus, from 1 to 3 ms, the high energy population are partly depleted via the dissociation and partly transferred to lower energy region via radiative cooling. The contribution of radiative cooling becomes more and more important with increasing storage time. After 3 ms, the dissociation becomes a minor process and it could no longer induce significant population depletion to the surviving "cold" molecular ions. Any further evolution of the IED should be essentially governed by the radiative cooling.

In this subsection, by analyzing the spontaneous neutral yield curve, we identify two kinds of cooling processes at different time range. At short storage time range, $t <$ 1 ms, the dissociation is found to be the dominant cooling process. At long time range $t >$ 3ms, the radiative cooling is considered as the dominant process. This is of importance for the discussion and interpretation in the following experiments.

4.2.2 **Characteristics of Mini-Ring Experiments**

In this subsection, starting by using the decay factor α to describe the experimental neutral yields, the time widow and energy window, the choice of photon energy, and the relative neutral yields we can collect in Mini-Ring experiments will be discussed.

4.2.2.1 **Decay Factor α and Energy Shift Rate**

Using the simple rectangular function to describe the IED of the stored anthracene molecular cations, we have obtained the relation between the decay factor α and the high energy edge of the IED, as plotted in Figure 2.25 in chapter 2. In this subsection, the decay factor α is applied to describe the decay tendency of the experiment neutral yield curves at different storage times. The decrease of the decay factor α with time indicates the shift of the IED to lower energies. By comparing the decay factor α in the experiment with the calculated relation between α and E_{edge}, a rough shift rate of the IED of stored molecular ions is obtained [140].

The molecular ions in the experiments are stored up to 5 ms, laser pulses (λ = 454.7 nm, $h\nu$ = 2.73 eV) with a repetition rate of 1 kHz are sent to irradiate the stored molecular ions, the intensity of laser pulse is about 300 μJ per pulse to ensure the single photon absorption condition. Figure 4.18 presents the neutral yields with laser irradiation at different storage times 1.2, 2.2, 3.2 and 4.2 ms.

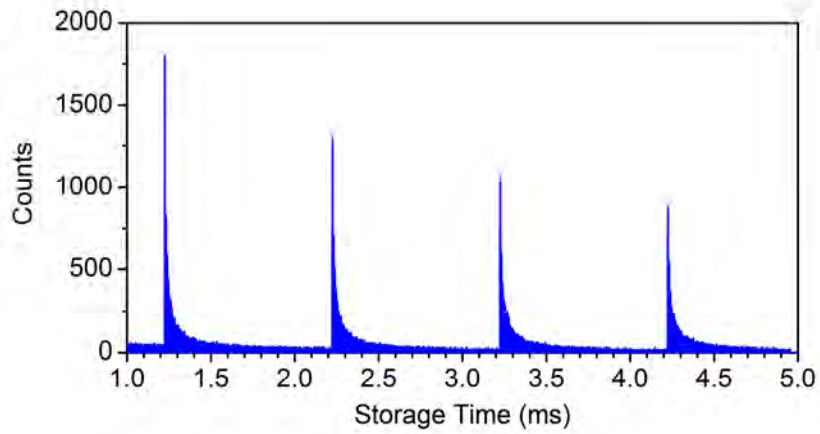

Figure 4.18 Neutral yields with laser excitation at different storage times.

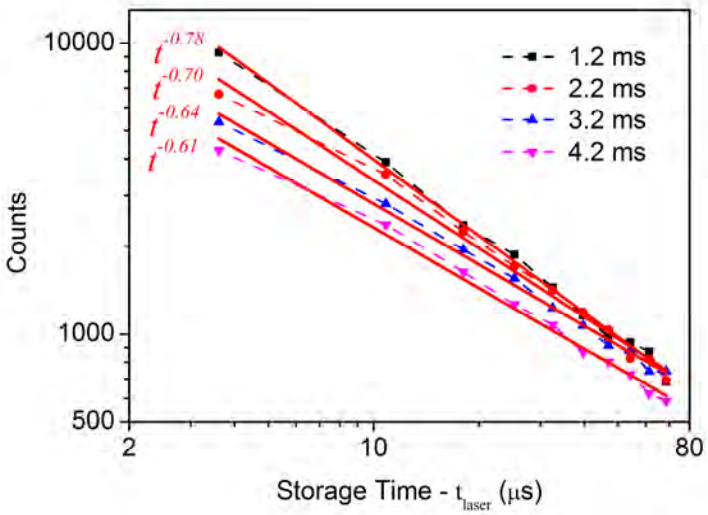

Figure 4.19 Integral of the first ten peaks after each laser pulse irradiation and the fit with $t^{-\alpha}$ law, laser firing time t_{laser} is used as time reference for the corresponding peaks.

For each laser pulse, the net laser induced neutral yield corresponding to the total neutral count recorded for each revolution period is plotted in Figure 4.19 as a function of time *t*. The reference of the time scale $t = 0$ is defined by the laser firing times t_{laser}. The four decay curves are plotted in log-log scales and fitted by $t^{-\alpha}$ law. The uncertainty of the decay factor α, Δα is about 0.02. For each neutral yield curve, the fit is only performed on the first ten peaks from t_1 = 3.25 to t_{10} = 62 μs, this time range is called the time window of Mini-Ring. By fitting the four neutral yield curves, the four decay factors at storage time from 1.2 to 4.2 ms have been obtained, as plotted in Figure 4.20 (a). The decrease of the decay factor α as a function of time is remarkable; this suggests that the decay factor is a pertinent parameter to follow the time evolution of the IED of the stored molecular ions.

By comparing the measured decay factors above with the relation between α and E_{edge} in Figure 4.20 (b), the high energy edges of the corresponding IEDs of the ion bunch after laser excitation are obtained. A clear decrease of E'_{edge} with time is observed. By subtracting the photon energy $h\nu$ = 2.73 eV, we got $E_{edge} = E'_{edge} - h\nu$ of the IED just before laser excitation, the energy distributions before and after laser excitation are plotted in Figure 4.21, and the values of the high energy edges are also presented in Table 3.

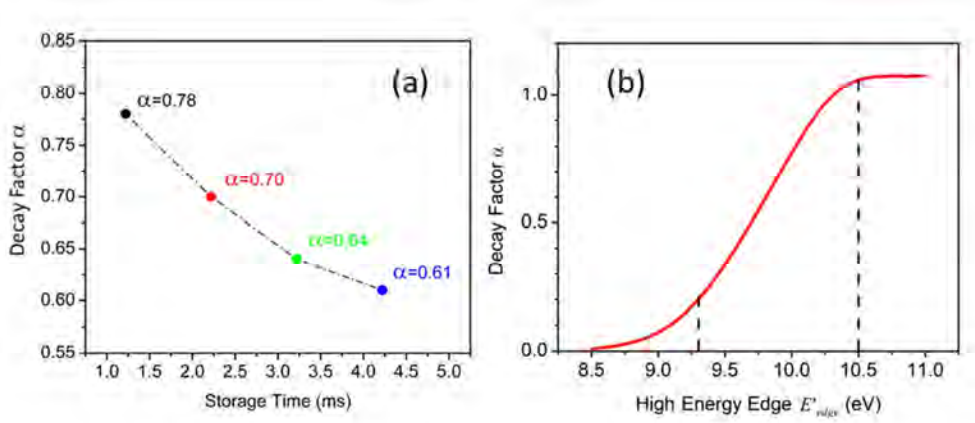

Figure 4.20 (a) Time evolution of the decay factor α. (b) α– E_{edge} relation (Figure 2.25).

Table 3 The high energy edges of the IEDs after (E'_{edge}) and before (E_{edge}) laser excitation as well as energy shift rate $\Delta E_{edge}/\Delta t$ at different storage time.

t (ms)	E'_{edge} (eV)	E_{edge} (eV)	Energy shift rate (eV s^{-1})
1.22	10.01	7.28	90
2.22	9.92	7.19	70
3.22	9.85	7.12	30
4.22	9.82	7.09	

The decrease of E_{edge} with time shows the evolution of the IED of the stored molecular ions as a function of the storage time. The high energy edge shift rate defined as $\Delta E'_{edge}/\Delta t$ decreases with storage time (Table 3). For the range of storage time considered in this work (1 < t < 4 ms), the high energy edge shift is interpreted as due to a competition between the dissociation and the radiative cooling. If the storage time is long enough when the dissociation process becomes negligible, the evolution

of the energy distribution due to the radiative cooling process then can be studied, and this work will be presented in the next section 4.3.

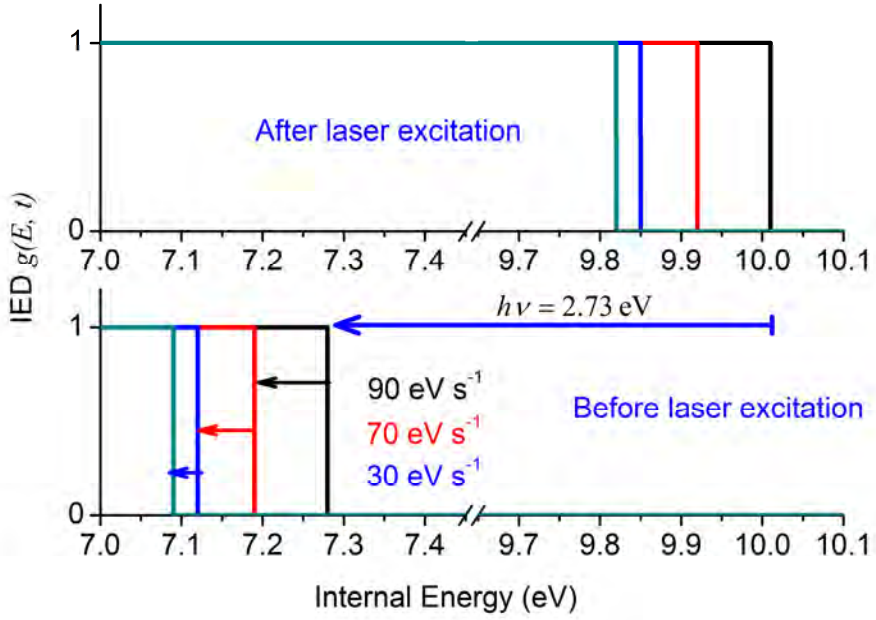

Figure 4.21 Time evolution the IEDs before and after laser excitation.

With the modeled relation between decay factor α and the high energy edge E_{edge}, the high energy edges and the energy shift rate are estimated at different storage times. The decay factor α is independent of the absolute neutral yields, which brings convenience of comparing neutral yield curves from different experiments.

4.2.2.2 **Choice of Photon Energy**

Following the discussion in subsection 2.3.5 of chapter 2, a sensitive energy window which centers at 9.6 eV with width of about 1 eV exists in Mini-Ring experiments. Any change of the molecular population inside this energy window will lead to apparent change on the neutral yield decay curves. In order to probe the IED of the molecular ions, the edges of the energy distribution, either the high energy or the low energy edge must be brought inside the energy window. Here in this thesis, only the determination of the high energy edge will be discussed, that is to say, the high energy edge of the IED must be inside the energy window after laser excitation. As illustrated in Figure 4.22, for a given IED $g(E)$, after one photon absorption, three cases can be noticed. If the high energy edge of the shifted distribution is lower than the energy window like the distribution (a), we can hardly collect the emitted neutral yields; or if the high energy edge is higher than the energy window like the

distribution (c) with homogeneous population inside the energy window, the neutral yields follows the well-known t^{-1} law which is not sensitive to the variation of the high energy edge. Only in the case (b), the high energy edge is inside the energy window, we can obtain neutral yields which are sensitive to any modification of the IED $g(E)$ of the stored molecular ions.

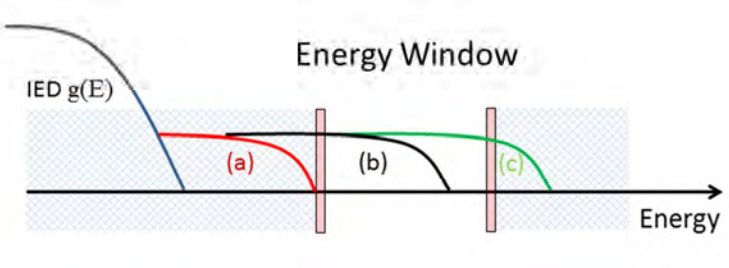

Figure 4.22 Three different shifted IEDs and the sensitive energy window.

To excite the IED of the stored molecular ions into the energy window, the type of ion source and the photon energy are the two key issues to be considered. With a hot ion source like the ECR ion source used in this work, which offers hot molecular ions with broad IED, one single photon is enough to excite the molecular ions into the sensitive energy window. If the ion source is a cold ion source like the laser ablation source, multi-photon absorption of total energy about 10 eV is necessary to excite the molecular ions, which is much more complex to draw a conclusion. As we know, the IED of the stored molecular ions shifts to lower energies as a function of the storage time, then the suitable choices of photon energy are essential to make sure that the high energy edge of the IED is inside the "narrow" energy window during the cooling experiments. For instance in the former experiment, the photon $h\nu$ = 2.73 eV is chosen to excite the molecular ions in a time range from 1 to 4 ms. When the molecular ions are stored for longer time, photons with higher energy are required.

4.2.2.3 **Neutral Yields and Time Window**

After laser excitation, the neutral yields one can collect are tightly related to the time window one can access, especially the short time limit which corresponds to the time of flight of the molecular ions from the laser excitation zone to the detection zone. This feature is typical for experiments using storage rings. Considering an ion bunch with very broad IED, the neutral yields emitted from this ion bunch tends to a t^{-1} decay law as discussed in subsection 2.3.2 of chapter 2, then the characteristic time window determines the relative neutral yields one can collect from the stored molecular ions. As illustrated in Figure 4.23, the characteristic time window of Mini-Ring can access to the very first microsecond, while using larger ESR as ELISA [64], the time window is from about 100 μs to tens of milliseconds. The relative neutral

yields one can collect in Mini-Ring are about one order of magnitude higher than that in ELISA. The ability to access to such short time range is one of the characteristics of the small size of Mini-Ring. The high collectable neutral yield insures the statistics of the experiments in short experiment performing time, which brings remarkable convenience to the experiments.

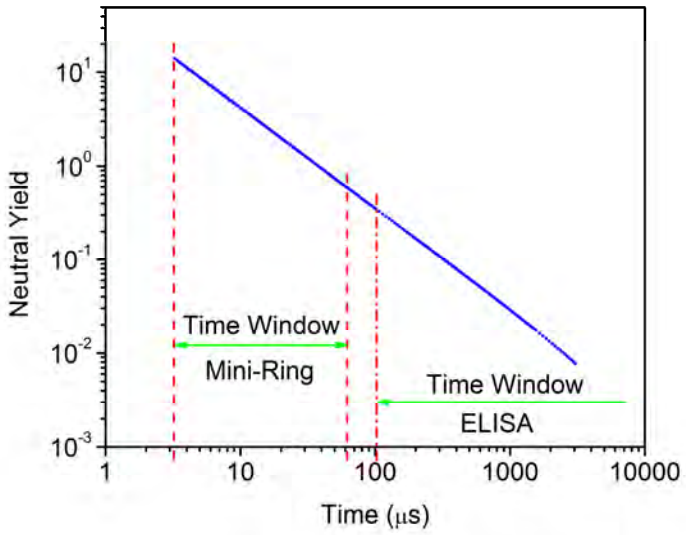

Figure 4.23 Time windows and the relative neutral yields, note the logarithmic scales.

In this subsection, a simple method to probe the time evolution of the IED of the stored molecular ions has been presented. By comparison with the neutral yield calculated from a modeled IED, the deviation of the measured neutral yield from t^{-1} behavior was related to a simple IED through an intermediate parameter, the decay factor α. By measuring the variation of α with the storage time from 1.2 to 4.2 ms, we have estimated the evolution of the IED in this time range. Furthermore, the characteristic energy window and the relative neutral yield have been discussed and compared with another ESR, ELISA, the small size of Mini-Ring brings apparent advantages in experiments.

4.2.3 Energy Shift Probed with Different Photon Wavelengths

In this subsection, laser pulses of two different photon wavelengths (454.7 nm, 2.73 eV) and (423.6 nm, 2.93 eV) were employed to excite stored anthracene cations

independently, and two series of decay factors α as function of the storage time are obtained. The shift rate of the IED then is estimated by comparing the decay factor α.

During a storage cycle 5 ms, laser pulses of photo wavelength 454.7 nm were used to irradiate the stored molecular ions at different storage times. By analyzing the laser induced neutral yield curves with the decay factor α, a series of decay factors were obtained as a function of storage time (black squares in Figure 4.24). A second series of decay factors (blue filled circle in Figure 4.24) were obtained due to the laser irradiation with photon wavelength of 423.6 nm, corresponding to a slight increase of the photon energy by 0.2 eV.

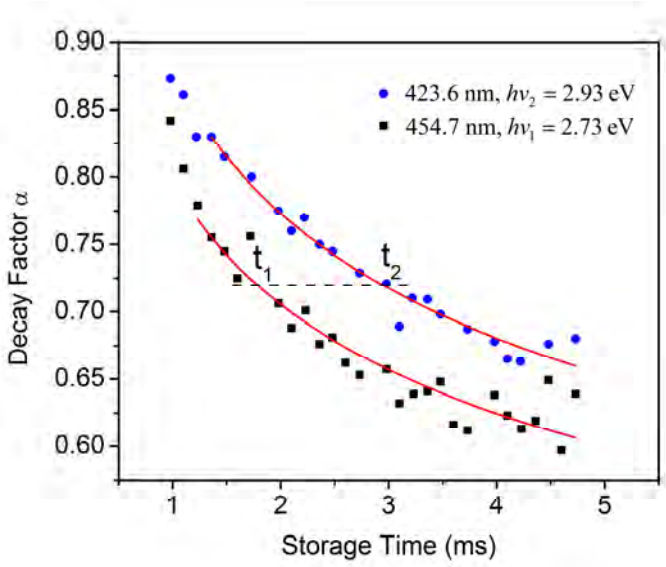

Figure 4.24 Decay factors as a function of storage time for two different wavelengths 454.7 nm (black square) and 423.6 nm (blue filled circle).

The decay factor α is related sensitively to the IED after laser excitation. Indeed, comparing two α values, the smaller one corresponds to a slower neutral yield decay which is related to an energy distribution shifted to a lower value with respect to that of the larger α value. The two series of decay factors present strong decreasing tendency with increasing storage time, indicating that the energy distribution after laser excitation shifts to lower energy region with the storage time. This behavior is in good agreement with the expected energy shift of the stored ions before laser excitation due to the cooling of the molecular ensemble. For a given α value obtained using λ_1 and λ_2, the laser firing times t_1 and t_2 were determined from Figure 4.24. The corresponding neutral yield curves present the most similar features that should be related to the most comparable IED after laser excitation. By removing the energy of the absorbed photon, respectively $h\nu_1$ and $h\nu_2$, the high energy part of the obtained IED before laser excitation at t_2 should present a shift to lower energy by about ΔE =

$h(\nu_1 - \nu_2)$ = 0.2 eV comparing to that at t_1. As an example, for α = 0.72 in Figure 4.24 (see the dash line), the storage times were found to be t_1=1.75 and t_2=3 ms. A mean internal energy shift rate $\frac{\Delta E}{\Delta t}(t)$ at a mean storage time $t_{mean} = (t_1 + t_2)/2$ was estimated,

$$\frac{\Delta E}{\Delta t}(t) = \frac{0.2\ \text{eV}}{t_2 - t_1} = 160\ \text{eV s}^{-1}$$

Equation 4-10

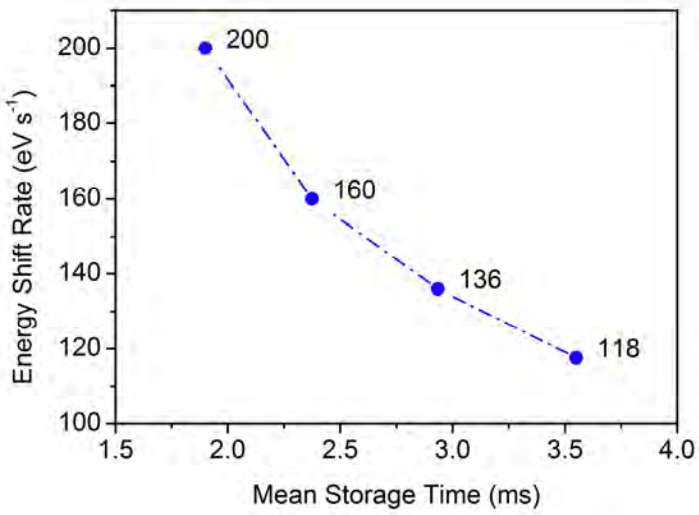

Figure 4.25 Mean energy shift rate at different storage times.

By choosing different values of decay factors α, the energy shift rate at various storage times could be estimated, as illustrated in Figure 4.25. The energy shift rate presents a monotonous decreasing trend with the storage time. According to the discussion in subsection 4.2.1, during the first millisecond of storage time, the dissociation of the stored ions is the predominant cooling process, the radiative cooling starts to compete with dissociation process at around 1 ms and inhibits the dissociation process after 3 ms. Therefore, the fast shift rate in the short time range (t < 3 ms) is attributed to both dissociation and the radiative cooling. The shift rate in the longer time range (t > 3 ms) could be attributed mainly to the radiative decay. It depends sensitively on the storage time, therefore, on the IED of the stored molecular ensemble.

The photon wavelengths chosen to irradiate the stored molecular ion bunches were 454.7 and 423.6 nm in this work, note that the choices were not unique. Any photon wavelength which may bring the excited population into the sensitive energy window can be chosen provided that it could be absorbed by anthracene cations with a

good efficiency. Therefore, the main issue that limited the choice of the photon energy was the width of sensitive energy window, about 1.2 eV.

Note that the energy shift rate we obtained here is about two times as that obtained in the paragraph 4.2.2.1. In the present method, the shift rate $\Delta E/\Delta t$ of the IED of the stored anthracene cations was estimated directly without involving any energy distribution simulation, thus it is more reliable. In the contrary, a relation between the decay factor α and the high energy edge E_{edge} of the IED was used in paragraph 4.2.2.1. As discussed in subsection 2.3.5 of chapter 2, this relation was obtained by fitting the neutral yields calculated from rectangular shaped IEDs described using only one parameter E_{edge}. This rough estimation of the IED leads to a qualitative description of the relation between α and E_{edge}, and is useful for drawing main features of experiments using storage rings. However, the disagreement of the energy shift rate measurement suggests that this simple model is not suitable for quantitative analysis. Furthermore, the fit of the neutral yield curve (either modeled one or experimental one) using only one parameter α seems not precise enough to describe the decay of the neutral yields, which may also bring uncertainties.

In the following work, multi-parameter functions will be employed to simulate the IED of the stored anthracene cations, and the modeled neutral yield curve will be compared directly with the experimental one. With this method, a more realistic estimation of IED is expected and the uncertainties due to the intermediate parameter can be avoided.

4.2.4 **Direct Fit of the Experimental Neutral Yields**

To draw the detailed picture of the IED, only one parameter like E_{edge} to describe the high energy edge is obviously not enough. In this subsection, multi-parameter functions which contain more details on the shape of the high energy part will be used to estimate the IED. The neutral yield curve calculated from the predefined multi-parameter function is fitted with the experiment neutral yield curve by adjusting the parameters, and the IED then can be redrawn by the predefined functions and the parameters after the fitting procedure.

Since we aim to determine the high energy edge of the IED, it is reasonable to define the multi-parameter functions which are broad and sensitive only at the high energy part. Three functions have been employed and compared in their reproduction ability of the experimental neutral yield, as shown in Figure 4.26:

(1) Power three function as used in earlier work Ref. [74]:

$g'(E) = N_0$, if $E < E_0$;

$g'(E) = N_0 - A(E - E_0)^3$, if $E \geq E_0$.

The parameters N_0, A and E_0 are adjustable.

(2) Square shape function as used in section 2.3 of chapter 2:

$g'(E) = N_0$, if $E < E_0$;

$g'(E) = 0$, if $E > E_0$;

N_0 and E_0 are adjustable.

(3) Half Gaussian function:

$g'(E) = N_0$, if $E < E_0$;

$g'(E) = N_0 e^{-\frac{(E-E_0)^2}{2\sigma^2}}$, if $E > E_0$;

N_0, E_0 and σ are adjustable.

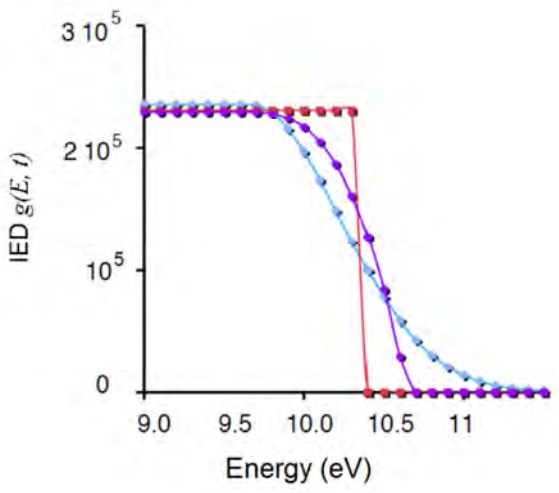

Figure 4.26 Three functions to estimate the IED, including square shape function (red square), half Gaussian function (blue diamond), power three function (violate filled cycle).

The modeled neutral yield curves are calculated by summing over the individual contributions from the whole internal energy range with Equation 2-21,

$$I(t) = \int g'(E) k_{diss}(E) e^{-k_{diss}(E)t} dE$$

The energy step is chosen as 0.1 eV to reach a good convergence. These modeled curves are used to fit one experimental neutral yield curve obtained at storage time 3 ms with laser pulse (355 nm, 3.5 eV) irradiation. As shown in Figure 4.27, it seems that all the three functions lead to nice fits with the experimental neutral yields.

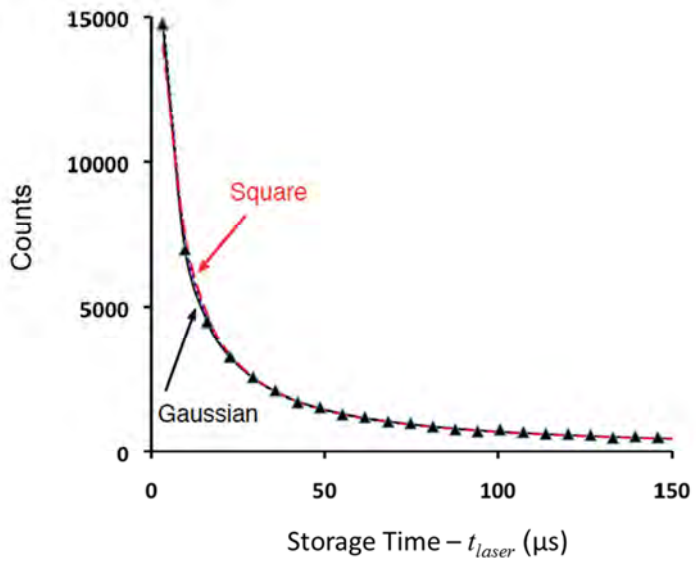

Figure 4.27 Experimental and modeled neutral yield curves. The neutral yield curves calculated from power three, square shape and half Gaussian distributions are illustrated as dashed, red broken and plain lines respectively.

In order to evaluate the reproduction ability of the three functions in detail, more attention has been paid on the small divergence between the modeled and experiment neutral yield curves. Figure 4.28 presents the relative divergence obtained from the difference between the modeled and experiment neutral yields divided by the experiment ones for the three functions. For longer time range ($40 < t < 150$ μs), the relative divergence is found close to zero for all the three functions. However, in the short time range ($t < 40$ μs), the difference among the three functions are apparent. The relative divergence is close to zero for only the half Gaussian function while large values are noticed using the square shape and power three functions. This indicates that the neutral yield curve in the short time range is more sensitive to the shape of the high energy edge of the IED. The half Gaussian function, which leads to the best fit in all time range, happens to be the best choice to estimate the IED of the molecular ion bunch.

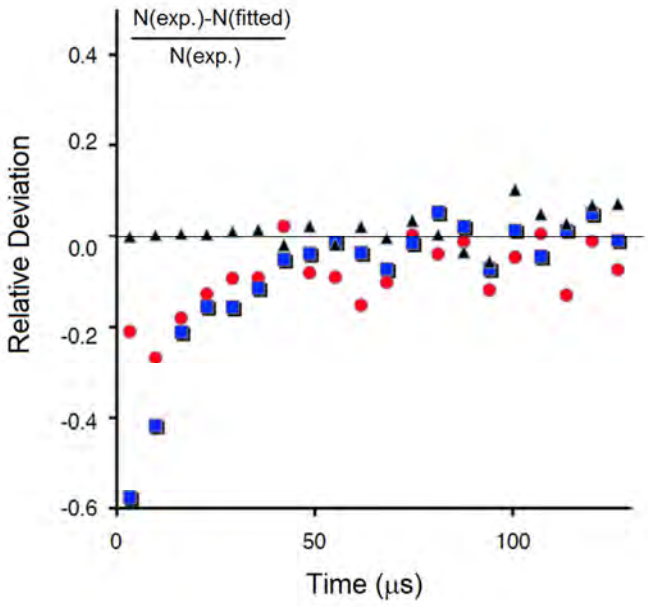

Figure 4.28 Differences between the experiment and fitted neutral yield curves as a function of time. Red filled circle, blue square and black triangle stands for the Power three, square shape and half Gaussian distributions, respectively.

In this subsection, three different functions have been used to estimate the IED of the stored molecular ions, and their abilities to reproduce the experimental neutral yield curve are compared. The half Gaussian function was found to be the best one to redraw the IED of the stored anthracene cations, which will be employed to describe the IED in the following work.

In this section, the dissociation and radiative cooling processes are found to be dominant cooling process in less than 1 ms and longer than 3 ms, respectively. The decay factor α is a convenient parameter to describe the neutral yield decay curve and draw qualitative features of the experiments. The half Gaussian function is found suitable to estimate the IED of the stored molecular ions. By fitting the experimental neutral yield curve with the modeled one calculated from half Gaussian distribution, a detailed picture of the high energy part of the IED can be obtained.

4.3 Fast Radiative Cooling

The shift of the IED in short time scale from about 1 to 4 ms is attributed to the contribution of both dissociation and radiative cooling process. To investigate the radiative cooling process, the molecular ions must be stored for long enough time. In

this section the anthracene cations are stored in the Mini-Ring up to 8 ms to access to the time range when the dissociation process is negligible. In the first subsection, with third harmonic photons irradiating the stored molecular ions at t_{laser} from 3 to 7 ms, the time evolution of the IED will be obtained by reproducing the laser induced neutral yield curves. In the second subsection, the radiative cooling rates obtained from the evolution of the IED will be discussed and compared with the predicted values.

4.3.1 **Experiment in Long Storage Time**

4.3.1.1 **Experiment with Multiple Laser Pulses**

The anthracene molecular ions are stored in Mini-Ring up to 8 ms in this experiment to access to the time range when dissociation is negligible. During each storage cycle, nanosecond laser pulses of third harmonic photons (355 nm, 3.5 eV) with repetition rate of 1 kHz are sent to merge the stored ion bunch at well-controlled storage time t_{laser} = 3, 4, 5, 6 and 7 ms. The laser pulses are unfocused with beam diameter estimated to be about 2 mm. The intensity of each laser pulse is about 2 ~ 3 mJ cm^{-2} per pulse to ensure the single photon absorption condition. In addition, the Clear of the data acquisition has been used to skip the spontaneous dissociation yields until 2.8 ms, thus the neutral yields before 2.8 ms are not recorded.

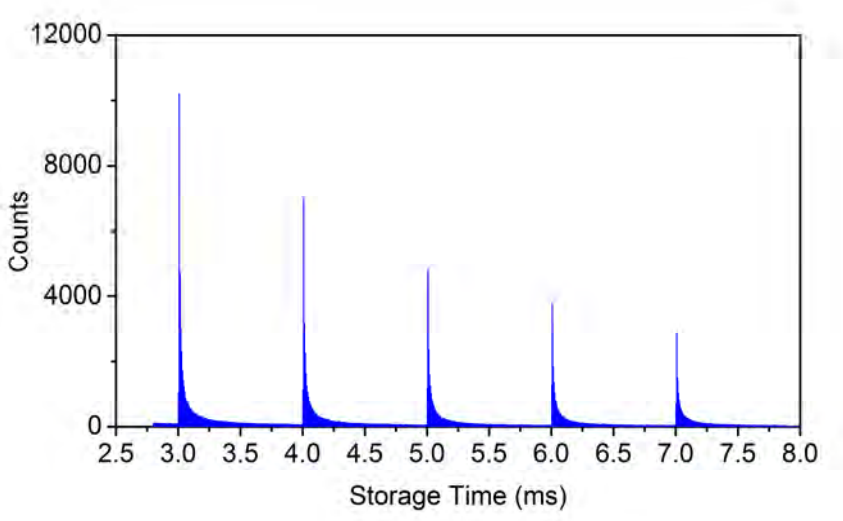

Figure 4.29 Neutral yields with laser excitation at 3, 4, 5, 6 and 7 ms.

Figure 4.29 displays the neutral yields with laser pulses firing at t_{laser} = 3, 4, 5, 6 and 7 ms. It is noticed that the brightness of the laser induced peaks is very high, which, as an outstanding feature of such small storage ring setup, brings advantages

for the analysis of the neutral yields. Furthermore, we notice that the laser induced neutral yields decrease with increasing storage time. As discussed in paragraph 4.1.2.3 in the first section of this chapter, the depleted population for each laser shoot is only about 3 ~ 4% of the total amount, this could not lead to such obvious decrease of the neutral yields. Therefore, the cooling of the internal energy of the stored ion bunch is considered to be responsible for the decrease of the neutral yields.

The zoom in of the neutral yields for $t_{laser} = 3\,\text{ms}$ is plotted in Figure 4.30 (a) and (b) to present the details. In Figure 4.30 (a), the first fifteen laser induced peaks are presented, the small peak in front of the first main peak is the noise on the MCP due to the hitting of the photons on the injection electrodes. In Figure 4.30 (b), the neutral yields are plotted in logarithmic scale, the nearly rectangular shape of the first huge peak at 3.008 ms illustrates the good space overlap condition of the laser pulse and the ion bunch, and this condition is found to be independent of the laser irradiation time t_{laser} over the total storage time. This shows that the storage of the ion bunch inside the ring is quite stable and the Betatron oscillation is considerably reduced compared to the earlier measurements when the Mini-Ring was built up [21]. The first huge peak locating in the center of the background count peak (amplitude about 100 counts) illustrates the good time overlap condition. This condition is well optimized for each laser shot to ensure that each laser pulse merges the middle of the ion bunch.

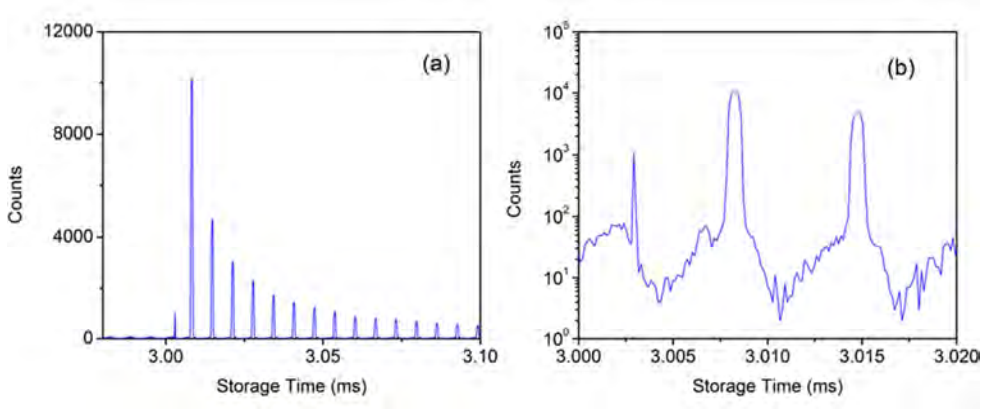

Figure 4.30 Zoom-in of the neutral yields at 3 ms. (a) Zoom in in linear scale; (b) Zoom in in log-linear scale to show the shape of the laser induced peak and the back ground counts.

The energy of the third harmonic photon (355 nm, 3.5 eV) used in this experiment is close to the electronic absorption band $^2B_{2g}$ (D_0) → $^2B_{1u}$ (D_5) around (352 nm, 3.52 eV) as discussed in subsection 2.2.3 of chapter 2. For molecular ions with high internal energy up to about 7 eV in the present case, the Franck-Condon profile is not known precisely but estimated to be broad. The absorption efficiency is observed here to be high enough for recording laser induced neutral yields with good statistics. In addition, from the technical point of view, the photon energy 3.5 eV is high enough to

bring the cooled population of the molecular ensemble into the sensitive energy window during the experiment time range 3 to 7 ms.

4.3.1.2 **Time Evolution of the IED**

Following the discussion in subsection 4.2.4, the half Gaussian function is the most suitable function to estimate the IED. By fitting the experimental neutral yield curve with the curve calculated from modeled half Gaussian function, the IED after each laser pulse excitation can be obtained. This method is used here to fit the neutral yields obtained at t_{laser} = 3, 4, 5, 6 and 7 ms.

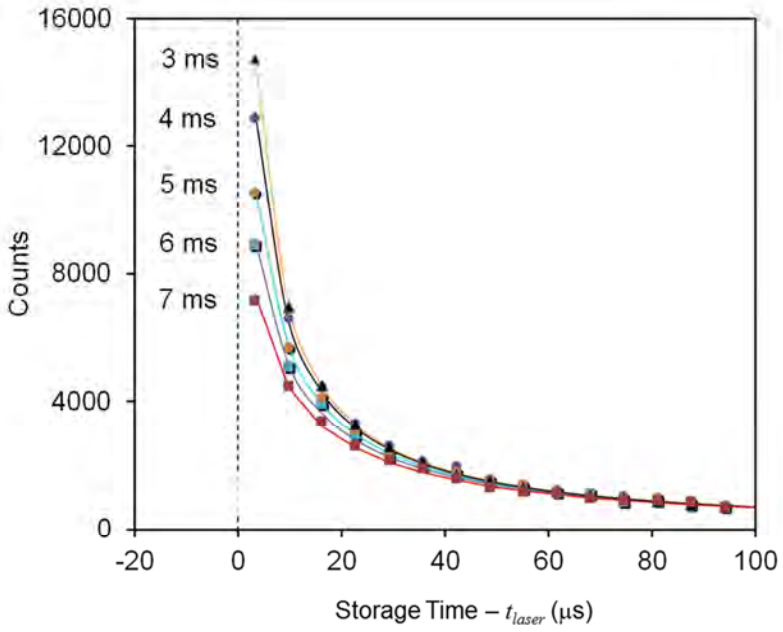

Figure 4.31 Experimental (symbols) and modeled (plain line) neutral yield curves versus laser pulse firing time t_{laser} = 3, 4, 5, 6 and 7 ms.

Figure 4.31 presents the experimental (symbols) and modeled (plain line) neutral yield curves at different storage times 3, 4, 5, 6 and 7 ms, the corresponding laser pulse firing times t_{laser} are used as time references. Due to the evolution of the stored ion bunch in the ring, the following factors have to be taken into account for the normalization of the neutral yield curves obtained at different t_{laser}, like the evolution (stretching) of the ion bunch, the depletion of the stored ions due to laser irradiation and collision with residual gas, as well as the time overlap of the laser pulse and the ion bunch.

It should be mentioned that the neutral yield curves have been fitted independently leading to very close values for N_0. It varies in a small range of less than 5%, the weak dependence of which on the storage time is tentatively interpreted as the demonstration of slight variation of the global absorption factor with the evolution of the IED. This justifies the assumption taken in this work by considering the absorption factor as independent of the internal energy around the high energy edge.

After the fitting procedures for all the above neutral yield curves, the IED after each laser excitation is obtained. Following the relation between the high energy edges before (E_{edge}) and after (E'_{edge}) laser excitation, $E'_{edge} = E_{edge} + h\nu$ (Equation 4-6), the IEDs before laser excitation at different storage time 3, 4, 5, 6 and 7 ms are obtained by subtracting the photon energy 3.5 eV from each IED, as illustrated in Figure 4.32, the N_0 has been normalized for each IED. The main feature appearing in this figure, as expected, is the evolution of the IED as a function of the storage time. The regular shift of the IED to lower energies shows that an efficient cooling process undertakes in the observed time range from 3 to 7 ms.

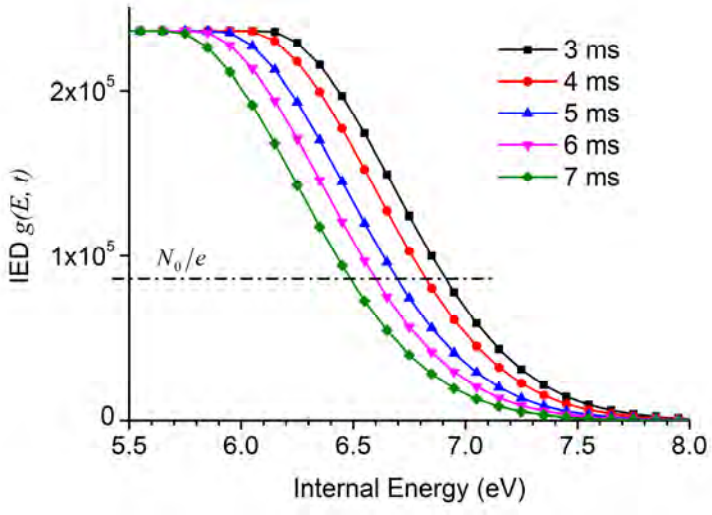

Figure 4.32 IEDs of the stored molecular ion bunch at 3, 4, 5, 6 and 7 ms of the storage time before laser excitation.

Following the definition of the high energy edge E_{edge}, $N(E_{edge}) = N_0/e$, the E_{edge} of the IED is estimated to shift globally at a rate of $\frac{\Delta E_{edge}}{\Delta t} \cong -100\,\text{eV s}^{-1}$. This value agrees well with the energy shift rates measured with different photon energies in the last section (Figure 4.25). As discussed in subsection 4.2.1, the dissociation process of the stored molecular ion bunch is quenched by the radiative cooling from 1 to 3 ms,

and becomes negligible after t > 3 ms. The shift rate of the IED also decreases down to -100 eV s^{-1} in the present time range from 3 to 7 ms. This shift rate should be attributed without ambiguity to the radiative cooling process of the stored molecular ions.

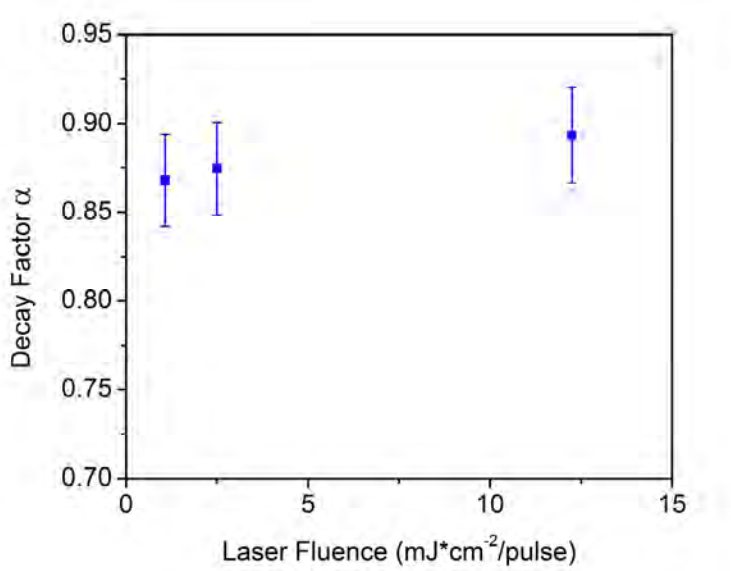

Figure 4.33 Decay factor α as a function of laser fluence at t_{laser} = 3 ms.

Although due to the sensitive energy window in this experiment, the sensitive part of the IED is only the high energy part, limited information on the low energy part still can be obtained by analyzing the decay factor α as a function of the laser fluence. In order to get such information, neutral yields at t_{laser} = 3 ms have been recorded as a function of the laser fluence, and analyzed by the decay factor α. The dependency of α on the laser fluence presented in Figure 4.33 shows a slight increasing behavior with laser increasing fluence. It is known that, by increasing the laser fluence, the two photon absorption probability will be enhanced. In the case of full Gaussian shape distribution centered around 7 eV, two photon absorption would lead to an extra Gaussian distribution centered around 14 eV. Molecular ions at such high internal energy have a very short dissociation lifetime (<< 1 μs) and dissociate during the first μs far from reaching the signal collection section D_3 - D_4. Therefore, the increase of this high energy population with the laser fluence would not induce any variation in the neutral yield curve and accordingly in the decay factor α. In the case of the half Gaussian shape with a broad extension to the low energy range, populations with initial energy around 3.5 eV might be brought to 10.5 eV via two photon absorption and modify the IED in the sensitive energy window. This could lead to variations of the neutral yield curves, the higher the laser fluence is, the higher the two photon absorption rate is, and the decay factor α has more obvious variation. From these

analyses we conclude that the full Gaussian function with the suppression of the low energy population does not give a realistic description of the IED. Although, we could not provide the exact form of the low energy part of the IED by the present work, we can say that it extends at least to about 3.5 eV.

As shown in Figure 4.29, multiple laser pulses are employed to excite the stored molecular ions with a repetition rate of 999 Hz during one storage cycle, the reheating effect may exist, for instance the last laser pulse ($t_{laser} = 7$ ms) may excite the molecular ions which already have been excited by a previous laser pulse. To evaluate the influence of reheating effect to the experiment, another experiment with only one laser pulse firing at $t_{laser} = 7$ ms during the storage has been performed. The two experiments show almost the same neutral yield curve at $t_{laser} = 7$ ms after normalization, indicating that the reheating effect in the experiment is negligible. On the other hand, as already discussed in paragraph 4.1.2.3, the depleted population due to each laser pulse is estimated to be about 3%, thus the excited population after each laser pulse is estimated to be around 6%. For such low excitation probability, it is not surprising that the reheating effect is negligible.

In this subsection, the half Gaussian function was used to estimate the IED of the stored anthracene cations. The IEDs before laser irradiation at different storage time 3, 4, 5, 6 and 7 ms have been obtained. The shift rate of the IED is estimated to be about -100 eV s^{-1}. Such fast shift rate is attributed to the radiative cooling in the studied time range.

4.3.2 **Fast Radiative Cooling**

In the above subsection, the global energy shift of the IED of stored anthracene cations has been studied as a function of the storage time. In this subsection, the evolution of the ion population for a given energy will be studied as a function of the storage time. The measured population decay rate will be compared with the population decay rate resulting from IR emission, and electronic fluorescence emission. The fluorescence cooling rate due to electronic fluorescence emission will be compared with the work of Boissel et al.

4.3.2.1 **Measured Population Decay Rate**

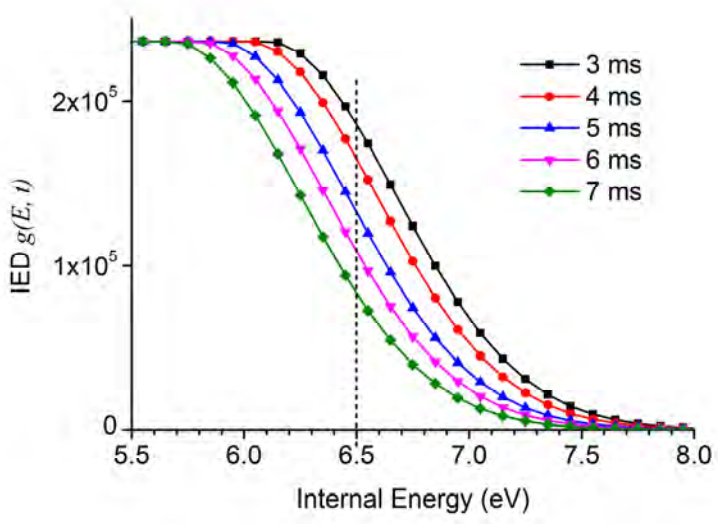

Figure 4.34 IEDs of the stored anthracene cations from 3 to 7 ms.

From the observed IEDs from 3 to 7 ms, it is possible to extract population decay rates for a given internal energy E as a function of the storage time. As an example, a vertical line at energy 6.5 eV is drawn crossing all energy distribution curves $g(E,t)$ at different storage time, as illustrated in Figure 4.34. By plotting the populations at the crossing points as a function of the storage time, we see clearly a time dependent population decay behavior for molecular ions with internal energy 6.5 eV.

With a step of 0.2 eV, the analysis of population decay as a function of the storage time has been repeated for E varying from 6 to 7.4 eV, the extracted populations for different energy E are plotted in Figure 4.35 in logarithmic scale. For each internal energy E, the population decay curve could be well fitted by the exponential function. The fitting exponent, i.e. the characteristic constant $k_{measured}$ for each internal energy E is defined by,

$$k_{measured} = -\frac{1}{g(E)}\frac{dg(E)}{dt}$$

Equation 4-11

The $k_{measured}$ values are presented in Table 4. These rates are expected to result from the sum of the contributions of all possible cooling and depletion mechanisms for molecular ions with internal energy E, i.e., mainly the dissociation process characterized by $k_{diss}(E)$ and the radiative emission process. The dissociation rates of neutral emission were discussed already in chapter 2 (Figure 2.5) and given in the table as a function of internal energy. In the interested energy range E < 7.5 eV,

$k_{diss}(E)$ is much smaller than $k_{measured}$, so the contribution of the dissociation process can be considered to be negligible. This is in agreement with our statement in subsection 4.2.1 that the dissociation process at storage time longer than 3 ms is negligible. The observed population decay is therefore attributed predominantly to the radiative cooling. The measured decay rates were found to be varying from 25 to 450 s^{-1} in the energy range from 6 to 7.4 eV. These values are in good agreement with our estimations in an earlier work [74].

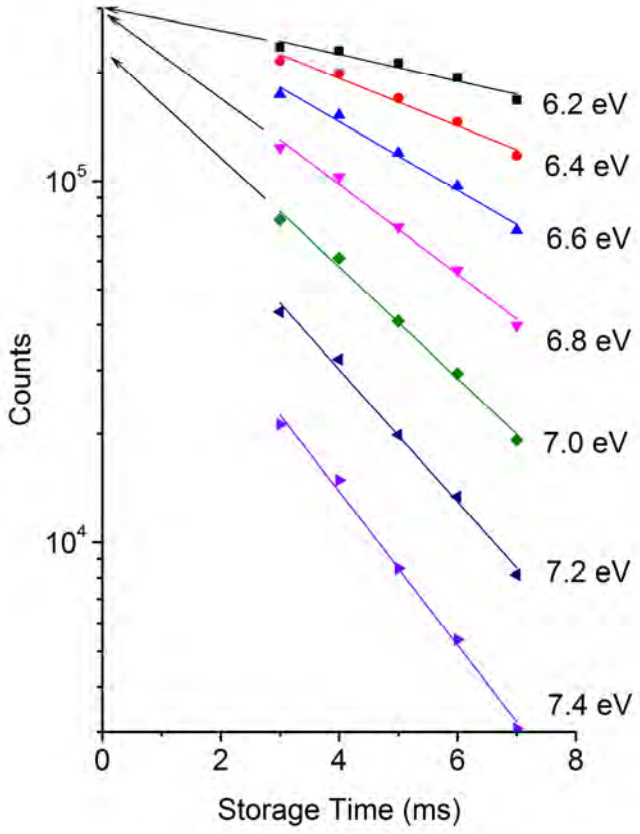

Figure 4.35 Evolution of the molecule population versus storage time at different internal energies from 6.2 to 7.4 eV. For each internal energy, the population decrease is fitted with the exponential law. Arrows indicate the estimation of the initial population at storage time t = 0, extrapolations of the high energy curves are not as precise as the low energy curves.

Table 4 Measured population decay rate $k_{measured}$ and calculated dissociation rate k_{diss} as a function of the internal energy E before laser excitation.

Internal Energy E (eV)	k_{diss} (s^{-1}) [113]	$k_{measured}$ (s^{-1})
7.8	69	

7.6	33	
7.4	15	450
7.2	7	386
7.0	3	324
6.8	1	262
6.6	0.38	198
6.4	0.13	133
6.2	0.04	85
6.0	0.01	25

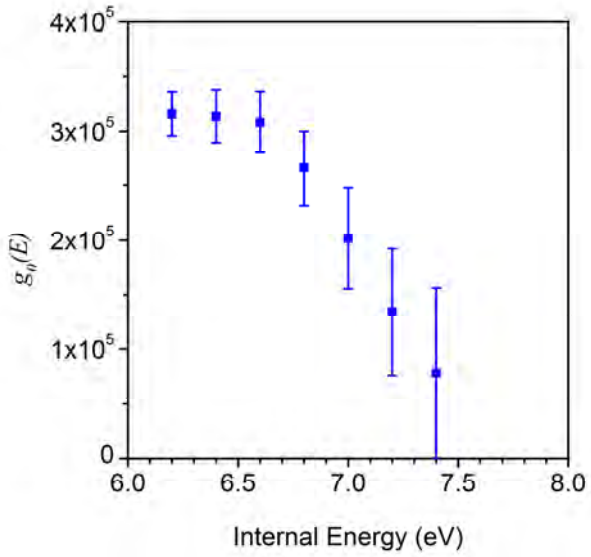

Figure 4.36 Estimation of $g_0(E)$ proportional to the initial IED profile in the ECR ion source from 6 to 7.4 eV.

In Figure 4.35, for each E value, the fitted exponential function is extrapolated to storage time t = 0, leading to the initial IED $g(E,0)$. The population found at t = 0 are presented in Figure 4.36 as a function of internal energy E. As we see, for $6 < E < 6.8$ eV, the extrapolated populations are quite comparable to the value N_0, constant values at the low energy part of the fitted IEDs (Figure 4.32). This suggests that the initial IED of the ion bunch formed in the ECR ion source is roughly independent of the internal energy at least in this energy range. For $E > 7$ eV, the extrapolated populations exhibit a decreasing tendency with increasing energy showing a limited width of the initial IED which is an expected behavior of the IED from an ECR ion source. However, the error bars in this high energy range are very

large because the corresponding population decay curves were obtained from the low yields, high energy tail of the IEDs (Figure 4.34). To get a more precise description of the high energy part of the IED, it would be necessary to probe the IED at shorter storage times.

4.3.2.2 **IR Emission**

From the above work, the population decay rate has been obtained as a function of the internal energy, which increases from 25 to 450 s^{-1} for internal energy varying from 6 to 7.4 eV. The radiative cooling, as introduced in section 2.1 of chapter 2, has been investigated theoretically by Boissel et al [88] including the contributions from both IR emission and fluorescence emission. In this paragraph and the next one, both mechanisms will be discussed individually to evaluate their relative importance in the measured population decay rate and in global radiative cooling of the anthracene molecular ions.

The IR emission of PAH molecules, as discussed in subsection 2.1.3 of chapter 2, was described using a statistical model. To follow the IR emission, it is more convenient to follow the time evolution of the internal energy $E(t)$ of an ensemble of molecules at the same initial internal energy, and from Equation 2-12 we know that $E(t)$ decreases with the characteristic cooling rate η_{IR},

$$\frac{dE}{dt} = -\eta_{IR} E$$

Equation 4-12

The IR cooling rate of anthracene cation η_{IR}, was about 2 s^{-1} and nearly energy-independent in a wide energy range from 2 to 10 eV. According to this model, the internal energy *E* for each molecule of one molecular ensemble shifts to lower values following an exponential law with a constant η_{IR}. Without other cooling mechanism, the IR emission would indeed lead to an energy shift of the high energy edge of the IED. In the energy region around 6.5 eV in the present work, the high energy edge was estimated to shift at a rate of $\left[\frac{\Delta E}{\Delta t}\right]_{IR} = -\eta_{IR} \times E \cong -13\,\text{eV}\,\text{s}^{-1}$. The absolute value of $\left[\frac{\Delta E}{\Delta t}\right]_{IR}$ is much smaller than the above measured energy shift rate 100 eV s^{-1}, suggesting that the IR emission can be considered as a minor effect in the radiative cooling.

The comparison between the measured population decay rate $k_{measured}$ and the population decay rate due to IR emission is not straightforward. Due to the fact that the IR emission energies, typically 0.2 eV are much smaller than the studied energy window 1.2 eV, when considering the variation of $g(E)$ at given *E*, one should take into account not only the decrease of the population $g(E)$ due to IR emission of molecules at the energy *E* but also the increase of $g(E)$ due to the IR emission from molecules at neighboring higher energies. Therefore, in the following an apparent IR population decay rate k_{IR}^{pop} is defined, which is tightly related to the profile of IED, particularly the derivative of $g(E)$ with respect to *E*, $\frac{dg(E)}{dE}$. In the energy region where $g(E)$ is constant, $\frac{dg(E)}{dE}=0$, the increased population compensates the decreased population, then $k_{IR}^{pop}=0$, and no population decay can be observed. In a $g(E)$ increasing region, for example the low energy edge of the IED, $\frac{dg(E)}{dE}>0$, the increased population is larger than the decreased population, then $k_{IR}^{pop}<0$, the IR emission should lead to a population gain. At around the high energy edge of the IED, $\frac{dg(E)}{dE}<0$, the increased population is smaller than the decreased population, then $k_{IR}^{pop}>0$, the IR emission should lead to a population decrease. The last case corresponds to the present work where only the high energy edge of the IED is inside the sensitive energy window.

Considering a molecular ensemble at the same initial energy *E*, the apparent IR population decay rate k_{IR}^{pop} is related to the time evolution of the energy *E* following Equation 4-12. The ion population $g(E,t)\Delta E$ at energy *E* can be approximately considered to vary with time through the energy $E(t)$, given by $g(E(t))\Delta E$, where ΔE is an infinitesimal energy interval to get the population at energy *E*. For the high energy edge of the IED, the global shift to lower energies due to IR emission leads to the decrease of the population at given energy value *E*. Then, the population decay rate k_{IR}^{pop} can be estimated as,

$$k_{IR}^{pop}=-\frac{1}{g(E(t))}\frac{dg(E(t))}{dt}=-\frac{1}{g}\frac{dg}{dE}\frac{dE}{dt}$$

Equation 4-13

In this equation, $\frac{dg}{dE}$ can be calculated using the Gaussian function $g(E) = N_0 e^{-\frac{(E-E_0)^2}{2\sigma^2}}$, and $\frac{dE}{dt}$ can be obtained from Equation 4-12, then k_{IR}^{pop} is given by,

$$k_{IR}^{pop} = \frac{(E - E_0)E}{\sigma^2}\eta_{IR}$$

Equation 4-14

To estimate the k_{IR}^{pop}, we have used η_{IR} = 2 s^{-1}, the average value of E_0 (5.9 eV) and σ = 0.57 of the five half Gaussian IEDs before laser excitation. The calculated values of k_{IR}^{pop} as a function of energy E are presented in Table 5. The measured population decay rate $k_{measured}$ is also presented in the table for comparison. The numerical values show that at a given internal energy E, k_{IR}^{pop} corresponds to about 10% ~ 15% of $k_{measured}$, which is in agreement with the discussion above that the IR emission is a minor process.

Table 5 Comparison of the calculated population decay rate due to IR emission k_{IR}^{pop} and measured rate $k_{measured}$.

Internal Energy E (eV)	k_{IR}^{pop} (s^{-1})	$k_{measured}$ (s^{-1})
7.4	57	450
7.2	48	386
7.0	40	324
6.8	32	262
6.6	24	198
6.4	16	133
6.2	8	85
6.0	4	25

4.3.2.3 **Fluorescence Emission**

For fluorescence emissions, due to the large energy jump in the electronic transitions, it is appropriate to follow the time evolution of the ion population $g(E,t)\Delta E$ at a given energy E in an infinitesimal energy interval ΔE. The ion population $g(E,t)\Delta E$ is characterized theoretically by the electronic transition rate,

$k_{elec}(E)$. Following the work of Boissel et al (subsection 2.1.4 of chapter 2), the contribution of the higher ($j \geq 3$) electronic excited states to the total fluorescence emission rate is less than 1%, thus the fluorescence emission from higher ($j \geq 3$) excited states are neglected here. In addition, the energies of the first two electronic excited states are very close ($E_{elec,1}$ = 1.71 eV, $E_{elec,2}$ = 1.88 eV), thus they can be considered as one state $E_{elec,1}$, the electronic transition rate $k_{elec}(E)$ then stands for the total transition rates from the two states. The fluorescence emission leads to a sudden reduction of the internal energy from E to $E - E_{elec,1}$ in a single step, therefore the ion population $g(E,t)\Delta E$ would decrease at energy E and increase at lower energy $E - E_{elec,1}$. Similarly, the fluorescence emission from molecules at higher energy $E + E_{elec,1}$ should lead to the increase of $g(E,t)\Delta E$ at E. The time evolution of the population $g(E,t)\Delta E$ at the energy E is then governed by the following equation,

$$\frac{dg(E,t)}{dt} = -k_{elec}(E)g(E,t) + k_{elec}(E + E_{elec,1})g(E + E_{elec,1}, t)$$

Equation 4-15

Nevertheless, it should be noted that for energy E at the high energy edge of the IED around 6.5 eV, the value $E + E_{elec,1}$ is about 8.2 eV. At such high internal energy, the initial ion population is very low, as shown in Figure 4.36. Thus the positive term in the above equation is negligible, we have

$$\frac{dg(E,t)}{dt} \approx -k_{elec}(E)g(E,t)$$

Equation 4-16

According to the above discussion, both IR and fluorescence emissions could lead to population decay at the high energy edge of the IED. Taking into account of the Equation 4-13 and Equation 4-16, the total population decay rate is considered as due to the sum of the IR population decay rate k_{IR}^{pop} and the fluorescence emission rate, k_{elec}.

$$\frac{dN(E,t)}{dt} \approx -(k_{elec} + k_{IR}^{pop})g(E,t)$$

Equation 4-17

This total population decay rate $k_{elec} + k_{IR}^{pop}$ corresponds in fact to the measured population decay rate, $k_{measured}$ (Equation 4-11). In order to extract the measured

fluorescence emission rate from $k_{measured}$, we need to subtract the contribution of IR emission, the obtained values are presented in Table 6, noted as $k_{measured} - k_{IR}^{pop}$. The theoretical electronic transition rates k_{elec} were calculated from Equation 2-13 following the work of Boissel et al [88], and then fitted with the measured value $k_{measured} - k_{IR}^{pop}$. The best fit was obtained using a value of 1.66 eV for the first electronic state $E_{elec,1}$. The theoretical electronic transition rates k_{elec} are presented in Table 6, both the theoretical and measured values are plotted in Figure 4.37.

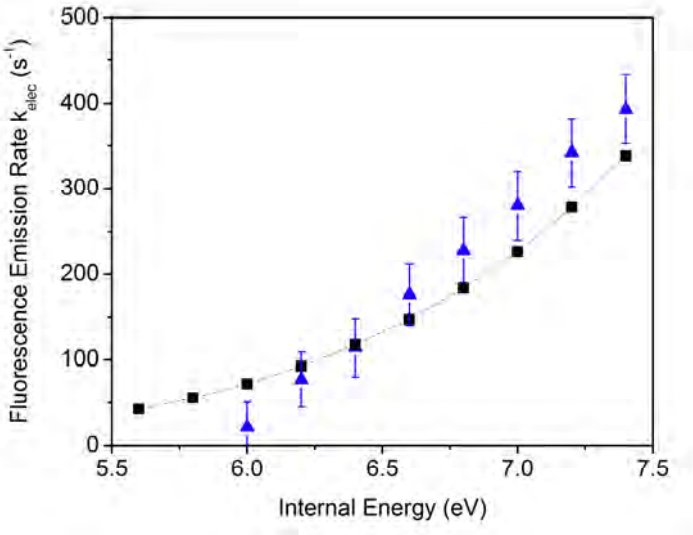

Figure 4.37 Measured fluorescence emission rate $k_{measured} - k_{IR}^{pop}$ (triangle) and the fitted theoretical one k_{elec} (square) as a function of the internal energy.

Table 6 Measured fluorescence emission rate $k_{measured} - k_{IR}^{pop}$ and the theoretical electronic transition rate k_{elec}.

Internal Energy E (eV)	$k_{measured} - k_{IR}^{pop}$ (s^{-1})	k_{elec} (s^{-1})
7.4	393	322
7.2	338	264
7.0	284	215
6.8	230	174
6.6	174	139
6.4	117	111

6.2	77	87
6.0	21	68

To compare with the dissociation rate, the measured and theoretical fluorescence emission rates are plotted together with dissociation rate as a function of internal energy, as shown in Figure 4.38. The crossing of k_{elec} and k_{diss} curves at around 8.5 eV confirms that the molecules with internal energy higher than 8.5 eV would prefer to dissociate, and the molecules in the present studied energy range is predominantly cooled down by fluorescence emission.

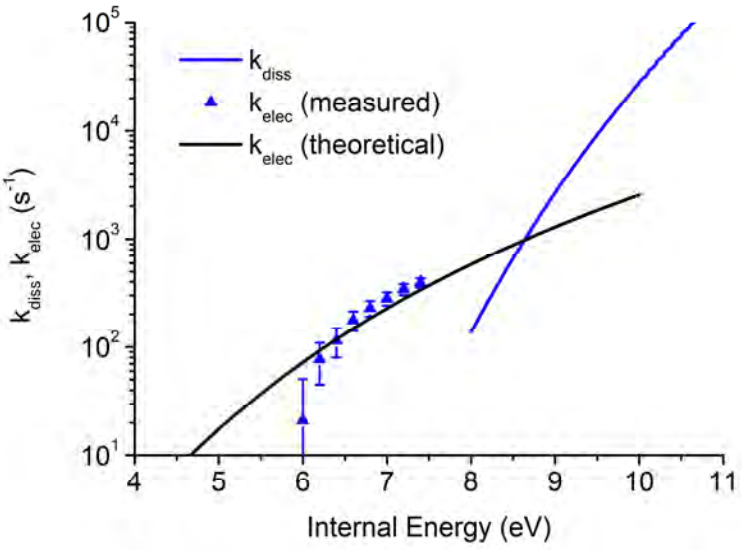

Figure 4.38 Comparison of the dissociation rate k_{diss} (blue curve), the measured (blue triangle) and theoretical (black curve) fluorescence emission rate k_{elec}.

In the present work, the first electronic state $E_{elec,1}$ is fitted to be 1.66 eV, which is about 0.1 eV smaller than the experimental value (1.75 eV) measured by cavity ring-down absorption spectroscopy by Sukhorukov et al [141]. However, the fitted value is very close to the calculation of Sanchez-Carrera et al [142] using B3LYP (1.68 eV) but still smaller than the value (1.71 eV) used by Boissel et al. This smaller value leads to the increase of k_{elec} about 30% comparing to the values obtained by Boissel et al. It shows that the fluorescence emission via electronic transition is very sensitive to the energy level of the first available electronic state, the lower the electronic energy level, the higher the emission rate.

4.3.2.4 **Fluorescence Cooling Rate**

To estimate the contribution of fluorescence emission to the cooling of a molecular ensemble with initial energy *E*, one should consider both the fluorescence emission rates and the energies carried out by the emitted photons. As discussed in subsection 2.1.4 of chapter 2, it is still informative and meaningful to proceed in an analog way as IR emission by defining a variation rate $\left[\frac{dE}{dt}\right]_{elec}$ of the average energy per molecule beside the mean fluorescence cooling rate η_{elec},

$$\eta_{elec} = \frac{1}{E}\left[\frac{dE}{dt}\right]_{elec}$$

$$\left[\frac{dE}{dt}\right]_{elec} \approx h\nu_{elec,1}k_{elec} = E_{elec,1}k_{elec}$$

Equation 4-18

Similarly to IR emission process, the average energy variation rate $\left[\frac{dE}{dt}\right]_{elec}$ corresponds to the ratio of the total power emitted via electronic transitions and the number of molecular ions in the studied molecular ion ensemble. The mean fluorescence cooling rate can be written as,

$$\eta_{elec} \approx \frac{1}{E}E_{elec,1}k_{elec}$$

Equation 4-19

Thus, the experimental fluorescence cooling rate $\eta_{elec}^{measured}$ can be calculated with Equation 4-19 using the measured population decay rate after the correction of IR emission ($k_{measured} - k_{IR}^{pop}$ in Table 6). It varies from 6 to 89 s^{-1} for internal energy varying from 6 to 7.4 eV. The theoretical value is also calculated with Equation 4-19 using the theoretical electronic transition rate k_{elec}, both the experimental and theoretical cooling rates are presented in Table 7 as well as in Figure 4.39. In addition, the total cooling rate and IR cooling rate calculated by Boissel et al are also plotted in the figure as reference.

Table 7 Measured fluorescence cooling rate $\eta_{elec}^{measured}$ and the theoretical one η_{elec} as a function of internal energy.

Internal Energy *E* (eV)	$\eta_{elec}^{measured}$ (s^{-1})	η_{elec} (s^{-1})

7.4	89	73
7.2	79	61
7.0	67	51
6.8	55	43
6.6	45	35
6.4	30	29
6.2	21	23
6.0	6	19

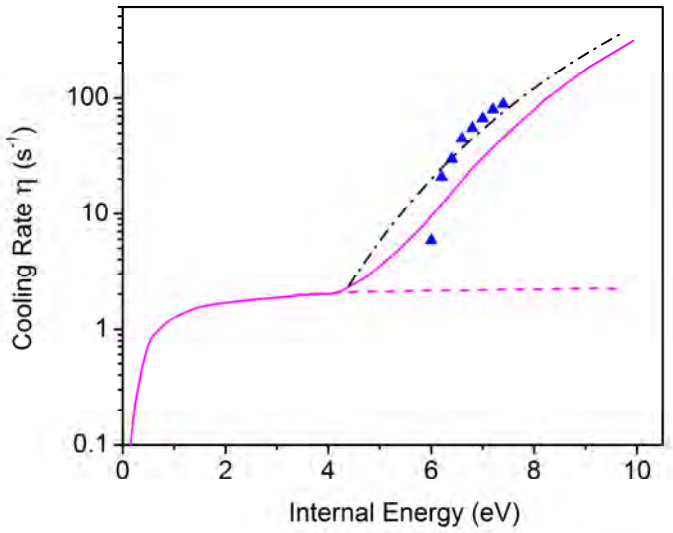

Figure 4.39 Radiative cooling rate of anthracene cation as a function of its internal energy. The pink lines (dash: infrared emission cooling rate; solid: total radiative cooling rate) are from Ref. [88]. Black dash dot line: theoretical fluorescence cooling rate. Blue triangle: measured fluorescence cooling rate in this work.

As noticed, apart from the first measured point, the experimental and theoretical cooling rates obtained in the present work are larger than that in the work of Boissel et al. Furthermore, these measured and theoretical values are much larger than the theoretical IR cooling rate η_{IR} (2 s^{-1}) calculated in this energy region. Therefore in our investigated energy range, the fluorescence emission of anthracene cation via electronic transition is found to be a more efficient radiative cooling channel. This is not only due to the increase of the fluorescence emission rate k_{elec} with internal energy, but also due to the large quantity of energy carried out by the emitted photon.

In conclusion, we have estimated the fluorescence emission rate via electronic transitions k_{elec} of anthracene cation with internal energy from 6 to 7.4 eV. In the studied energy range, k_{elec} has been found varying very fast from 20 to 400 s^{-1}. The corresponding fluorescence cooling rates η_{elec} were estimated and compared with the work of Boissel. We find that for $E > 5$ eV the fluorescence emission is the dominant radiative cooling channel. In spite of the statistically very low probability of presence in electronic excited states, the relatively high fluorescence cooling rate is explained by the high spontaneous transition rate of the involved states and the large quantity of energy carried by a single photon.

According to the calculations, the fluorescence emission is found to be very sensitive to the energy level of the first electronic excited state. Therefore, we may deduce that the fluorescence emission depends strongly on the charge and size of the PAH molecule. This effect has been confirmed recently by a study on the cooling of C_6^- and C_6H^- [71], the very different radiative cooling rates measured for the two cations were correlated to their different electronic structures, especially different energies for their first excited states.

Conclusion

In this chapter, the time evolution of the IED of the stored anthracene cations in Mini-Ring has been probed by laser excitation to investigate their cooling dynamics. The reality processes as well as the condition of the experiment have been described in detail, and the characteristics of Mini-Ring experiment has also been discussed, like the time window and energy window. The fast radiative cooling process of the PAH molecules, i.e. the fluorescence emission via electronic transition predicted by Boissel et al has been proved experimentally in this work.

Chapter 5 Summary and Perspectives

The Mini-Ring originated from the ConeTrap is a “tabletop” ESR with circumference of only 0.73 m. It consists of two conical electrostatic mirrors, and four pairs of electrostatic deflectors with six straight sections. The Mini-Ring combines the advantages of both ESRs and EIBTs. Similarly as the experiments in larger ESRs, the stored ions can be injected and excited along one of the straight sections by laser pulse, the neutral fragments emitted at another straight section can be detected as a function of time. Owing to its compact design and short ion revolution period, the laser induced dissociation in Mini-Ring can be investigated from the very first microseconds. The ability to access to such short time range allows one to measure the neutral yields with high statistics. Therefore, Mini-Ring is well adapted for the study of the cooling regimes of the PAH molecules.

The relaxation dynamics of a PAH molecule, the anthracene cation, has been studied in Mini-Ring up to 8 ms in this thesis work. An ECR ion source was employed to produce the anthracene cations with broad IED, and the cooling of anthracene cation has been probed with well-controlled laser pulses. The decay profile of the laser induced neutral yield curve contains the information of the IED of stored ions. The decay factor α is a convenient parameter to describe the decay profile of the neutral yields. Therefore the α is tightly related to the IED of the stored ions, leading to the determination of the shift of IED with α. The shift rate of IED of stored anthracene cations was estimated to decrease from 200 to 100 eV s^{-1} from about 2 to 5 ms. The energy shift at different time ranges was attributed to different cooling processes, i.e., in the first 1 ms due to the depletion of hot molecular ions by dissociation process and after 3 ms the radiative cooling process, while between 1 and 3 ms the competition between the two processes. The sensitive energy window of the Mini-Ring experiment, referring to an energy region inside which the change of molecular population leads to

obvious variation of neutral yields, is determined to center at 9.6 eV with 1.2 eV in width for anthracene cations.

The radiative cooling of anthracene cation has been studied as a function of internal energy from 6 to 7.4 eV by following the evolution of the IED from 3 to 7 ms. The fluorescence emission rate which corresponds to the electronic transition rate ($D_2 \rightarrow D_0$) of anthracene cation, has been measured to vary from about 20 to 400 s^{-1} in the studied energy range. The corresponding fluorescence cooling rate has been estimated to be about 10 to 90 s^{-1} and compared with the IR cooling rate 2 s^{-1}. This relatively high cooling rate is explained by the high spontaneous transition rate and the large quantity of energy carried by the emitted photon. Thus the fluorescence emission is the dominant radiative cooling mechanism at internal energy higher than 5 eV.

The experimental methods used to study the cooling regimes of anthracene cation can be applied to study other PAH molecules and the molecules of biological interests with different charge states. Preliminary experiments on naphthalene, pyrene, and coronene cations have already been performed, the analysis of these experiments are in process. Whether the enhancement or absence of fast fluorescence emission being observed on the other PAH molecules, the results may have important consequences for the estimation of the presences of PAH molecules in the ISM.

Besides the indirect measurements of radiative cooling via analyzing the laser induced neutral yields as a function of storage time, the direct measurement of the radiative cooling of a molecule/cluster can also be performed with the optical spectroscopy method. For instance, with the knowledge of the electronic excited states, a wavelength selective filter associated with a photomultiplier can be used directly to observe the emitted photons due to fluorescence emission as a function of time. In order to have complete data of the radiative cooling of a molecule/cluster, a spectrometer with a wide wavelength range can be employed to scan the emitted photons as a function of the wavelength to observe the photons emitted from different electronic excited states. Then by selecting certain wavelength, the emitted photons at each wavelength can be observed as a function of time.

References

[1] C. Joblin and A. G. G. M. Tielens, *PAHs and the Universe: A Symposium to Celebrate the 25th Anniversary of the PAH Hypothesis* (2011).

[2] L. H. Andersen, O. Heber, and D. Zajfman, J Phys B Mol Opt Phys **37**, R57 (2004).

[3] F. C. Gillett, W. J. Forrest, and K. M. Merrill, Astrophys. J. **183**, 87 (1973).

[4] S. P. Willner, R. C. Puetter, R. W. Russell, and B. T. Soifer, Astrophys. Space Sci. **65**, 95 (1979).

[5] W. W. Duley and D. A. Williams, Mon. Not. R. Astron. Soc. **196**, 269 (1981).

[6] A. Leger and J. L. Puget, Astron. Astrophys. **137**, L5 (1984).

[7] L. J. Allamandola, A. G. G. M. Tielens, and J. R. Barker, Astrophys. J. Lett. **290**, L25 (1985).

[8] H. Piest, G. von Helden, and G. Meijer, Astrophys. J. Lett. **520**, L75 (1999).

[9] D. M. Hudgins and L. J. Allamandola, J. Phys. Chem. **99**, 8978 (1995).

[10] H. S. Kim, D. R. Wagner, and R. J. Saykally, Phys. Rev. Lett. **86**, 5691 (2001).

[11] J. Oomens, B. G. Sartakov, A. G. G. M. Tielens, G. Meijer, and G. von Helden, Astrophys. J. Lett. **560**, L99 (2001).

[12] J. Oomens, A. G. G. M. Tielens, B. G. Sartakov, G. von Helden, and G. Meijer, Astrophys. J. **591**, 968 (2003).

[13] L. J. Allamandola, D. M. Hudgins, and S. A. Sandford, Astrophys. J. Lett. **511**, L115 (1999).

[14] A. Omont, Astron. Astrophys. **164**, 159 (1986).

[15] A. G. G. M. Tielens, Annu. Rev. Astron. Astrophys. **46**, 289 (2008).

[16] F. Salama, E. L. Bakes, L. J. Allamandola, and A. G. Tielens, Astrophys. J. **458**, 621 (1996).

[17] H. W. Jochims, E. Ruhl, H. Baumgartel, S. Tobita, and S. Leach, Astrophys. J. **420**, 307 (1994).

[18] C. Joblin, P. Boissel, and P. de Parseval, Planet. Space Sci. **45**, 1539 (1997).

[19] M. P. Bernstein, S. A. Sandford, L. J. Allamandola, J. S. Gillette, S. J. Clemett, and R. N. Zare, Science **283**, 1135 (1999).

[20] S. P. Moller, Nucl Instrum Methods Phys Res Sect A **394**, 281 (1997).

[21] J. Bernard, G. Montagne, R. Brédy, B. Terpend-Ordacière, A. Bourgey, M. Kerleroux, L. Chen, H. T. Schmidt, H. Cederquist, and S. Martin, Rev. Sci. Instrum. **79**, 075109 (2008).

[22] R. D. Thomas, H. T. Schmidt, G. Andler, M. Björkhage, M. Blom, L. Brännholm, E. Bäckström, H. Danared, S. Das, N. Haag, P. Halldén, F. Hellberg, A. I. S. Holm, H. a. B. Johansson, A. Källberg, G. Källersjö, M. Larsson, S. Leontein, L. Liljeby, P. Löfgren, B. Malm, S. Mannervik, M. Masuda, D. Misra, A. Orbán, A. Paál, P. Reinhed, K.-G. Rensfelt, S. Rosén, K. Schmidt, F. Seitz, A. Simonsson, J. Weimer, H. Zettergren, and H. Cederquist, Rev. Sci. Instrum. **82**, 065112 (2011).

[23] D. Zajfman, O. Heber, L. Vejby-Christensen, I. Ben-Itzhak, M. Rappaport, R. Fishman, and M. Dahan, Phys. Rev. A **55**, R1577 (1997).

[24] M. Dahan, R. Fishman, O. Heber, M. Rappaport, N. Altstein, D. Zajfman, and W. J. van der Zande, Rev Sci Instrum **69**, 76 (1998).

[25] W. H. Benner, Anal. Chem. **69**, 4162 (1997).

[26] J. D. Alexander, C. R. Calvert, R. B. King, O. Kelly, W. A. Bryan, G. R. a. J. Nemeth, W. R. Newell, C. A. Froud, I. C. E. Turcu, E. Springate, P. A. Orr, J. Pedregosa-Gutierrez, C. W. Walter, R. A. Williams, I. D. Williams, and J. B. Greenwood, J. Phys. B At. Mol. Opt. Phys. **42**, 154027 (2009).

[27] M. Lange, M. Froese, S. Menk, J. Varju, R. Bastert, K. Blaum, J. R. C. López-Urrutia, F. Fellenberger, M. Grieser, R. von Hahn, O. Heber, K.-U. Kühnel, F. Laux, D. A. Orlov, M. L. Rappaport, R. Repnow, C. D. Schröter, D. Schwalm, A. Shornikov, T. Sieber, Y. Toker, J. Ullrich, A. Wolf, and D. Zajfman, Rev. Sci. Instrum. **81**, 055105 (2010).

[28] H. T. Schmidt, H. Cederquist, J. Jensen, and A. Fardi, Nucl Instrum Methods Phys Res Sect B **173**, 523 (2001).

[29] T. Tanabe, K. Chida, K. Noda, and I. Watanabe, Nucl Instrum Methods Phys Res Sect A **482**, 595 (2002).

[30] T. Tanabe, K. Noda, and E. Syresin, Nucl. Instrum. Methods Phys. Res. Sect. Accel. Spectrometers Detect. Assoc. Equip. Int. Workshop Beam Cool. Relat. Top. **532**, 105 (2004).

[31] S. Jinno, T. Takao, Y. Omata, A. Satou, H. Tanuma, T. Azuma, H. Shiromaru, K. Okuno, N. Kobayashi, and I. Watanabe, Nucl Instrum Methods Phys Res Sect A **532**, 477 (2004).

[32] S. Jinno, Storage of Atomic/molecular Ions in an Eletrostatic Ring, Tokyo Metropolitan University, 2007.

[33] H. B. Pedersen, *The New Electrostatic Storage Ring SAPHIRA* (Presentation at 5th International Workshop on Electrostatic Storage Devices, Heidelberg, Germany, 2013).

[34] Y. Nakano, W. Morimoto, T. Majima, J. Matsumoto, H. Tanuma, H. Shiromaru, and T. Azuma, J. Phys. Conf. Ser. **388**, 142027 (2012).

[35] M. O. A. El Ghazaly, S. M. Alshammari, C. P. Welsch, and H. H. Alharbi, Nucl. Instrum. Methods Phys. Res. Sect. Accel. Spectrometers Detect. Assoc. Equip. **709**, 76 (2013).

[36] K. E. Stiebing, V. Alexandrov, R. Dörner, S. Enz, N. Y. Kazarinov, T. Kruppi, A. Schempp, H. Schmidt Böcking, M. Völp, P. Ziel, M. Dworak, and W. Dilfer, Nucl. Instrum. Methods Phys. Res. Sect. Accel. Spectrometers Detect. Assoc. Equip. **614**, 10 (2010).

[37] R. von Hahn, F. Berg, K. Blaum, J. R. Crespo Lopez-Urrutia, F. Fellenberger, M. Froese, M. Grieser, C. Krantz, K.-U. Kühnel, M. Lange, S. Menk, F. Laux, D. A. Orlov, R. Repnow, C. D. Schröter, A. Shornikov, T. Sieber, J. Ullrich, A. Wolf, M. Rappaport, and D. Zajfman, Nucl. Instrum. Methods Phys. Res. Sect. B Beam Interact. Mater. At. **269**, 2871 (2011).

[38] J. Matsumoto, *Construction of a Tabletop Electrostatic Storage Ring* (Presentation at 5th International Workshop on Electrostatic Storage Devices, Heidelberg, Germany, 2013).

[39] H. B. Pedersen, D. Strasser, O. Heber, M. L. Rappaport, and D. Zajfman, Phys. Rev. A **65**, 042703 (2002).

[40] O. Heber, P. D. Witte, A. Diner, K. G. Bhushan, D. Strasser, Y. Toker, M. L. Rappaport, I. Ben-Itzhak, N. Altstein, D. Schwalm, A. Wolf, and D. Zajfman, Rev Sci Instrum **76**, 013104 (2005).

[41] D. Grinfeld, A. Giannakopulos, I. Kopaev, A. Makarov, M. Monastyrskiy, and M. Skoblin, Eur. J. Mass Spectrom. **20**, 131 (2014).

[42] A. Fardi, ConeTrap: An Electrostatic Ion Trap for Atomic and Molecular Physics, Stocholm University, 2001.

[43] J. Bernard, S. Martin, L. Chen, H. Cederquist, A. Salmoun, and R. Brédy, Nucl Instrum Methods Phys Res Sect B **205**, 196 (2003).

[44] J. Bernard, B. Wei, A. Bourgey, R. Brédy, L. Chen, M. Kerleroux, S. Martin, G. Montagne, A. Salmoun, and B. Terpend-Ordacière, Nucl Instrum Methods Phys Res Sect B **262**, 105 (2007).

[45] M. W. Froese, M. Lange, S. Menk, M. Grieser, O. Heber, F. Laux, R. Repnow, T. Sieber, Y. Toker, R. von Hahn, A. Wolf, and K. Blaum, New J. Phys. **14**, 073010 (2012).

[46] T. Andersen, L. H. Andersen, P. Balling, H. K. Haugen, P. Hvelplund, W. W. Smith, and K. Taulbjerg, Phys. Rev. A **47**, 890 (1993).

[47] U. V. Pedersen, M. Hyde, S. P. Møller, and T. Andersen, Phys. Rev. A **64**, 012503 (2001).

[48] L. Knoll, K. G. Bhushan, N. Altstein, D. Zajfman, O. Heber, and M. L. Rappaport, Phys. Rev. A **60**, 1710 (1999).

[49] P. Reinhed, A. Orbán, J. Werner, S. Rosén, R. D. Thomas, I. Kashperka, H. A. B. Johansson, D. Misra, L. Brännholm, M. Björkhage, H. Cederquist, and H. T. Schmidt, Phys. Rev. Lett. **103**, 213002 (2009).

[50] K. G. Bhushan, H. B. Pedersen, N. Altstein, O. Heber, M. L. Rappaport, and D. Zajfman, Phys. Rev. A **62**, 012504 (2000).

[51] M. J. Jensen, U. V. Pedersen, and L. H. Andersen, Phys. Rev. Lett. **84**, 1128 (2000).

[52] J. Rajput, L. Lammich, and L. H. Andersen, Phys Rev Lett **100**, 153001 (2008).

[53] A. Naaman, K. G. Bhushan, H. B. Pedersen, N. Altstein, O. Heber, M. L. Rappaport, R. Moalem, and D. Zajfman, J Chem Phys **113**, 4662 (2000).

[54] L. H. Andersen, A. Lapierre, S. B. Nielsen, I. B. Nielsen, S. U. Pedersen, U. V. Pedersen, and S. Tomita, Eur. Phys. J. D **20**, 597 (2002).

[55] S. B. Nielsen, A. Lapierre, J. U. Andersen, U. V. Pedersen, S. Tomita, and L. H. Andersen, Phys Rev Lett **87**, 228102 (2001).

[56] S. Boyé, H. Krogh, I. B. Nielsen, S. B. Nielsen, S. U. Pedersen, U. V. Pedersen, L. H. Andersen, A. F. Bell, X. He, and P. J. Tonge, Phys. Rev. Lett. **90**, 118103 (2003).

[57] S. Boyé, I. B. Nielsen, S. B. Nielsen, H. Krogh, A. Lapierre, H. B. Pedersen, S. U. Pedersen, U. V. Pedersen, and L. H. Andersen, J. Chem. Phys. **119**, 338 (2003).

[58] S. Boyé, S. B. Nielsen, H. Krogh, I. B. Nielsen, U. V. Pedersen, A. F. Bell, X. He, P. J. Tonge, and L. H. Andersen, Phys. Chem. Chem. Phys. **5**, 3021 (2003).

[59] L. H. Andersen, H. Bluhme, S. Boyé, T. J. D. Jørgensen, H. Krogh, I. B. Nielsen, S. B. Nielsen, and A. Svendsen, Phys. Chem. Chem. Phys. **6**, 2617 (2004).

[60] K. Hansen, J. U. Andersen, P. Hvelplund, S. P. Møller, U. V. Pedersen, and V. V. Petrunin, Phys Rev Lett **87**, 123401 (2001).

[61] S. B. Nielsen, J. U. Andersen, J. S. Forster, P. Hvelplund, B. Liu, U. V. Pedersen, and S. Tomita, Phys. Rev. Lett. **91**, 048302 (2003).

[62] J. U. Andersen, P. Hvelplund, S. B. Nielsen, U. V. Pedersen, and S. Tomita, Phys Rev A **65**, 053202 (2002).

[63] M. Goto, J. Matsumoto, H. Shiromaru, Y. Achiba, T. Majima, H. Tanuma, and T. Azuma, Phys. Rev. A **87**, 033406 (2013).

[64] J. U. Andersen, H. Cederquist, J. S. Forster, B. A. Huber, P. Hvelplund, J. Jensen, B. Liu, B. Manil, L. Maunoury, S. Brøndsted Nielsen, U. V. Pedersen, H. T. Schmidt, S. Tomita, and H. Zettergren, Eur Phys J D **25**, 139 (2003).

[65] J. U. Andersen and E. Bonderup, Eur Phys J D **11**, 413 (2000).

[66] J. U. Andersen, C. Gottrup, K. Hansen, P. Hvelplund, and M. O. Larsson, Eur Phys J D **17**, 189 (2001).

[67] A. E. K. Sundén, M. Goto, J. Matsumoto, H. Shiromaru, H. Tanuma, T. Azuma, J. U. Andersen, S. E. Canton, and K. Hansen, Phys Rev Lett **103**, 143001 (2009).

[68] Y. Toker, O. Aviv, M. Eritt, M. L. Rappaport, O. Heber, D. Schwalm, and D. Zajfman, Phys Rev A **76**, 053201 (2007).

[69] M. W. Froese, K. Blaum, F. Fellenberger, M. Grieser, M. Lange, F. Laux, S. Menk, D. A. Orlov, R. Repnow, T. Sieber, Y. Toker, R. von Hahn, and A. Wolf, Phys. Rev. A **83**, 023202 (2011).

[70] M. Goto, A. E. K. Sundén, H. Shiromaru, J. Matsumoto, H. Tanuma, T. Azuma, and K. Hansen, J. Chem. Phys. **139**, 054306 (2013).

[71] G. Ito, T. Furukawa, H. Tanuma, J. Matsumoto, H. Shiromaru, T. Majima, M. Goto, T. Azuma, and K. Hansen, Phys. Rev. Lett. **112**, 183001 (2014).

[72] K. Najafian, M. S. Pettersson, B. Dynefors, H. Shiromaru, J. Matsumoto, H. Tanuma, T. Furukawa, T. Azuma, and K. Hansen, J. Chem. Phys. **140**, 104311 (2014).

[73] C. Ortéga, R. Brédy, L. Chen, J. Bernard, M. Ji, G. Montagne, A. R. Allouche, A. Cassimi, C. Joblin, and S. Martin, J. Phys. Conf. Ser. **583**, 012038 (2015).

[74] S. Martin, J. Bernard, R. Brédy, B. Concina, C. Joblin, M. Ji, C. Ortega, and L. Chen, Phys. Rev. Lett. **110**, 063003 (2013).

[75] A. Diner, Y. Toker, D. Strasser, O. Heber, I. Ben-Itzhak, P. D. Witte, A. Wolf, D. Schwalm, M. L. Rappaport, K. G. Bhushan, and D. Zajfman, Phys. Rev. Lett. **93**, 063402 (2004).

[76] T. Tanabe, S. Lee, K. Noda, I. Watanabe, and E. Syresin, in *Proc. EPAC 2002* (Paris, France, 2002), pp. 632–634.

[77] T. Tanabe, K. Noda, M. Saito, S. Lee, Y. Ito, and H. Takagi, Phys. Rev. Lett. **90**, 193201 (2003).

[78] M. O. A. El Ghazaly, A. Svendsen, H. Bluhme, A. B. Nielsen, S. B. Nielsen, and L. H. Andersen, Phys. Rev. Lett. **93**, 203201 (2004).

[79] A. Svendsen, H. Bluhme, M. Ghazaly, K. Seiersen, S. Nielsen, and L. Andersen, Phys. Rev. Lett. **94**, 223401 (2005).

[80] T. Tanabe, J. Phys. Conf. Ser. **58**, 17 (2007).

[81] H. B. Pedersen, D. Strasser, S. Ring, O. Heber, M. L. Rappaport, Y. Rudich, I. Sagi, and D. Zajfman, Phys Rev Lett **87**, 055001 (2001).

[82] H. B. Pedersen, D. Strasser, B. Amarant, O. Heber, M. L. Rappaport, and D. Zajfman, Phys. Rev. A **65**, 042704 (2002).

[83] D. Zajfman, Y. Rudich, I. Sagi, D. Strasser, D. W. Savin, S. Goldberg, M. Rappaport, and O. Heber, Int. J. Mass Spectrom. **229**, 55 (2003).

[84] D. Strasser, T. Geyer, H. B. Pedersen, O. Heber, S. Goldberg, B. Amarant, A. Diner, Y. Rudich, I. Sagi, M. Rappaport, D. J. Tannor, and D. Zajfman, Phys Rev Lett **89**, 283204 (2002).

[85] A. Vallette, C. I. Szabo, and P. Indelicato, EPL Europhys. Lett. **103**, 10009 (2013).

[86] R. N. Wolf, M. Eritt, G. Marx, and L. Schweikhard, Hyperfine Interact. **199**, 115 (2011).

[87] R. N. Wolf, G. Marx, M. Rosenbusch, and L. Schweikhard, Int. J. Mass Spectrom. **313**, 8 (2012).

[88] P. Boissel, P. de Parseval, P. Marty, and G. Lefèvre, J Chem Phys **106**, 4973 (1997).

[89] A. Léger, P. Boissel, and L. d' Hendecourt, Phys. Rev. Lett. **60**, 921 (1988).

[90] A. Léger, L. D'Hendecourt, and N. Boccara, in *Polycycl. Aromat. Hydrocarb. Astrophys.* (Reidel, Dordrecht, 1987), p. 243.

[91] M. Bixon and J. Jortner, J. Chem. Phys. **48**, 715 (1968).

[92] S. Leach, in *Polycycl. Aromat. Hydrocarb. Astrophys.*, edited by A. Léger, L. d' Hendecourt, and N. Boccara (Springer Netherlands, 1987), pp. 99–127.

[93] Y. Yamada, T. Ebata, M. Kayano, and N. Mikami, J. Chem. Phys. **120**, 7400 (2004).

[94] N. Nakashima and K. Yoshihara, J. Phys. Chem. **93**, 7763 (1989).

[95] Y. Liu, B. Tang, H. Shen, S. Zhang, and B. Zhang, Opt. Express **18**, 5791 (2010).

[96] A. Leger, L. D'Hendecourt, P. Boissel, and F. X. Desert, Astron. Astrophys. **213**, 351 (1989).

[97] G. Z. Whitten and B. S. Rabinovitch, J. Chem. Phys. **38**, 2466 (1963).

[98] K. Hansen, J. Chem. Phys. **128**, 194103 (2008).

[99] B. H. Bransden and C. J. Joachain, *Physics of Atoms and Molecules* (Pearson Education, 2003).

[100] J. Aihara, K. Fujiwara, A. Harada, H. Ichikawa, K. Fukushima, F. Hirota, and T. Ishida, J. Mol. Struct. THEOCHEM **366**, 219 (1996).

[101] Y. Ling, J. M. L. Martin, and C. Lifshitz, J. Phys. Chem. A **101**, 219 (1997).

[102] A. I. S. Holm, H. A. B. Johansson, H. Cederquist, and H. Zettergren, J Chem Phys **134**, 044301 (2011).

[103] H. a. B. Johansson, H. Zettergren, A. I. S. Holm, N. Haag, S. B. Nielsen, J. A. Wyer, M.-B. S. Kirketerp, K. Støchkel, P. Hvelplund, H. T. Schmidt, and H. Cederquist, J. Chem. Phys. **135**, 084304 (2011).

[104] Y. Ling and C. Lifshitz, J Phys Chem A **102**, 708 (1998).

[105] B. West, A. Sit, S. Mohamed, C. Joblin, V. Blanchet, A. Bodi, and P. M. Mayer, J. Phys. Chem. A **118**, 9870 (2014).

[106] H. Kühlewind, A. Kiermeier, and H. J. Neusser, J. Chem. Phys. **85**, 4427 (1986).

[107] H. W. Jochims, H. Rasekh, E. Rühl, H. Baumgärtel, and S. Leach, Chem. Phys. **168**, 159 (1992).

[108] J. U. Andersen, E. Bonderup, and K. Hansen, J Chem Phys **114**, 6518 (2001).

[109] D. J. Cook, S. Schlemmer, N. Balucani, D. R. Wagner, J. A. Harrison, B. Steiner, and R. J. Saykally, J. Phys. Chem. A **102**, 1465 (1998).

[110] A. Leger, L. D'Hendecourt, and D. Defourneau, Astron. Astrophys. **216**, 148 (1989).

[111] NIST Chem. WebBook (http://webbook.nist.gov).

[112] J. Postma, R. Hoekstra, A. G. G. M. Tielens, and T. Schlathölter, Astrophys. J. **783**, 61 (2014).

[113] *Private Communication with Christine Joblin.* (2015).

[114] J. Szczepanski, M. Vala, D. Talbi, O. Parisel, and Y. Ellinger, J Chem Phys **98**, 4494 (1993).

[115] G. Herzberg and J. W. T. Spinks, *Molecular Spectra and Molecular Structure: Diatomic Molecules* (Van Nostrand, 1950).

[116] J. Huh, *Unified Description of Vibronic Transitions with Coherent States* (2010).

[117] J. Ferguson, L. W. Reeves, and W. G. Schneider, Can. J. Chem. **35**, 1117 (1957).

[118] G. Malloci, G. Mulas, and C. Joblin, Astron. Astrophys. **426**, 105 (2004).

[119] G. Malloci, C. Joblin, and G. Mulas, Chem. Phys. **332**, 353 (2007).

[120] Q. Meng and H.-D. Meyer, J. Chem. Phys. **138**, 014313 (2013).

[121] J. B. Fenn, M. Mann, C. K. Meng, S. F. Wong, and C. M. Whitehouse, Science **246**, 64 (1989).

[122] M. E. Belov, A. W. Colburn, and P. J. Derrick, Rev. Sci. Instrum. **69**, 1275 (1998).

[123] J. U. Andersen, P. Hvelplund, S. B. Nielsen, S. Tomita, H. Wahlgreen, S. P. Moller, U. V. Pedersen, J. S. Forster, and T. J. D. Jorgensen, Rev Sci Instrum **73**, 1284 (2002).

[124] K. O. Nielsen, Nucl. Instrum. **1**, 289 (1957).

[125] T. Ooie, T. Yano, M. Yoneda, and M. Katsumura, J. Laser Appl. **12**, 171 (2000).

[126] E. N. Beebe and V. O. Kostroun, Rev. Sci. Instrum. **63**, 3399 (1992).

[127] M. P. Stockli, Rev. Sci. Instrum. **67**, 892 (1996).

[128] J. P. Flemming, J. Vac. Sci. Technol. **12**, 1369 (1975).

[129] B. K. Das and A. Shyam, Rev. Sci. Instrum. **79**, 123305 (2008).

[130] R. Geller, IEEE Trans. Nucl. Sci. **23**, 904 (1976).

[131] P. Sortais, Nucl. Instrum. Methods Phys. Res. Sect. B Beam Interact. Mater. At. **98**, 508 (1995).

[132] M. M. Abdelrahman, Sci. Technol. **2**, 98 (2012).

[133] C. Taylor, S. Caspi, M. Leitner, S. Lundgren, C. Lyneis, D. Wutte, S. T. Wang, and J. Y. Chen, IEEE Trans. Appl. Supercond. **10**, 224 (2000).

[134] C. M. Lyneis, D. Leitner, D. S. Todd, G. Sabbi, S. Prestemon, S. Caspi, and P. Ferracin, Rev. Sci. Instrum. **79**, 02A321 (2008).

[135] S. Hosokawa, N. Takahashi, M. Saito, and Y. Haruyama, Rev. Sci. Instrum. **81**, 063301 (2010).

[136] M. Barat, J. C. Brenot, J. A. Fayeton, and Y. J. Picard, Rev. Sci. Instrum. **71**, 2050 (2000).

[137] T. M. Stephen and B. L. Peko, Rev. Sci. Instrum. **71**, 1355 (2000).

[138] M. Ji, G. Montagne, R. Brédy, J. Bernard, L. Chen, and S. Martin, Phys. Scr. **T156**, 014092 (2013).

[139] K. Mehlig, K. Hansen, M. Hedén, A. Lassesson, A. V. Bulgakov, and E. E. B. Campbell, J. Chem. Phys. **120**, 4281 (2004).

[140] M. Ji, R. Brédy, L. Chen, J. Bernard, B. Concina, G. Montagne, A. Cassimi, and S. Martin, Phys. Scr. **T156**, 014091 (2013).

[141] O. Sukhorukov, A. Staicu, E. Diegel, G. Rouillé, T. Henning, and F. Huisken, Chem. Phys. Lett. **386**, 259 (2004).

[142] R. S. Sánchez-Carrera, V. Coropceanu, D. A. da Silva Filho, R. Friedlein, W. Osikowicz, R. Murdey, C. Suess, W. R. Salaneck, and J.-L. Brédas, J. Phys. Chem. B **110**, 18904 (2006).